Summer 2019

Role of Epigenome and Microbiome in Endocannabinoid-Mediated Regulation of Inflammation During Diet-Induced Obesity

Kathryn Miranda

Role of Epigenome and Microbiome in Endocannabinoid-Mediated Regulation of Inflammation During Diet-Induced Obesity

by

Kathryn Miranda

Bachelor of Science
College of Charleston, 2014

Submitted in Partial Fulfillment of the Requirements

For the Degree of Doctor of Philosophy in

Biomedical Science

School of Medicine

University of South Carolina

2019

Accepted by:

Mitzi Nagarkatti, Major Professor

Prakash Nagarkatti, Chairman, Examining Committee

Philip Brandon Busbee, Committee Member

Mohamad Azhar, Committee Member

Ho-Jin Koh, Committee Member

Cheryl L. Addy, Vice Provost and Dean of the Graduate School

DEDICATION

It is with love and gratitude that I dedicate this dissertation to my parents.

Mom and Dad: your immeasurable love, unconditional support, and

innumerable sacrifices have allowed me to succeed.

I could never say this enough—thank you.

ACKNOWLEDGEMENTS

My Ph.D. journey has been filled with many wonderful people deserving of appreciation, that without whom; completion of this dissertation would not have been possible.

I would first like to thank my mentors, Dr. Mitzi Nagarkatti and Dr. Prakash Nagarkatti, for their tremendous leadership, support, and encouragement all along the way. They took me in as a mentee with minimal research experience and provided every opportunity imaginable to learn and achieve. For that, and the rapport we have built, I am extremely grateful.

Secondly, I would like to thank the rest of my dissertation committee: Dr. P. Brandon Busbee, Dr. Mohamad Azhar, and Dr. Ho-Jin Koh, for their time and efforts to aid in completion of this dissertation.

Thank you to all the School of Medicine administrative faculty and staff, especially Dr. Edie Goldsmith, Ansley Roberts, Joann Nagy, Katie Harris, Debra Poston, Nicole Holt, Tina Akers, Lee Ann Faulling, Margaret Whisenant, and Syeedur Khandkar. Also, thank you to the Instrumentation Resource Facility staff and director Dr. Robert Price for help with microscopy applications. Thank you to veterinarian Dr. Shayne Barlow and his staff at the Department of Laboratory Animal Resources for their support with mouse work.

To the numerous past and present labmates and faculty of the Nagarkatti Lab: thank you all for your help, support, and friendship. I do not have room to

name everyone, but I would like to name those that have had significant impact on my research by either training me or performing contributing experiments: Dr. K. Alexa Gandy, Dr. P. Brandon Busbee, Dr. William Becker, Dr. Pegah Mehrpouya-Bahrami, Dr. Xiaoming Yang, Dr. Marpe Bam, Dr. Mona Hassuneh, Nicholas Dopkins, and Yin Zhong. I also appreciate collaborators at the University of South Carolina: Dr. Angela Murphy and Dr. Michael Walla, and at the Baylor College of Medicine: Dr. Nagireddy Putluri and his laboratory.

Finally, thank you so much to all of my family and friends that have provided continuous support and encouragement, especially: Patricia Miranda (“Mama”), Denise Miranda (“Mom”), Richard Miranda (“Dad”), my sisters Ginelle and Andrea Miranda, and Coach Jimmy Koosa. Thanks for always listening, displaying pride, and reminding me to enjoy the journey.

This research was supported in parts by NIH grants: R01ES019313, R01MH094755, R01AI123947, R01AI129788, P01AT003961, P20GM103641, R01AT006888, and a SPARC Graduate Research Grant from the Office of the Vice President for Research at the University of South Carolina. Metabolomics experiments performed in the Putluri Lab at Baylor were supported by American Cancer Society Award 127430-RSG-15-105-01-CNE, NIH/NCI R01CA220297, and NIH/NCI R01CA216426, CPRIT Proteomics and Metabolomics Core Facility, (RP170005), NIH (P30 CA125123), and Dan L. Duncan Cancer Center.

ABSTRACT

Obesity is an inflammatory disease involving accumulation of adipose tissue, gut microbiota dysbiosis, and over-activation of the endocannabinoid system (ECS). Mechanisms involved in ECS regulation of obesity-induced inflammation are not well understood. Presented here are three chapters involving microRNA (miR) regulation of inflammatory adipose tissue macrophages (ATM) during high-fat diet (HFD)-induced obesity and cannabinoid receptor-mediated regulation of gut microbiota dysbiosis.

ATMs are innate immune cells that drive chronic low-grade inflammation during obesity. Polarization between pro-(M1) and anti-(M2-like) inflammatory phenotypes influence insulin sensitivity and energy expenditure; however, the mechanisms involved are unclear. In study one, we characterized miRs involved in ATM polarization during diet-induced obesity (DIO). In study two, DIO mice were treated with the cannabinoid receptor 1 (CB1) antagonist AM251 because CB1 antagonists ameliorate DIO and associated inflammation. In both studies, it was found that the miR-30 family regulates ATM Delta-like-4 (DLL4)-Notch signaling, and consequently ATM polarization. Downregulation of miRs 30a-5p, 30c-5p, and 30e-5p in ATMs from DIO mice versus lean mice resulted in Notch-signaling induced M1 polarization. Interestingly, miR-30e-5p was upregulated in ATMs from DIO mice treated with AM251, while DLL4 was downregulated.

Subsequently, fat storage and M1 ATM polarization was reduced. Furthermore, AM251-treated macrophages suppressed DLL4-mediated Th1 polarization in CD4+ T cells. The combined effect of miR-30 in ATMs and consequently T cells led to an anti-inflammatory state and attenuation of diet-induced obesity regulated by CB1 blockade.

In the third study, $CB1^{-/-}$ and $CB2^{-/-}$ mice as well as AM251 DIO intervention were used to investigate ECS regulation of DIO-associated gut dysbiosis. $CB1^{-/-}$ mice displayed resistance, whereas, $CB2^{-/-}$ mice displayed accelerated DIO development versus wild-type (WT) mice. Interestingly, CB1 and CB2 reciprocally regulated HFD-induced leukocyte infiltration in the cecal-colonic lamina propria. Microbiota profiling showed that $CB1^{-/-}$, but not WT or $CB2^{-/-}$ mice were resistant to development of HFD-induced gut dysbiosis. Moreover, AM251 intervention in obese mice shifted their microbiota towards a lean profile. Investigation of host: microbiota interactions revealed ECS-mediated regulation of intestinal barrier defense and gut microbiota-mediated sugar metabolism were involved in the pathogenesis of obesity.

Together, our studies demonstrate that DIO is regulated by endocannabinoids through alterations in miRNA and microbiota that regulate inflammation. Thus, approaches aimed at modulating such pathways may provide novel therapeutic modalities to treat obesity.

TABLE OF CONTENTS

DEDICATION iii

ACKNOWLEDGEMENTS iv

ABSTRACT vi

LIST OF TABLES ix

LIST OF FIGURES x

LIST OF ABBREVIATIONS xiii

CHAPTER 1: INTRODUCTION 1

CHAPTER 2: MICRORNA-30 MODULATES METABOLIC INFLAMMATION BY REGULATING NOTCH SIGNALING IN ADIPOSE TISSUE MACROPHAGES 13

CHAPTER 3: CANNABINOID RECEPTOR 1 BLOCKADE ATTENUATES OBESITY AND ADIPOSE TISSUE TYPE 1 INFLAMMATION THROUGH MIR-30E-5P REGULATION OF DELTA-LIKE-4 IN MACROPHAGES AND CONSEQUENTLY DOWNREGULATION OF TH1 CELLS 47

CHAPTER 4: CANNABINOID RECEPTOR SIGNALING MEDIATES SUSCEPTIBILITY TO HIGH FAT DIET-INDUCED INTESTINAL DYSBIOSIS AND REGULATES METABOLIC HEALTH 78

CHAPTER 5: CONCLUSION 134

REFERENCES 137

APPENDIX A: DETAILED EXPERIMENTAL PROTOCOLS 162

APPENDIX B: PERMISSION TO REPRINT 168

LIST OF TABLES

Table 2.1 Dysregulated miRNAs and macrophage polarization genes 37

Table 3.1 Dysregulated miRNAs and their experimental fold change observations in F4/80+ ATMs. 69

LIST OF FIGURES

Figure 1.1 Epididymal adipose tissue morphology in lean and high-fat diet-induced obese mice.. 12

Figure 2.1 HFD-Induced Obesity Stimulates ATM Inflammation and miRNA Dysregulation. 38

Figure 2.2 HFD-Induced Obesity Elicits Distinct Transcript and miRNA Expression Profiles in ATMs. 40

Figure 2.3 MicroRNA-30 targets the Dll4 3'UTR. 41

Figure 2.4 DLL4 Expression is Elevated in Obese ATMs. 42

Figure 2.5 miR-30 Inhibition Induces DLL4-Notch1 Signaling and M1 polarization. 43

Figure 2.6 MicroRNA-30 Inhibitor LNAs downregulate miR-30 Expression. 44

Figure 2.7 Inhibition of DLL4-Notch signaling lessens inflammation in miR-30 inhibitor-transfected macrophages. 44

Figure 2.8 Lentiviral overexpression of miR-30a-5p in RAW264.7 macrophages reduces inflammation. 45

Figure 2.9 DNA Methylation-Dependent Regulation of miR-30. 45

Figure 2.10 Illustrative summary. 46

Figure 3.1 Treatment of mice with the CB1 antagonist (AM251) reverses obesity. 70

Figure 3.2 CB1 blockade reduces abundance of pro-inflammatory macrophages in epididymal fat. 71

Figure 3.3 AM251 treatment elevates ATM miR-30e-5p and reduces target expression of the pro-inflammatory Notch ligand Delta-like-4. 72

Figure 3.4 Pathway analysis of dysregulated miRNAs following AM251 treatment. 73

Figure 3.5 AM251 treatment in vivo reduces energy storage and type 1 inflammation associated with DLL4-Notch signaling 74

Figure 3.6 Confirmation of M1 polarization in BMDM and Th1 polarization in CD4+ T cells 75

Figure 3.7 AM251 reduces expansion of pro-inflammatory Th1 cells by downregulating DLL4 in macrophages. 76

Figure 3.8 Blocking CB1 receptors reverses obesity through miR-30e-5p regulation of DLL4. 77

Figure 4.1 CB1 deletion promotes resistance to DIO 118

Figure 4.2 CB1 knockout delays DIO development and glucose intolerance 119

Figure 4.3 Loss of CB1 suppresses HFD-induced inflammation 120

Figure 4.4 Loss of CB1 suppresses HFD-induced intestinal inflammation and permeability 121

Figure 4.5 $CB1^{-/-}$ mice are resistant to HFD-induced alterations in gut microbiota 122

Figure 4.6 Predictive metagenomics by 16S V3-V4 rRNA gene sequencing 123

Figure 4.7 Gut microbiota composition is largely dispensable for the improved obesity phenotype observed in $CB1^{-/-}$ mice 124

Figure 4.8 Co-housing WT and $CB1^{-/-}$ mice does not confer resistance to DIO development; however, $CB1^{-/-}$ maintain a dominant microbiota composition 125

Figure 4.9 Transfer of $CB1^{-/-}$ feces does not confer resistance to DIO development 126

Figure 4.10 DIO intervention with the CB1 antagonist AM251 reverses obesity, inflammation, and shifts intestinal microbiota composition 127

Figure 4.11 AM251 DIO intervetion predictive metagenomics by 16S V3-V4 rRNA gene sequencing 128

Figure 4.12 CB1 regulates microbial defense in intestinal epithelial cells 129

Figure 4.13 CB1 regulates host and intestinal microbiota sugar metabolism 130

Figure 4.14 Microbiota sugar metabolic pathways correlate with body weight gain 132

Figure 4.15 CB1 blockade improves DIO-induced intestinal dysbiosis 133

List of Abbreviations

2-AG.....2-arachidonylglycerol

Ab..... antibody

Abx.....antibiotics

AEA.....N -arachidonoyl-ethanolamine, anandamide

APC.....antigen-presenting cell or allophycocyanin

ATM .....adipose tissue macrophage

AU .....arbitrary unit

A.U.C. ..... area under the curve

BMC ..... bone marrow cell

BMDM .....bone marrow-derived macrophage

bp .....basepair

BSA..... bovine serum albumin

C57BL6 .....“C57 black 6” mouse strain

CB1 ..... cannabinoid receptor type 1

CB2 ..... cannabinoid receptor type 2

ccIEC ..... cecal:colonic intestinal epithelial cell

CCL2 ..... C-C motif chemokine ligand 2 (also MCP-1)

ccLP ..... cecal:colonic lamina propria

CD..... cluster of differentiation

cDNA..... complementary DNA

CM-3T3-L1A .....conditioned medium from 3T3-L1 adipocytes

CNS ..... central nervous system

DEXA ..... dual energy x-ray absorptiometry

DIO ..... diet-induced obesity

DLL4 ..... Delta-like ligand 4

DMEM ..... Dulbecco's modified Eagle's medium

DMEM/F12 ..... DMEM/Ham's F12 nutrient mixture

DNMT ..... DNA methyltransferase

DPBS ..... Dulbecco's phosphate buffered saline

eCB ..... endocannabinoid

ECS ..... endocannabinoid system

EDTA ..... ethylenediaminetetraacetic acid

ELISA ..... enzyme-linked immunosorbent assay

EpCAM ..... epithelial cell adhesion molecule (also CD326)

FAAH ..... fatty acid amide hydrolase

FACS ..... fluorescence-activated cell sorter

FASTQ ..... text-based format for sequencing reads including quality scores

FBS ..... fetal bovine serum

FC ..... fold change

FcR ..... Fc (fragment, crystallizable) receptor

FIJI ..... FIJI is Just ImageJ

FITC ..... fluorescein isothiocyanate

FMT ..... fecal microbiota transplantation

Fru ..... fructose

GI ..... gastrointestinal

GTT ..... glucose tolerance test

H&E.....hematoxylin and eosin

HBSS.....Hank's balanced salt solution

HEPES.....4-(2-hydroxyethyl)-1-piperazineethanesulfonic acid (buffer)

HFD.....high-fat diet

HOMA-IR.....homeostatic model assessment of insulin resistance index

HPLC.....high performance liquid chromatography

IEC.....intestinal epithelial cell

IEL.....intraepithelial leukocyte

IFNγ.....interferon gamma

IL-.....interleukin-

IPA.....Ingenuity Pathway Analysis

kD.....kilodalton

LDA.....linear discriminant analysis

LEfSe.....LDA effect size

LFD.....low-fat diet

LNA.....locked nucleic acid

LPMC.....lamina propria mononuclear cell

LPS.....lipopolysaccharide

Lyz2.....lysozyme 2

M-CSF.....macrophage colony-stimulating factor

mAb.....monoclonal antibody

Man.....mannose

MCP-1.....monocyte chemoattractant protein 1 (also CCL2)

meDIP-seq.....methylated DNA immunoprecipitation sequencing

miR or miRNA.....microRNA

MNE ..... mean normalized expression

NCD ..... normal chow diet

NIH ..... National Institutes of Health

OTU ..... operational taxonomic unit

PBS ..... phosphate buffered saline

PC ..... principal component

PCA or PCoA ..... principal component analysis

PCR ..... polymerase chain reaction

PE ..... phycoerythrin

Cy7 ..... cyanine 7

PEP ..... phosphoenolpyruvate

PICRUSt ..... Phylogenetic Investigation of Communities by Reconstruction of Unobserved States

PTS ..... phosphotransferase system

qRT-PCR ..... quantitative reverse transcription PCR

RBC ..... red blood cell

ROI ..... region of interest

RPM ..... rotations per minute

rRNA ..... ribosomal RNA

RT ..... room temperature

SCFA ..... short chain fatty acid

STAT ..... signal transducer and activator of transcription

SVF ..... stromal vascular fraction

TBS-T ..... tris buffered saline with Tween80

TCA ..... tricarboxylic acid cycle

TGF-β ..... transforming growth factor beta

TLR4 ..... toll-like receptor 4

TNFα ..... tumor necrosis factor alpha

Treg ..... regulatory T cell

Tx ..... treatment

UTR ..... untranslated region

V3-V4 ..... variable region 3 – variable region 4

Veh ..... vehicle

WHO ..... World Health Organization

WT ..... wild-type

CHAPTER 1

INTRODUCTION

1.1 OBESITY

The World Health Organization (WHO) defines obesity as “excessive fat accumulation that presents a risk to health”. Its incidence has reached epidemic proportions and continues to rise. WHO reports from 2016 indicated that over 1.9 billion adults were overweight or obese worldwide. That equates to approximately 39% of the global population. Furthermore, the WHO estimated over 340 million children and adolescents were considered overweight or obese in 2016. These data are an obvious indication that obesity is a major health concern that requires attention.

Obesity has been an issue for centuries; however, in 2008 The Obesity Society presented evidence to advocate characterization of obesity as a disease (Allison et al., 2008). After much debate, the American Medical Association officially declared obesity as a disease in 2013, which allowed increased research and access to healthcare (Kyle et al., 2016). Eventual declaration of obesity as a disease can be attributed to its correlation with development of comorbid disorders such as type II diabetes, cardiovascular diseases, and some types of cancers, which together, put a large burden on the healthcare system (Redinger, 2007). Obesity is a preventable yet chronic condition that can be

cured with the right lifestyle modifications or interventions. Causes of obesity include environmental factors such as poor diet composition, overeating, and sedentary lifestyle, as well as, genetic predisposition (Haslam and James, 2005). It is reported that many physiological processes and interactions contribute to obesity such as inflammation, the endocannabinoid system, and the intestinal flora (Cota et al., 2003; Lumeng et al., 2007; Muccioli et al., 2010; Sonnenburg and Bäckhed, 2016). Still, there is much to be learned about the complex etiology of this disease in order to develop more efficient therapeutic interventions.

1.2 Metabolic Inflammation

Inflammation is the underlying cause of many diseases including obesity. During obesity, inflammation occurs in various metabolic organs including the adipose tissue, liver, muscle, and intestinal tract, which promote a state of chronic sub-clinical systemic inflammation that encourages metabolic dysfunction (Lackey and Olefsky, 2016). Specific to this dissertation, adipose tissue inflammation and intestinal immunity are investigated.

In adipose tissue, increased adiposity, particularly visceral fat expansion, promotes metabolic inflammation. Importantly, inflammation originating from adipose tissue is thought to initiate the development of obesity-induced insulin resistance and type II diabetes (Xu et al., 2003). Adipocyte hypertrophy and hyperplasia results in stress-induced cell death and release of pro-inflammatory adipokines as well as damage-associated molecular patterns that recruit immune cells into the adipose tissue to clean up damage (Sun et al., 2012). Recruited

immune cells produce additional pro-inflammatory cytokines to promote chronic low-grade inflammation (Fontana et al., 2007). Macrophages are myeloid-derived phagocytic cells of the innate immune system that make up a majority of the immune infiltrate to dominate the adipose tissue by both phenotype and number (Boutens and Stienstra, 2016; Red Eagle and Chawla, 2010; Weisberg et al., 2003; Xu et al., 2003). They are capable of polarizing between a broad spectrum of pro- and anti- inflammatory phenotypes (routinely classified as M1 and M2, respectively) and several subsets have been described that are involved in not only inflammatory responses but also in buffering lipolysis by storing lipids and preventing their release into circulation (Boutens and Stienstra, 2016; Hamilton et al., 2014; Mantovani et al., 2002). Lean adipose tissue contains resident M2-like ATMs that are uniformly dispersed and secrete anti-inflammatory cytokines such as IL-4, TGFβ, and IL-10 to maintain insulin sensitivity and tissue homeostasis (Fujisaka et al., 2009). Obesity promotes infiltration, retention, proliferation, and polarization of pro-inflammatory M1 ATMs that dominate the tissue, form crown-like-structures around necrotic adipocytes, and produce pro-inflammatory cytokines such as TNFα, IL-1β, MCP-1, and IL-6 that decrease insulin sensitivity, increase adipocyte lipolysis, and recruit additional immune cells (Olefsky and Glass, 2010). Microscopy images of epididymal fat from lean and diet-induced obese mice illustrate these phenotypic differences of adipocyte and ATM morphology (Figure 1.1). Due to vast disparities observed in ATM functionality and number between lean and obese individuals, ATMs play a critical role in determining development of obesity-related pathologies. Therapeutic strategies

that lessen ATM inflammation would be beneficial to reduce obesity and comorbid disorders such as insulin resistance (Fujisaka et al., 2009; Sun et al., 2012).

Intestinal inflammation is another contributor to obesity-induced metabolic dysfunction. The intestinal immune system is comprised of mucus, intestinal epithelial cells (IECs), innate lymphoid cells, as well as other innate and adaptive immune cells that reside in the intraepithelial layer or lamina propria (Winer et al., 2016). During homeostasis, IECs secrete protective mucus and antimicrobial peptides that prevent microbial breach of the intestinal barrier (Winer et al., 2016). Innate immune cells and regulatory T cells also produce anti-inflammatory mediators such as IL-22 and IL-10 that promote tolerance and barrier integrity (Winer et al., 2016). During obesity, intestinal immunity is altered due to changes in composition and interaction with the gut microbiota. Pro-inflammatory T cells produce IFNγ and IL-17. Resultant intestinal permeability allows microbe associated molecular patterns, such as lipopolysaccharide (LPS), to enter circulation and activate innate immune responses through toll-like receptor 4 and it's co-receptor CD14 (Zhang et al., 2019). Thus, LPS in circulation stimulates metabolic endotoxemia and pro-inflammatory cytokine production that promotes adipose tissue insulin resistance and is thought to be a main initiator of obesity-induced metabolic dysfunction (Cani et al., 2007, 2008). Together, these data indicate that maintenance of intestinal barrier homeostasis is crucial for protecting against metabolic dysfunction.

1.3 Endocannabinoid System

The endocannabinoid system (ECS) regulates a multitude of obesity-related physiological processes. These include appetite, inflammation, intestinal permeability and motility, etc (Azua et al., 2017; Cani et al., 2016; Cota et al., 2003). The ECS is comprised of cannabinoid receptors and their endogenous lipophilic ligands called endocannabinoids. The two main cannabinoid receptors are the seven-transmembrane G-protein coupled receptors CB1 and CB2, although non-classical cannabinoid receptors include the orphan receptor GPR55 and transient receptor potential vanilloid type 1. CB1 expression is most abundant in the central nervous system but is also located at peripheral nerve terminals, in metabolic tissues such as the liver, adipose tissue, muscle, and intestines, and in some immune cells (Maccarrone et al., 2015). CB2 is mainly expressed in the immune system, where its activation promotes anti-inflammatory responses (Turcotte et al., 2016). The two best-characterized endocannabinoids are arachidonic acid derivatives N-arachidonoylethanolamine (Anandamide, AEA), a high affinity, partial agonist for CB1, and 2-arachidonylglycerol (2-AG), a moderate affinity, full agonist at both CB1 and CB2. Both of these endocannabinoids are produced as needed from cell membrane lipid precursors (Maccarrone et al., 2015). AEA is produced by the enzymes N-acyltransferase and N-acyl-phosphatidylethanolamine-specific phospholipase D and broken down by mainly by fatty acid amide hydrolase (FAAH) (Maccarrone et al., 2015). AEA is also a precursor for various inflammatory mediators such as prostaglandins and leukotrienes. 2-AG is synthesized by diacylglycerol lipases

alpha and beta, and quickly catabolized by monoacylglycerol lipase (Maccarrone et al., 2015).

Modulation of ECS activity during obesity was recognized in the early 2000s when it was discovered that activation of CB1 promotes over eating and obesity (Cota et al., 2003). Subsequent CB1 knockout and antagonist studies in animal models confirmed involvement of CB1 activation in promoting obesity, which led to testing CB1 antagonists for human obesity intervention (Ravinet Trillou et al., 2003, 2004). Unfortunately, adverse neuropsychiatric side effects caused SR141716A (also known as Rimonabant), a CB1 antagonist, to be removed from market (Pi-Sunyer et al., 2006; Sam et al., 2011). Despite this, animal studies have continued in order to identify mechanisms involved in the beneficial effects of CB1-blockade, some of which are presented in this dissertation.

Furthermore, circulating endocannabinoids are elevated during obesity, however; overactivation of CB1 by AEA is most recognized to contribute to excessive energy storage and appetite (Balsevich et al., 2018; Brown et al., 2012; Engeli et al., 2005; Touriño et al., 2010). Genetic ablation of FAAH, which hydrolyzes AEA, promotes excessive energy storage and adiposity (Touriño et al., 2010). Moreover, mutations in the FAAH gene are associated with human obesity (Sipe et al., 2005). These observations further support the beneficial effects of CB1 blockade on obesity.

More recently the role of CB2 activation in metabolic regulation has been discovered. Treatment of obese mice with the CB2 agonist JWH-015 reduces fat mass and inflammation, which indicates that not only blocking CB1 but also activating CB2 has anti-obesity effects (Verty et al., 2015). Polymorphisms in the CB2 gene (*Cnr2*) also contribute to overeating disorders (Ishiguro et al., 2010). This demonstrates the complementary nature of cannabinoid receptor signaling and also indicates that some beneficial effects observed upon CB1 blockade may be attributed to increased endocannabinoid signaling through CB2. In this dissertation, data in regards to CB2 signaling in obesity are also provided.

1.4 Epigenetic Regulation

Epigenetic regulation of gene expression is regulation independent of alterations in DNA sequence. It is important to note that many environmental factors such as diet, exercise, and stress, etc. can alter gene expression through epigenetic modifications without changing the underlying DNA sequence (Toraño et al., 2016). Therefore studying epigenetic regulation is essential to understand the pathophysiology of many diseases. Epigenetic mechanisms pertinent to this dissertation are microRNAs (miRNA, miR) and DNA methylation.

MicroRNAs are short (~22 nucleotide long) non-coding RNAs that silence genes by complementary binding to the 3' untranslated region of target genes, which causes translational repression or transcript degradation (Bartel, 2004). It is thought that ~60% of protein-coding genes are conserved targets of miRNAs and therefore they have emerged as important regulators of gene expression

(Lewis et al., 2005). Additionally, specific miRNAs have been identified as biomarkers and/or prognostic indicators in a variety of diseases, which demonstrates their importance in the field of personalized medicine and currently, synthetic miRNA mimics and inhibitors are being developed for clinical purposes (Alexander et al., 2011; Reid et al., 2016).

DNA methylation silences gene expression due to chromatin condensation (Caiafa and Zampieri, 2005). DNA methyltransferases (DNMT) add methyl groups to cytosine nucleotides. DNMT1 maintains DNA methylation while DNMT3a and DNMT3b perform de novo methylation (Jin and Robertson, 2013). Methylated cytosines primarily reside in CpG islands—which are genomic regions of enriched C-G content proximal to transcription start sites—and repress gene transcription by decreasing accessibility of transcription factor binding sites (Caiafa and Zampieri, 2005). Importantly, DNA methylation has been implicated in development of pathologies including atherosclerosis and cancer, and has been a therapeutic target for several diseases (Dong et al., 2002; Zhang et al., 2011).

1.5 MICROBIOTA

It is becoming increasingly evident that the intestinal flora is a major contributor to the pathophysiology of many diseases, including obesity. The gut microbiota is comprised of trillions of microbes that colonize the gastrointestinal tract and collectively contribute to metabolic processes, such as energy harvest, and can be thought of as a metabolic organ (Bäckhed et al., 2007). The

dependence on microbiota for excessive energy harvest was identified in 2004 when it was discovered that germ-free mice fed a high-fat diet were more lean than conventionally raised colonized mice (Bäckhed et al., 2004). Additionally, conventionalization of germ-free mice led to rapid increases in weight gain (Bäckhed et al., 2004). More recent studies have also demonstrated that microbiota depletion through antibiotic administration promotes white adipose tissue browning, which increases energy expenditure, reduces inflammation, and lessens obesity (Suárez-Zamorano et al., 2015). Hence the complex interactions of the gut microbiota with host processes have been investigated for therapeutic purposes.

The advent of next-generation sequencing technology has allowed characterization of the gut microbiome, including those microbes that are difficult to culture and thus poorly characterized (Forde and O'Toole, 2013). Interrogation of the obese gut microbiome revealed that it has an increased capacity for energy harvest, decreased diversity, and generally an increase in the Firmicutes to Bacteroidetes ratio (Ley et al., 2005; Turnbaugh et al., 2006). These alterations in the obese microbiome can be called "dysbiosis" due to having detrimental effects on host health status (Petersen and Round, 2014). Interestingly, fecal transplantation transfers donor obesity phenotype into the recipient (Turnbaugh et al., 2006). Transfer of donor phenotypes in various disease models has made the gut microbiota a very interesting therapeutic target (Gupta et al., 2016). In fact, fecal microbiota transplant to promote weight loss in

obese people is currently in clinical trial (ClinicalTrials.gov identifier: NCT03789461).

While the association of the gut microbiota composition with obesity phenotype is well established, there is still much to be learned about the complex interactions between various microbes and the host. This will aid in developing better therapeutics in the future. In particular, ECS modulation of the gut microbiota: host interactions during obesity are presented within this dissertation.

1.6 Hypotheses and Aims

Obesity is an energy imbalance disease that is characterized by overactivation of the ECS, chronic-low grade inflammation, and gut microbiota dysbiosis. CB1 blockade reverses obesity, yet the anti-inflammatory mechanisms involved are not well characterized. Furthermore, characterization of the gut microbiome: host interactions with cannabinoid receptor signaling modulation have not been heavily investigated. This dissertation presents three studies that were aimed at investigating ECS regulation of ATM-mediated inflammation and gut microbiota: host interactions.

In study one, miRNA regulation of ATM polarization was investigated in a mouse model of diet-induced obesity. Classification of miRNA profiles in lean and obese ATMs were not previously characterized. We hypothesized that the inflammatory polarization of ATMs could be regulated by miRNA expression.

In the second study, we investigated the anti-inflammatory mechanisms involved in attenuation of diet-induced obesity after CB1 blockade. We

hypothesized that decreased obesity and inflammation observed following CB1 antagonist treatment in diet-induced obese mice was associated with altered miRNA profile in ATMs.

In the final study, gut microbiota profiles and microbiota: host interactions were investigated in diet-induced obese mice of wild-type, $CB1^{-/-}$ and $CB2^{-/-}$ genotypes, as well as in obese mice treated with the CB1 antagonist AM251. We hypothesized that the ECS contributes to the overall metabolic and inflammatory tone during obesity through alterations in gut microbiota composition/metabolism and/or host microbial defense mechanisms, primarily through CB1-dependent mechanisms.

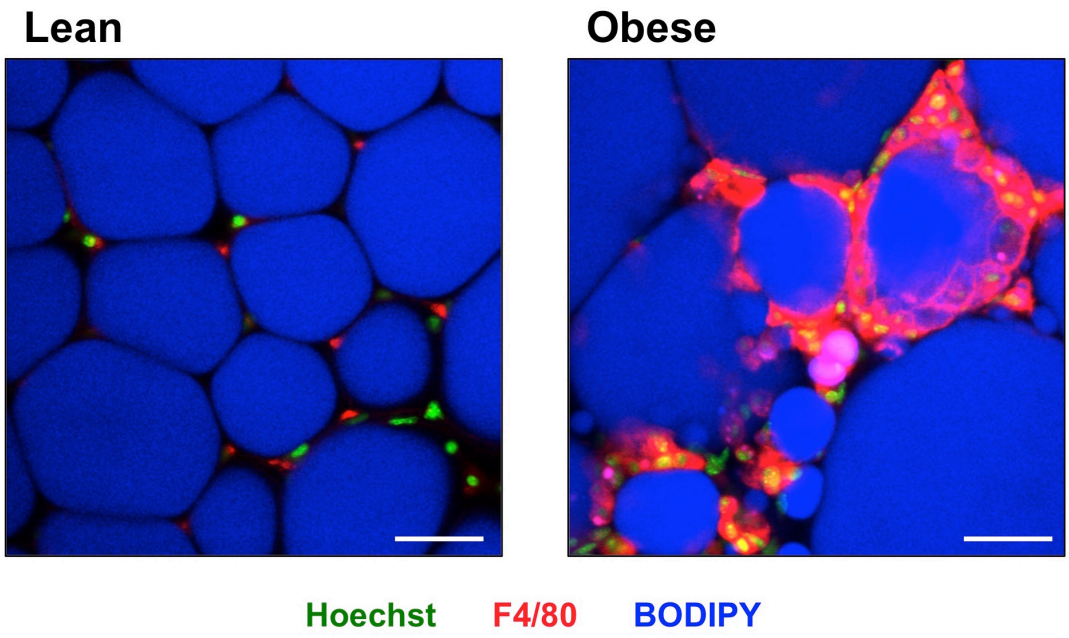

Figure 1.1 Epididymal adipose tissue morphology in lean and high-fat diet-induced obese mice.

Immunofluorescent staining of epididymal adipose tissue from lean and obese mice shows distinct morphological features. Lean adipose tissue is homeostatic with organized adipocyte structure and uniformly dispersed ATMs that maintain immune surveillance. Obese adipose tissue contains hypertrophic adipocytes and infiltrating ATMs that form crown-like structures around necrotic adipocytes. Tissue damage is evident. Whole mount staining of adipose tissue and confocal microscopy were performed as described in chapter 2, section 2. Green depicts Hoechst staining of cellular nuclei. Red indicates Immunofluorescent staining of F4/80+ macrophages. Blue represents BODIPY staining of lipids and adipocytes. Images were acquired with a 40X water immersion objective.

CHAPTER 2

MICRORNA-30 MODULATES METABOLIC INFLAMMATION BY REGULATING NOTCH SIGNALING IN ADIPOSE TISSUE MACROPHAGES[1]

[1] Miranda, K., X. Yang, M. Bam, E.A. Murphy, P.S. Nagarkatti, and M. Nagarkatti. (2018) "MicroRNA-30 Modulates Metabolic Inflammation by Regulating Notch Signaling in Adipose Tissue Macrophages." *International Journal of Obesity* 42 (6): 1140–50.
Reprinted here with permission of publisher.

2.1 ABSTRACT

Background/Objectives: Obesity is a pandemic disorder that is characterized by accumulation of adipose tissue and chronic-low grade inflammation that is driven primarily by adipose tissue macrophages (ATMs). While ATM polarization from pro-(M1) to anti-(M2) inflammatory phenotype influences insulin sensitivity and energy expenditure, the mechanisms of such a switch are unclear. In the current study we identified epigenetic pathways including microRNAs (miR) in ATMs that regulate obesity-induced inflammation.

Subjects/Methods: Male C57BL/6J mice were fed normal chow diet (NCD) or high-fat diet (HFD) for 16 weeks to develop lean and diet-induced obese mice respectively. Transcriptome microarrays, microRNA microarrays, and meDIP-Seq were performed on ATMs isolated from visceral fat. Pathway analysis and bone marrow derived macrophage (BMDM) transfections further allowed computational and functional analysis of miRNA-mediated ATM polarization.

Results: ATMs from HFD-fed mice were skewed towards M1 inflammatory phenotype. Concurrently, the expression of miRs 30a-5p, 30c-5p, and 30e-5p was downregulated in ATMs from HFD mice when compared to mice fed NCD. The miR-30 family was shown to target Delta-like-4, a Notch1 ligand, whose expression was increased in HFD ATMs. Inhibition of miR-30 in conditioned BMDM triggered Notch1 signaling, pro-inflammatory cytokine production, and M1 macrophage polarization. In addition, DNA hypermethylation was observed in *mir30*-associated CpG islands suggesting HFD downregulates miR-30 through epigenetic modifications.

Conclusions: HFD-induced obesity downregulates miR-30 by DNA methylation thereby inducing Notch1 signaling in ATMs and their polarization to M1 macrophages. These findings identify miR-30 as a regulator of pro-inflammatory ATM polarization and suggest miR-30 manipulation could be a therapeutic target for obesity-induced inflammation.

2.2 Introduction

Overnutrition causes obesity and adipose tissue macrophage (ATM)-dependent inflammation that enhances risk for type II diabetes, cardiovascular disease, and some cancers. Macrophages are innate immune cells that display remarkable plasticity between pro- and anti-inflammatory phenotypes. They are routinely classified as M1 and M2 respectively, although various subtypes exist (Hamilton et al., 2014). At steady state, resident M2-like ATMs contribute to insulin sensitivity and adipose tissue homeostasis through production of anti-inflammatory cytokines such as IL-10 (Boutens and Stienstra, 2016). During obesity, M1 ATMs dominate the adipose tissue in both phenotype and abundance, promoting insulin resistance and chronic low-grade inflammation (Lumeng et al., 2007). Due to vast disparities seen in ATM functionality between lean and obese individuals, ATMs have been suggested to play a substantial role in determining development of obesity-related pathologies. Therapeutic strategies that decrease ATM-dependent inflammation have been heavily investigated due to the tight correlation of macrophage-dependent inflammation and insulin resistance.

Notch signaling plays key roles in metabolic and inflammatory processes (Bi and Kuang, 2015). It is highly conserved juxtacrine signaling utilized by numerous cell types including macrophages and adipocytes. Binding of Notch receptors (Notch1-4) by Delta-like and Jagged ligands (DLL1, -3, -4 and JAG1, -2) initiates proteolytic release of the Notch intracellular domain (NICD) allowing it to translocate to the nucleus and activate Jk-Recombination Signal-Binding Protein (RBP-J)-dependent transcription (Borggrefe and Liefke, 2012). In macrophages, Notch1 signaling promotes pro-inflammatory polarization through IRF8 and NF-kB transcriptional pathways, while in adipocytes, Notch1 signaling inhibits white adipose tissue browning and energy expenditure, and promotes insulin resistance (Bi et al., 2014; Pajvani et al., 2011; Xu et al., 2012). Additionally, blockade of the canonical Notch1 ligand DLL4 improves atherosclerosis and metabolic disease indicating DLL4-Notch1 signaling is directly involved in the crosstalk of inflammatory and metabolic pathways (Fukuda et al., 2012).

Recent studies in our laboratory have identified epigenetic modifications which regulate immune responses in a variety of diseases including post-traumatic stress disorder, multiple sclerosis, colitis, and liver failure (Bam et al., 2016; Busbee et al., 2015; Guan et al., 2016; Singh et al., 2014). MicroRNAs (miRNA, miR) are short (~22 nucleotide long) non-coding RNAs that post-transcriptionally inhibit protein translation by binding the 3' untranslated region (3'UTR) of target mRNAs (Bartel, 2004). Because approximately 60% of protein-coding genes are known conserved targets of miRNAs, they have emerged as

important regulators of biological functions such as immune system development and inflammatory responses (Lewis et al., 2005; Xiao and Rajewsky, 2009). DNA methylation occurs when methyl groups are added to cytosines by DNA methyltransferases (DNMT). These methylated cytosines primarily reside in CpG islands near transcription start sites and repress gene transcription by blocking binding sites for transcription factors through chromatin condensation. Importantly, DNA methylation and miRNAs have been associated with development of aging-associated pathologies including obesity, atherosclerosis, and cancer (Dong et al., 2002; Ge et al., 2014; Zhang et al., 2011).

Numerous miRNAs have already been classified to regulate differentiation and function of both adipocytes and macrophages. However, characterization of miRNA expression specifically in ATMs from lean and obese individuals has not been previously reported. Such investigation warrants merit because ATMs comprise a unique cell type due to their immunometabolic functions and dominance in the adipose tissue of obese individuals. Also, ATMs are thought to be the main initiators of obesity-induced inflammation and insulin resistance (Xu et al., 2003). In this report, we have identified dysregulated microRNAs in ATMs during obesity, which demonstrates that obese ATMs have distinct miRNA profiles that are likely to contribute to their inflammatory phenotype. Specifically, we discovered downregulation of the miR-30 family in ATMs to modulate macrophage phenotype. Our findings demonstrate that miR-30 regulates pro-inflammatory polarization of ATMs, and is likely due to regulation of DLL4-mediated Notch1 signaling. Our data also suggest therapeutic manipulation of

this miRNA family or the epigenetic mechanisms that regulate its expression, may constitute therapeutic modalities for obesity-induced inflammation, insulin resistance, and related cardiometabolic disorders.

2.3 Materials and Methods

Mice

6- to 8-week-old male and female C57Bl/6J mice and 22-week-old male C57Bl/6J mice fed either 60% kcal HFD (D12492, Research Diets), NCD (8904, Envigo Teklad), or purified 10% low-fat diet (LFD, D12450J, Research Diets) where indicated, for 16 weeks were obtained from The Jackson Laboratory and housed in a specific-pathogen-free facility. Studies were not blinded and mice were not randomized into experimental groups. At the conclusion of each study, mice were euthanized by overdose isoflurane inhalation. All procedures were performed in accordance with protocols approved by the University of South Carolina Institutional Animal Care and Use Committee.

Analytical Procedures

Body composition of lean mass, fat mass, and percent fat were measured by dual-energy x-ray absorptiometry (DEXA) (LUNAR PIXImus). Mice were placed under isoflurane anesthesia and scanned in the prone position with the head region being excluded. Body weight was monitored using an electronic gram scale with precision ± 0.1g. For glucose tolerance tests, mice underwent a 5hr morning fast before fasting glucose measurement then gavaged with 2 g/kg lean mass glucose (Sigma G7528). Blood glucose was measured 15, 30, 60 and

120m post-glucose bolus by applying approximately 5uL tail-tip blood to a glucose test strip in a glucose meter (Contour Next, Bayer).

Adipose Tissue Dissociation and ATM Isolation

To dissociate cells of the stromal vascular fraction (SVF), epididymal fat pads from 22-week-old mice were dissected, rinsed in phosphate buffered saline (PBS) and homogenized in 5mL digestion media consisting of Hank's Balanced Salt Solution (HBSS) containing 2% bovine serum albumin (BSA) and 1mg/mL collagenase (Sigma C6885) using a gentleMACs dissociator (Miltenyi Biotec). An additional 5mL digestion media was added to the homogenates and incubated 37°C, 75 RPM, 30-40m until fully dissociated. Next, 5mL complete Dulbecco's Modified Eagle's Medium and Ham's F-12 Nutrient Mixture (DMEM/F12) containing 10% FBS and 1% penicillin/streptomycin was added to the samples before filtering through a 100um nylon mesh. SVF cells were pelleted (1200 RPM, 4°C, 10m), RBC-lysed, filtered through a 70um nylon mesh and washed in complete DMEM/F12 then used immediately for desired application. To purify ATMs, SFV cells were washed twice in FACS buffer consisting of PBS, 2% heat-inactivated fetal bovine serum (FBS), and 1mM EDTA then incubated in FcR-Blocker (StemCell Tech, 18720) followed by PE-conjugated anti-F4/80 (BioLegend, Clone BM8). F4/80+ cells were immunomagnetically selected by EasySep PE positive selection kit according to manufacturer protocol including 4 total wash steps (StemCell Tech, 18557). Flow cytometry was used to verify selection purity, which was greater than 85%.

RNA Purification, cDNA Synthesis, and quantitative RT-PCR

ATMs were lysed in Qiazol and total RNA was purified using Qiagen miRNeasy Micro kit. RNA concentration and purity was measured using a NanoDrop 2000 spectrophotometer. 400ng total RNA was reverse transcribed to cDNA using Qiagen miScript II RT kit with HiFlex buffer. To validate miRNA expression by qRT-PCR, miScript SYBR Green PCR kit and miScript miRNA Primer Assays were used (Qiagen).

ATM MicroRNA and Transcriptome Microarrays

MicroRNA and transcriptome microarrays were performed using 3 biological replicates of total RNA isolated from pools of ATMs (NCD: pools of 20 mice, HFD: pools of 10 mice). For each miRNA microarray, 500 ng total RNA was polyadenylated then labeled using the Affymetrix FlashTag Biotin HSR RNA Labeling Kit. Labeled samples were hybridized to Affymetrix miRNA 4.0 chips overnight (16 h, 48°C, 60 RPM) then washed, stained, and scanned on an Affymetrix GCS 3000 system following manufacturer protocols. For transcriptome microarrays, 100ng total RNA was used as starting material. RNA was prepared for hybridization by using the Affymetrix GeneChip WT PLUS Reagent Kit according to manufacturer protocol. Labeled samples were hybridized to MTA 1.0 chips overnight (16h, 45°C, 60 RPM) then washed, stained, and scanned on an Affymetrix GCS 3000 system. Affymetrix Expression Console Version 1.4.1.46 was used for quality control, data summarization, and normalization. Affymetrix Transcriptome Analysis Console Version 3.1.0.5 was used to perform differential expression analyses. Transcripts or miRNAs were considered differentially

expressed between the two groups if linear fold change was greater than ±2 and the ANOVA p-value was less than 0.05. Heatmap figures of differentially expressed microRNAs and mRNAs were made using Genesis Version 1.7.7.(Sturn et al., 2002)

Immunofluorescence

Epididymal fat was dissected, minced (~3mm x 3mm), washed in PBS, and then fixed in 4% paraformaldehyde for 3h. Fixed tissues were permeabilized with 1% Triton X-100 for 10 min then blocked with 1% BSA and FcR-Blocker for 1h at RT. Samples were incubated with primary antibody (BioLegend: anti-F4/80-AlexaFluor488 clone: BM8, and anti-Notch1 clone: HMN1-12, or anti-DLL4 clone: HMD4-1) overnight at 4°C, then incubated with anti- Hamster IgG-AlexaFluor633 secondary antibody for 1h at RT (Invitrogen SA1-26817, Molecular Probes labeling kit A20170). Tissues were counterstained with 40uM Hoechst 33342 and 5uM BODIPY 558/568 C12 (Molecular Probes H21492 & D3835) for 1h at RT then washed and mounted on slides using a Vaseline boundary and Fluoromount-G (eBioscience, 00-4958-02).

Confocal Microscopy and Image Analysis

Confocal images of whole-mount adipose tissue were acquired on a Zeiss LSM 510 Meta Confocal Scanning Laser Microscope equipped with UV, Argon, green HeNe and red HeNe lasers. 5 random images per sample were taken using a 40X water immersion objective. Original .lsm files were imported into Fiji (Fiji Is Just ImageJ, NIH) then split into channels. Thresholds were applied to the Cy5 channel using Fiji's max Entropy algorithm to identify regions of interest

(ROIs) that express either Notch1 or DLL4. Area and intensity (mean gray value) were measured for each ROI. The product of positive signal area and intensity were used to determine total expression per image. Each biological replicate is the mean expression of 5 images. We then divided the expression values for each biological replicate by the mean of the NCD biological replicates. Therefore, data are presented as fold expression in arbitrary units (AU) with mean NCD set as control.

Flow Cytometry

Freshly isolated SVF cells or cultured BMDM were washed in FACS buffer then incubated on ice with FcR-Blocker for 10m followed by appropriate fluorochrome-conjugated antibodies or isotype controls (BioLegend, anti-CD11b-AlexaFluor488 clone: M1/70, anti-F4/80-PE clone: BM8, anti-DLL4-APC clone: HMD4-1, anti-CD45-PECy7 clone: 30-F11, anti-CD11c-APC clone: N418) for 50m. Stained cells were washed 3X in FACS buffer then analyzed on a Beckman Coulter FC500 or BD FACSCelesta flow cytometer. Plots were analyzed with Beckman Coulter CXP Software or FlowJo v10.

In Vitro Locked Nucleic Acid (LNA) Transfection Assays

Bone marrow derived macrophages (BMDM) were differentiated from bone marrow cells (BMC) by flushing the tibia and femur of 6-8 week old female C57Bl/6J mice with PBS. BMCs were filtered through a 70um nylon mesh, RBC-lysed, and washed, then cultured in complete DMEM/F12 supplemented with 10% FBS, 1% penicillin/streptomycin, 2mM L-glutamine, and 1U/mL M-CSF (BioLegend, 576406) for 7-10 days. 3T3-L1 adipocyte-conditioned media (CM-

3T3-L1A) was generated by differentiating 3T3-L1 preadipocytes into adipocytes according to the Zen-Bio 3T3-L1 Adipocyte Care Manual (ZBM0009.03). Preadipocyte medium, differentiation medium, and adipocyte maintenance medium were also used (Zen-Bio, PM-1-L1, DM-2-L1, AM-1-L1). Conditioned medium was collected between days 7 and 14 post-differentiation, 0.22um filtered, aliquoted, and stored at -80°C until use. For transfection assays, mature BMDM were plated in poly-D-lysine-coated 6-well plates at a density of $5x10^5$ cells in 2ml CM-3T3-L1A containing 10% FBS without antibiotics. BMDM were incubated 24h (37°C, 5% CO_2, 95% humidity) before transfection. Transfection complexes were prepared by diluting Lipofectamine3000 and LNA in Opti-MEM to final concentrations of 2% (v/v) and 0.32mM respectively. Mixtures were incubated 15-20m at RT to allow complexes to form. Meanwhile, conditioned BMDM were washed 3X in pre-warmed Dulbecco's PBS (DPBS), then media replaced with 2mL Opti-MEM. 500uL transfection complexes were added drop-wise to each well. Cells were incubated (37°C, 5% CO_2, 95% humidity) 5-6hr to allow LNA uptake, washed 3X in pre-warmed DPBS, then media replaced with DMEM/F12 containing 10%FBS, 1% penicillin/streptomycin, and 2mM L-glutamine, and cultured for an additional 18h. For inhibition studies, DAPT (5uM), anti-DLL4 antibody (1ug/mL), or appropriate vehicle/isotype antibody controls were added to the culture media. MirCURY LNA oligonucleotides were obtained from Exiqon. (LNA Sequences— Ctr LNA: TAA CAC GTC TAT ACG CCC A, Anti-30a: TTC CAG TCG AGG ATG TTT AC, Anti-30c: CTG AGA GTG TAG GAT GTT, Anti-30e: TCC AGT CAA GGA TGT TTA C).

Protein Extraction and Western Blotting

Cultured BMDM were washed twice in ice-cold PBS, and then directly scrapped into 100uL blue loading buffer (Cell Signaling Tech 7722) and kept on ice. Protein lysates were sonicated 10s then heated at 95°C for 5m before loading 20uL on Mini-Protean TGX Protein Gels (BioRad 4569034). Precision Plus Protein Dual Color Standards (BioRad 1610374) were loaded for a molecular weight ladder. Samples were run 40V for 30 min followed by 80V for 1.5h. Proteins were transferred to nitrocellulose membranes by using iBlot 2 NC stacks and the ThermoFisher iBlot 2 western transfer system running the P0 protocol (20V 1m, 23V 4m, then 25V 2m). Membranes were blocked in 5% dry milk or 5% BSA for 1h then washed 3X in Tris-buffered saline containing 0.1% Tween-20 (TBS-T). Membranes were incubated in primary antibody overnight at 4°C with gentle shaking then washed 3 x 5m in TBS-T. Membranes were incubated in secondary antibody for 1h at RT, then washed 3 x 5m in TBS-T before addition of ECL substrate and exposure to x-ray film. Films were scanned and densitometry measurements were made using ImageJ gel analysis features (NIH).

Enzyme-linked Immunosorbent Assays (ELISA)

Culture supernatants were aspirated and centrifuged 5000 RPM, 5m, 4°C to rid of debris then aliquoted and stored -80°C before assaying. DLL4 ELISA kits were purchased from Abcam (ab213860). Mouse TNFα and CCL2 ELISA kits were purchased from BioLegend (TNFα 530901 & CCL2 432701). Assays were

performed according to manufacturer protocols and plates were read at 450nm. Concentrations were calculated using standard curves.

Methylated DNA Immunoprecipitation Sequencing (MeDIP-seq)

MeDIP-seq libraries were generated from ATM DNA as previously described and sequenced with single-end reads of 75bp on an Illumina NextSeq500 (Bam et al., 2015). Data analysis was performed as previously described (Bam et al., 2015). Mapped reads were analyzed using MEDIPS software (Lienhard et al., 2014). Peaks were visualized in the Integrated Genome Browser (Freese et al., 2016). The UCSC genome browser was used to locate CpG islands within 10kb of miR-30 gene coding regions (Kent et al., 2002).

Methylation-specific PCR

Genomic DNA from NCD and HFD ATMs were isolated using Qiagen AllPrep DNA/RNA/miRNA Universal Kit (80224). Bisulfite conversion of DNA was performed using Qiagen EpiTect Fast DNA Bisulfite Kit (59824). PCR using methylated and unmethylated primers specific for the *Nfyc* CpG island (Methylated: Fwd—TTC GTT AAT GGG AGA AAG TTC Rev—CTA CCG CCG CCA TAT TAT A Unmethylated: Fwd—TTT TTT GTT AAT GGG AGA AAG TTT, Rev—ACT CTA CCA CCA CCA TAT TAT A). Primers were designed using ThermoFisher Methyl Primer Express Software v1.0. BioRad iQ SYBR Green Supermix was used and qRT-PCR was run using the following reaction conditions: initial denaturation- 95°C 5m followed by 31 cycles of- 95°C 15s, 49.8°C 30s, and 70°C 35s. PCR products were run on a 1.5% agarose gel and

bands were quantified using FIJI gel analysis features. Methylation ratio was determined by dividing methylated by unmethylated quantities (M/U).

Lentiviral Overexpression of miR-30a-5p in the RAW264.7 macrophage cell line

MicroRNA lentiviral expression vectors were purchased from Applied Biological Materials (ABM) (Cat No. m001 and mm10332) and then amplified in DH5α competent cells. Amplified plasmid DNA was isolated using Qiagen EndoFree Plasmid Maxi Kit. Lentiviruses were produced in HEK293T cells using ABM's 3rd generation packaging mix and Lentifection transfection reagent (Cat no. LV053 and G074). Lentiviruses were collected from the culture supernatant and cellular debris was pelleted by centrifugation at 3000 rpm for 15 min at 4°C. The cleared supernatant was filtered through a 0.45um PVDF sterile filter. The viral titer was determined by ABM qPCR titration kit (Cat no. LV900-S). Lentivirus aliquots were stored at -80°C. RAW264.7 target cells were transduced with lentivirus at a multiplicity of infection of 2.5. 48hr following transduction, culture supernatants were collected for TNFα and CCL2 ELISAs and the cells were stained for flow cytometry.

Statistical Analysis

Statistical analyses were performed using GraphPad Prism Version 7.000 for Mac, GraphPad Software, La Jolla California USA, www.graphpad.com. Values are expressed as mean ± standard error. Two-tailed Student's t tests were performed for paired analyses. One-way ANOVA with a Bonferroni post hoc correction were used for multiple group analyses. The null hypothesis was rejected if $p<0.05$. All experiments were repeated at least twice, unless otherwise

indicated in each figure legend. Detailed sample sizes are provided in each figure legend. Sample sizes were chosen by power analysis based on pilot studies.

2.4 RESULTS

Obesity Promotes ATM miRNA Dysregulation and Pro-Inflammatory Phenotype

To study ATMs associated with obesity (will be referred to as obese ATMs), we used a high-fat diet (HFD)-induced obesity model whereby 6-week-old male C57BL/6J mice were fed HFD or normal chow diet (NCD) for 16 weeks to generate diet-induced obese and lean control mice. HFD-fed mice more than doubled their body weight during 16 weeks of feeding whereas NCD-fed mice increased their weight by ~3% (Figures 2.1A-2.1C), and HFD-induced weight gain occurred due to selective increases in fat mass (Figure 2.1C). As expected, HFD also caused glucose intolerance measured by glucose tolerance test (GTT) (Figures 2.1D and 2.1E).

While phenotyping ATMs, we observed percentages of ATMs ($F4/80^+/CD11b^+$) and $CD11c^+$ ATMs in epididymal fat of obese mice were more than 2 and 4 fold that of lean mice respectively (Figure 2.1F and 2.1G). To identify gene expression alterations in HFD and NCD ATMs we performed transcriptome microarrays using F4/80+ cells from epididymal fat of HFD and NCD mice. Principal component analysis (PCA) displayed HFD and NCD ATMs have distinct transcript expression profiles (Figure 2.2A). HFD ATMs exhibited increased M1- and decreased M2-associated gene expression (Figure 2.1H and Table 2.1). Notably, *Irf8*, which encodes a transcription factor activated by Notch-

RBPJ signaling, as well as *Itgax*, which encodes the M1 surface marker CD11c, were upregulated in obese ATMs (Lumeng et al., 2007; Xu et al., 2012). Alternatively, *Klf4*, which encodes Krüppel-like factor 4 that cooperates with STAT6 to promote M2 polarization, and *Adipor2*, which encodes a receptor for the anti-inflammatory adipokine adiponectin, were downregulated in obese ATMs (Liao et al., 2011; van Stijn et al., 2015). Together these observations suggested that HFD ATM phenotype was skewed towards M1.

To identify differentially expressed miRNAs in ATMs during obesity, we performed miRNA microarrays using F4/80+ cells isolated from epididymal fat of HFD and NCD mice. PCA showed HFD and NCD ATMs have distinct miRNA expression profiles (Figure 2.2B). In total, there were 37 down- and 12 up-regulated miRNAs in HFD versus NCD ATMs (Figures 2.1I, 2.1J and Table 2.1). Additionally, transcriptome microarrays showed there were 946 down- and 920 up-regulated transcripts in HFD versus NCD ATMs. Of these, 216 and 273 coding genes were up- and down-regulated respectively (Figure 2.2C). We performed core analysis on these dysregulated miRNAs and transcripts using Ingenuity Pathway Analysis and observed significant overlap with canonical pathways including hepatic fibrosis and atherosclerosis signaling, disorders such as cancer and hepatic disease, cellular functions including movement and survival, and toxic effects including cardiotoxicity, hepatotoxicity, and nephrotoxicity (Figures 2.2D-2.2H).

Upon closer examination of dysregulated miRNAs during obesity, we observed downregulation of miR-322-5p (-17.1 linear FC) and miR-155-5p (-

14.19 linear FC), which have been previously characterized for their involvement in macrophage functions (O'Connell et al., 2007; Zhang et al., 2017). Interestingly, we also noted downregulation of miRs -30a-5p, -30c-5p, and -30e-5p in HFD ATMs (-12.27 combined linear FC) when compared to NCD ATMs, thereby indicating that the miR-30 family may play a role in macrophage polarization (Figures 2.1I-2.1M).

The miR-30 target DLL4 is associated with ATM inflammation

When we looked at potential target molecules for miR-30, we found through in silico analyses that it may target the 3'UTR of *Dll4* (Figures 2.3A-2.3C). Previous studies had confirmed miR-30-*Dll4* targeting using luciferase reporter assay (Bridge et al., 2012; Shan et al., 2016). Interestingly, DLL4 has been shown to be involved in Notch signaling (Fukuda et al., 2012; Fung et al., 2007; Nakano et al., 2016). To that end, we evaluated expression of Notch1 and the miR-30 target DLL4 in adipose tissue. Notch1 and DLL4 were visualized in whole-mounted epididymal fat by confocal microscopy (Figures 2.4A and 2.4C). Adipose tissue expression of DLL4 but not Notch1 was elevated in HFD-fed mice (Figures 2.4B and 2.4D). Flow cytometry analysis of epididymal fat stromal vascular fractions (SVF) was then used to confirm that DLL4 expression was elevated on ATMs ($CD45^+/CD11b^+/F4/80^+/DLL4^+$) (Figures 2.4E and 2.4F). Specifically, elevated DLL4 expression was most pronounced in the $CD45^+/CD11b^{int}/F4/80^+$ subset of infiltrating ATMs (Figure 2.4F).

MiR-30 Inhibition Promotes DLL4-Notch Signaling-Induced Inflammation in Macrophages

To further demonstrate involvement of miR-30 in regulation of DLL4-mediated Notch signaling and pro-inflammatory response in macrophages, we developed an in vitro assay to mimic the downregulated miR-30 expression observed in vivo in obese ATMs. To that end, naïve bone marrow derived macrophages (BMDM) were cultured in conditioned medium from differentiated 3T3-L1 adipocytes (CM-3T3-L1A) to confer an ATM-like phenotype, and then transfected with miRNA inhibitor locked nucleic acids (LNA) which targeted miRs-30a-5p (Anti-30a), -30c-5p (Anti-30c), and -30e-5p (Anti-30e) (Figure 2.5A). BMDM transfected with Anti-30a, Anti-30c, and Anti-30e LNAs had decreased expression of miRs -30a-5p, -30c-5p, and -30e-5p relative to Mock and control LNA (Ctr LNA)-transfected controls, although the inhibitors displayed some cross-reactivity (Figure 2.6). Anti-30a, Anti-30c, and Anti-30e transfection increased DLL4 and activated Notch1 intracellular domain (N1ICD) expression compared to Mock and Ctr LNA (Figures 2.5B and 2.5C). Pro-inflammatory cytokines TNFα and CCL2 were also elevated in culture supernatants of inhibitor-transfected cells (Figures 2.5D and 2.5E). Moreover, miR-30 inhibitors promoted increased surface expression of CD11c (Figures 2.5F and 2.5G). Treatment of transfected cells with the Notch/γ-secretase inhibitor DAPT reduced induction of CD11c in miR-30 inhibitor-transfected cells (Figures 2.7A and 2.7B). Specific blockade of DLL4 signaling using anti-DLL4 antibody also reduced induction of pro-inflammatory cytokines TNFα and CCL2 in miR-30 inhibitor-transfected cells

(Figures 2.7C and 2.7D). Conversely, lentiviral overexpression of miR-30a-5p in the RAW264.7 macrophage cell line reduced M1 polarization evidenced by decreased expression of CD11c and decreased TNFα and CCL2 production (Figure 2.8). Together these data demonstrated that miR-30 plays an anti-inflammatory role in macrophages by regulating DLL4-Notch1 signaling, M1 polarization and pro-inflammatory cytokine production in macrophages.

Evidence for DNA Methylation-Dependent Regulation of miR-30

Epigenetic modifications can occur due to various environmental factors such as stress, aging, and diet. Because this study involved diet-induced obesity, we investigated epigenetic mechanisms that may control miR-30 expression in ATMs. Data from transcriptome microarrays enriched for epigenetic modification enzymes and factors revealed that gene expression of *Dnmt1* and *Dnmt3a* were upregulated in ATMs of HFD vs. NCD-fed mice (Figure 2.9A). Therefore, we investigated DNA methylation intensity of miR-30 gene regions. *Mir30c-1* and *mir30e* are located within the same intron of the *Nfyc* gene, which contains a CpG island in it's promoter region. *Mir30a* and *mir30c-2* are intergenic miRNA genes that do not have any nearby CpG islands, therefore we were not able to identify DNA methylation as a potential epigenetic mechanism regulating their expression. We performed methylated-DNA immunoprecipitation sequencing (MeDIP-seq) to screen genome-wide DNA methylation in ATMs and found DNA hypermethylation in the *Nfyc*-promoter CpG island in HFD- versus LFD-ATMs indicating expression of miRs -30c and -30e may be regulated by DNA methylation. This was validated in NCD- and HFD- ATMs by methylation-specific

PCR (Figure 2.9C). Together, these data indicated DNA methylation-dependent downregulation of miR-30 may promote pro-inflammatory polarization of adipose tissue macrophages during obesity (Figure 2.10).

2.5 DISCUSSION

There is a clear association between pro-inflammatory ATM polarization and insulin resistance during HFD-induced obesity. However, miRNA-mediated epigenetic mechanisms regulating ATM phenotype have not been well characterized. Our results unveil a role for the miR-30 family in modulating polarization of macrophages in visceral adipose tissue through regulation of the Notch1 ligand DLL4. Furthermore, we identified that DNA methylation may play a role in attenuating miR-30 expression. Jointly, these findings suggest important roles for miRNAs and DNA methylation in regulation of ATM polarization and obesity-induced insulin resistance.

DLL4 is a canonical Notch1 ligand that is linked to macrophage inflammation and metabolic disorders. DLL4 promotes M1 macrophage polarization (Fung et al., 2007; Nakano et al., 2016). Blockade of DLL4 by administration of anti-DLL4 antibody in mice attenuates atherosclerosis and metabolic disease by decreasing macrophage infiltration and inflammatory response (Fukuda et al., 2012). Interestingly, Notch signaling is also linked to insulin resistance (Bi et al., 2014; Pajvani et al., 2011). Conditional knockout of Notch1 or its downstream transcription factor RBP-J in adipocytes ameliorates obesity and insulin resistance by promoting white adipose tissue browning and

energy expenditure in mice (Bi et al., 2014). These findings suggest that downregulation of the DLL4-Notch1 axis may hold significant therapeutic potential for various inflammatory and metabolic disorders. Furthermore, identification of regulatory mechanisms controlling this pathway could reveal therapeutic targets for cardiometabolic disorders. In the current study, we identified epigenetic regulatory mechanisms of this pathway in ATMs.

Growing bodies of evidence suggest miRNA dysregulation and aberrant DNA methylation play pathogenic roles in clinical disorders such as type II diabetes, atherosclerosis, and cancer. Inflammation is many times the underlying cause for these chronic diseases, and macrophages are key mediators of chronic-inflammation. Additionally, obesity is well known to greatly increase risk for these diseases. Because ATMs are a primary source of pro-inflammatory cytokines that initiate chronic sub-clinical inflammation during obesity, ATMs contribute to progression towards comorbid diseases. In the current study, we observed increased infiltration and pro-inflammatory polarization of macrophages in visceral adipose tissue. When we performed core analysis of dysregulated miRNAs and transcripts in ATMs during diet-induced obesity, we found significant overlap with cardiometabolic disease processes and cancer, which suggests that ATM-inflammation is tightly linked to the development of comorbid diseases.

Recent reports have linked specific miRNAs to obesity as well as macrophage polarization. In the context of obesity, expression profiles of human adipose tissue have identified miRNAs such as miR-132 and miR-17-5p to be

involved in regulation of adipocyte growth and insulin resistance (Klöting et al., 2009). In macrophage polarization, miR-146a and miR-155-5p are classified to be negative regulators of inflammatory responses to the bacterial endotoxin lipopolysaccharide (Taganov et al., 2006). MicroRNA expression profiles of whole adipose tissue and in vitro polarized macrophages have been previously reported, however dysregulated miRNAs between lean and obese ATMs have not been characterized (Ge et al., 2014; Klöting et al., 2009; Zhang et al., 2013). ATMs form heterogenous populations and their inflammatory status greatly influences adipose insulin sensitivity. In the current study, the miRNAs that exhibited the most significant fold change in ATMs were miR-322-5p and miR-155-5p. miR-322-5p is well characterized to inhibit pro-inflammatory cytokine production in macrophages, while miR-155-5p is also known to be involved in a variety of macrophage processes (O'Connell et al., 2007; Zhang et al., 2017). Most strikingly, we observed downregulation of several miR-30 family miRNAs in ATMs during obesity, yet this miR family has not been previously investigated for its role regulating macrophage phenotype. The miR-30 family is highly conserved and known to target the Notch1 ligand DLL4, which is a ligand that contributes to metabolic disease and macrophage inflammation (Bridge et al., 2012; Fukuda and Aikawa, 2013; Fukuda et al., 2012; Fung et al., 2007; Nakano et al., 2016; Shan et al., 2016). We observed upregulation of DLL4 on obese ATMs. Moreover, inhibiting miR-30 in vitro triggered DLL4-Notch1 signaling and pro-inflammatory response in macrophages, and blocking DLL4-Notch1 signaling could lessen this effect. Overexpression of miR-30a-5p also decreased M1

polarization in the RAW264.7 macrophage cell line. Thus, we have observed that miR-30 is involved in attenuating M1 macrophage activation through regulation of the DLL4-Notch signaling pathway. These data suggest that miR-30 induction holds therapeutic potential for regulating macrophage-driven inflammatory and metabolic disorders. Furthermore, regulatory mechanisms of the miR-30 family warrant further investigation due to emerging advances in epigenetic therapies and targeted personalized medicine.

To investigate the mechanisms through which obesity downregulates miR-30 in ATMs, we focused on epigenetic regulation. We observed elevated expression of DNMTs and DNA hypermethylation in miR-30-associated CpG islands in obese vs. lean ATMs. Thus, HFD may trigger DNA hypermethylation of miR-30 genes leading to downregulation of miR-30 to allow increased expression of DLL4 and Notch signaling-induced inflammation and insulin resistance during obesity. Our findings are summarized as an illustrative summary in Figure 2.10.

Previous studies have suggested that miR-30 induction has metabolic benefits. MicroRNA-30c attenuates hyperlipidemia, hypercholesterolemia, and atherosclerosis in mice, while miR-30b/c promotes thermogenesis and white adipose tissue browning (Hu et al., 2015; Irani et al., 2016; Soh et al., 2013). These findings suggest that in vivo manipulation of the miR-30 family holds promise for therapeutic intervention of obesity-related disorders. Additionally, macrophage polarization plays key roles in regulation of both brown adipose tissue metabolism and inflammation during atherosclerosis, yet macrophage phenotype was not assessed in the aforementioned studies (Moore et al., 2013;

Qiu et al., 2014; Rao et al., 2014). Our data suggest that macrophage-specific miR-30 regulates polarization towards inflammatory phenotype and progression of chronic macrophage-driven inflammatory disorders. Thus, future studies targeting macrophage-specific miR-30 in vivo could shed new light on mechanistic and therapeutic potential of this miR family in attenuating obesity and other metabolic disorders.

Table 2.1 Dysregulated miRNAs and macrophage polarization genes

miRNA or Gene	Linear Fold Change (HFD vs. NCD)	ANOVA p-value
mmu-miR-221-3p	2.54	0.00007
mmu-miR-222-3p	3.19	0.000424
mmu-miR-714	3.23	0.000954
mmu-miR-6240	2.69	0.001063
mmu-miR-342-3p	2.21	0.004268
mmu-miR-2137	2.02	0.018981
mmu-miR-1895	2.45	0.021364
mmu-miR-494-3p	2.23	0.022023
mmu-miR-1894-5p	2.76	0.025895
mmu-miR-6906-5p	3.47	0.035544
mmu-miR-7088-5p	2.09	0.037997
mmu-miR-668-5p	3.06	0.04592
mmu-miR-7036-5p	-3.07	0.000096
mmu-miR-15a-3p	-2.26	0.002774
mmu-miR-145a-5p	-8.58	0.003083
mmu-miR-150-5p	-4.02	0.00323
mmu-miR-30a-3p	-13	0.004316
mmu-miR-143-3p	-12.28	0.004959
mmu-miR-210-3p	-2.7	0.008072
mmu-miR-511-3p	-2.87	0.010394
mmu-miR-7069-5p	-2.94	0.012634
mmu-miR-155-5p	-14.19	0.013576
mmu-miR-3473f	-2.79	0.014766
mmu-let-7e-5p	-3.21	0.017401
mmu-miR-100-5p	-7.38	0.018074
mmu-miR-669m-5p	-4.26	0.022299
mmu-miR-466m-5p	-4.26	0.022299
mmu-miR-200c-3p	-6.1	0.024927
mmu-miR-30e-5p	-3.65	0.026714
mmu-miR-322-5p	-17.1	0.029387
mmu-miR-30a-5p	-5.22	0.03013
mmu-miR-143-5p	-2.61	0.030279
mmu-miR-1934-3p	-2.34	0.030372
mmu-miR-138-5p	-7.82	0.031309
mmu-miR-30c-5p	-3.4	0.031619
mmu-miR-671-5p	-2.42	0.033095
mmu-miR-192-5p	-5.91	0.033668
mmu-miR-700-3p	-2.19	0.037904
mmu-miR-99b-5p	-3.29	0.038033

miRNA or Gene	Linear Fold Change (HFD vs. NCD)	ANOVA p-value
mmu-miR-199a-3p	-2.47	0.040407
mmu-miR-199b-3p	-2.47	0.040407
mmu-let-7b-5p	-3.6	0.042523
mmu-miR-195a-5p	-5.2	0.043074
mmu-miR-29c-3p	-2.45	0.043942
mmu-let-7f-5p	-2.05	0.04436
mmu-miR-320-3p	-2.24	0.044977
mmu-miR-203-3p	-6.67	0.045282
mmu-miR-6971-5p	-2.15	0.048055
mmu-miR-152-3p	-2.62	0.049714
Gsn	2.12	9.56E-07
Itgax	3.99	0.002376
Irf8	2.39	0.007543
Il1rn	3.73	0.007581
Pak1	3.83	0.007639
Mmp12	2.43	0.008177
Ccr3	2.01	0.009267
Ifngr1	2.17	0.033921
Cd44	2.39	0.040322
Ccr5	2.4	0.040445
Ccr5	2.4	0.040445
Cd209f	-16.43	0.000237
Cd209d	-21.07	0.000383
Cd209b	-10.21	0.000414
Klf4	-5.52	0.000488
Cd209e	-2.69	0.001121
Cd209a	-8.22	0.001402
Mtus1	-2.1	0.003759
Cd209c	-4.38	0.005042
Adipor2	-2.06	0.01107
Mmp9	-8.58	0.012721
Nt5e	-2.13	0.01318
Csf1	-2.89	0.01473
Junb	-3.04	0.01674
Icam1	-2.42	0.021615
Cav1	-3.47	0.028567
Chil3	-2.75	0.044279
S1pr1	-4.61	0.047906

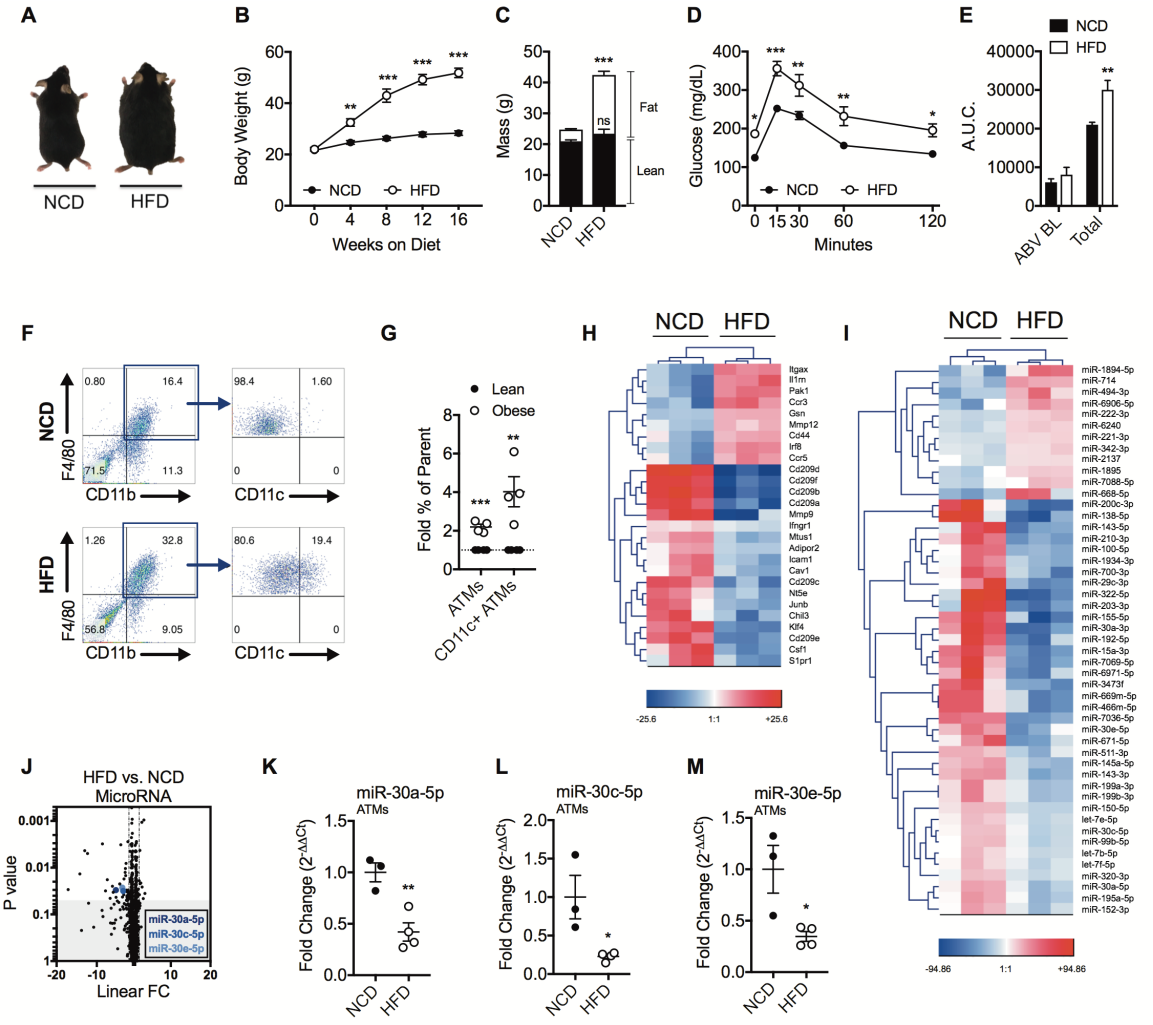

Figure 2.1 HFD-Induced Obesity Stimulates ATM Inflammation and miRNA Dysregulation.

To study HFD-induced obesity, male C57BL/6J mice were fed NCD or HFD for 16 weeks until 22-weeks-old. (A) Representative photo of mice after 16 weeks of NCD or HFD feeding. (B) Weekly measurements of body weight growth. (C) DEXA body composition after 16 weeks of diet. (D) Oral glucose tolerance test (GTT) after 16 weeks of diet. (E) Area under the curve (A.U.C.) for GTT. Represented are A.U.C. above baseline (ABV BL) or total A.U.C. (F) Flow cytometry dot plots of F4/80$^+$/CD11b$^+$/CD11c$^+$ ATMs in the epididymal fat stromal vascular fraction (SVF) of NCD- or HFD-fed mice. (G) Fold percentage increase quantification of F4/80$^+$/CD11b$^+$ cells in the SVF (denoted as "ATMs") and CD11c$^+$ ATMs. Lean mice were fed either NCD or 10% low-fat diet (LFD). Obese mice were fed 60% HFD. (H-J) Pooled F4/80$^+$ ATMs from epididymal fat were used for transcriptome and miRNA microarrays. (H) Transcriptome microarray heatmap of differentially expressed mRNAs in ATMs related to macrophage polarization. (I) MicroRNA heatmap of differentially expressed miRNAs in ATMs. (J) MicroRNA array volcano plot depicting linear fold change (FC) vs. ANOVA p-

value significance. (K-M) qRT-PCR expression validation of miRs 30a-5p, 30c-5p, and 30e-5p. For (A-F), the values are shown as mean ± SEM and are from a single experiment representative of at least 3 independent experiments with 5 mice per experimental group. For (G) data shown as mean ± SEM of 4 independent experiments with 5 mice per experimental group. For (H-M), the data shown are mean ± SEM and are from 3-4 independent experiments with 20 pooled NCD mice and 10 pooled HFD mice per experiment. Statistical differences were determined by using Student's t-test. *$p<0.05$, **$p<0.01$, ***$p<0.001$.

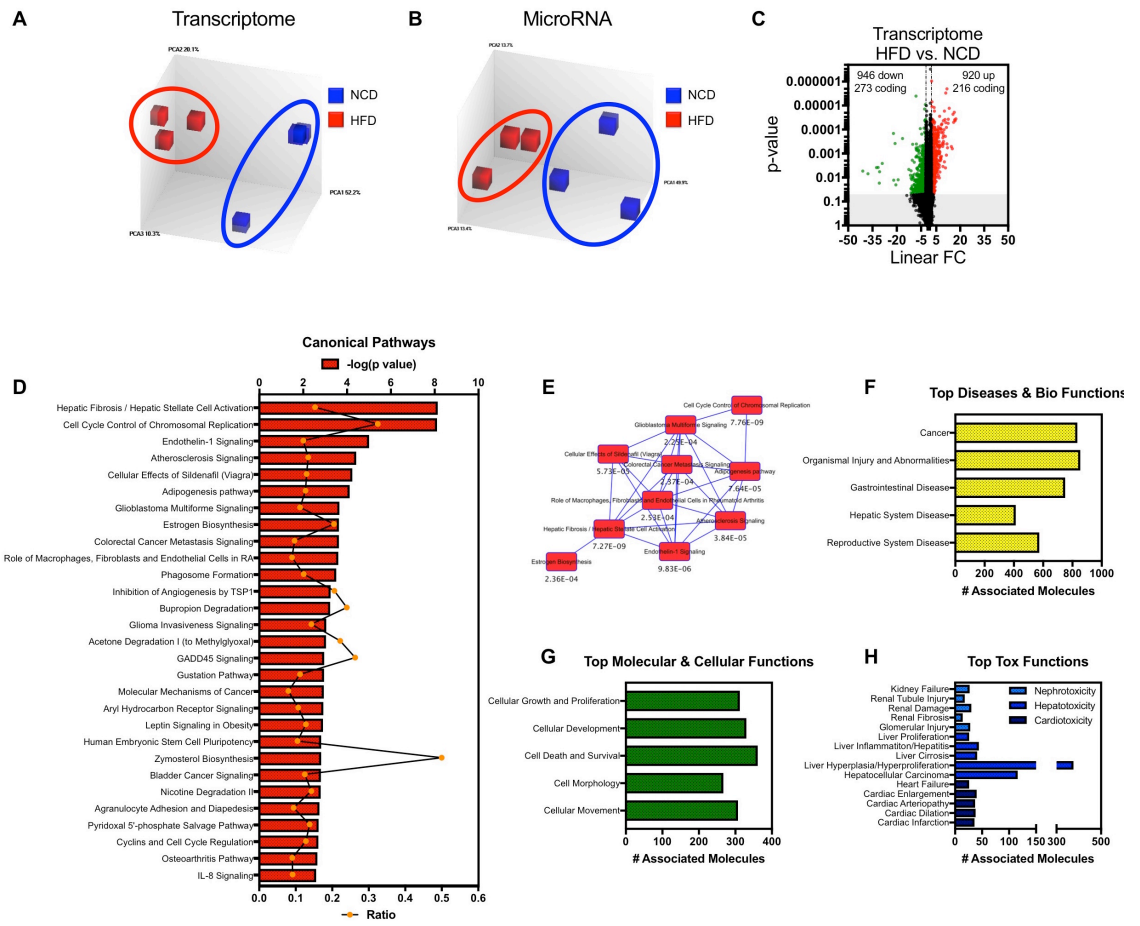

Figure 2.2 HFD-Induced Obesity Elicits Distinct Transcript and miRNA Expression Profiles in ATMs.

As described in Figure 2.1 legend, F4/80+ ATMs were isolated from 22-week-old HFD and NCD mice and used for miRNA and transcriptome microarrays. (**A**) PCA plot of ATM transcriptome microarray signal. NCD and HFD ATMs cluster distinctly. (**B**) PCA plot of ATM microRNA microarray signal. NCD and HFD ATMs form distinct clusters. (**C**) Volcano plot of differentially expressed transcripts. (**D-H**) Ingenuity Pathway Analysis (IPA) was used to perform a core analysis on dysregulated transcripts and miRNAs observed in HFD ATMs. (**D**) The top associated canonical pathways are presented with their overlap ratio and p-values. (**E**) Network of overlapping canonical pathways. P-values for each canonical pathway are presented under each node. (**F-H**) The top diseases and bio functions (**F**), molecular and cellular functions (**G**), and toxicological functions (**H**) are presented with their number of associated molecules observed to be dysregulated in HFD ATMs. The data shown are representative of 3 independent experiments with 20 pooled NCD mice and 10 pooled HFD mice per experiment.

A

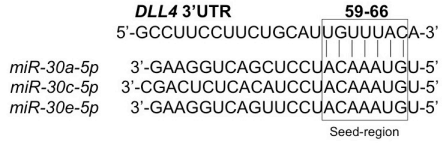

B

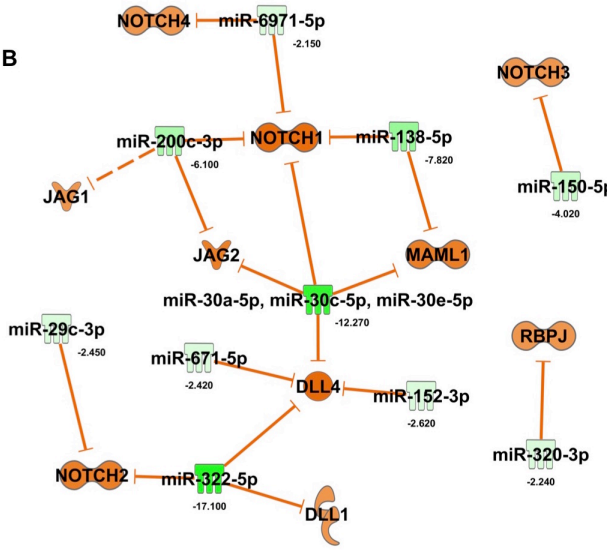

C

DLL4 3'UTR target pairing predictions:

MicroRNA Name	Observed Fold Change (HFD vs. NCD)	ANOVA p-value	Site Type	Position in 3'UTR	Seed Sequence	TargetScan Context Score	microRNA.org mirSVR Score	miRDB Target Score
miR-30a-5p	-5.22	0.030	8mer	59-66	ACAAAUG	-0.29	-1.0845	95
miR-30c-5p	-3.40	0.032	8mer	59-66	ACAAAUG	-0.28	-1.0820	95
miR-30e-5p	-3.65	0.027	8mer	59-66	ACAAAUG	-0.29	-1.0845	95
miR-322-5p	-17.1	0.029	7mer-m8	102-108	ACGACGA	-0.14	-0.1259	73

Notch1 3'UTR target pairing predictions:

MicroRNA Name	Observed Fold Change (HFD vs. NCD)	ANOVA p-value	Site Type	Position in 3'UTR	Seed Sequence	TargetScan Context Score	microRNA.org mirSVR Score	miRDB Target Score
miR-30a-5p	-5.22	0.030	7mer-A1	1490-1496	CAAAUG	-0.27	-0.2977	N/A
miR-30c-5p	-3.40	0.032	7mer-A1	1490-1496	CAAAUG	-0.33	-0.2951	N/A
miR-30e-5p	-3.65	0.027	7mer-A1	1490-1496	CAAAUG	-0.28	-1.2676	N/A

MAML1 3'UTR target pairing predictions:

MicroRNA Name	Observed Fold Change (HFD vs. NCD)	ANOVA p-value	Site Type	Position in 3'UTR	Seed Sequence	TargetScan Context Score	microRNA.org mirSVR Score	miRDB Target Score
miR-30a-5p	-5.22	0.030	8mer	1936-1943	ACAAAUG	-0.32	-1.2264	95
miR-30c-5p	-3.40	0.032	8mer	1936-1943	ACAAAUG	-0.36	-1.2264	95
miR-30e-5p	-3.65	0.027	8mer	1936-1943	ACAAAUG	-0.32	-1.2236	95

JAG2 3'UTR target pairing predictions:

MicroRNA Name	Observed Fold Change (HFD vs. NCD)	ANOVA p-value	Site Type	Position in 3'UTR	Seed Sequence	TargetScan Context Score	microRNA.org mirSVR Score	miRDB Target Score
miR-30a-5p	-5.22	0.030	8mer	334-341	ACAAAUG	-0.19	N/A	N/A
miR-30c-5p	-3.40	0.032	8mer	334-341	ACAAAUG	-0.17	N/A	N/A
miR-30e-5p	-3.65	0.027	8mer	334-341	ACAAAUG	-0.17	N/A	N/A

Figure 2.3 MicroRNA-30 targets the Dll4 3'UTR.
As shown in Figures 2.1 and 2.4, miR-30 expression is down and DLL4 is up in HFD versus NCD ATMs. miR-30 target pairing predictions were explored using online databases and pathway analysis. (A) Targetscan.com seed sequence alignment of miRs -30a-5p, -30c-5p, and -30e-5p with the Dll4 3'UTR. (B) IPA network of dysregulated miRNAs in HFD ATMs and predicted of Notch signaling gene targets. miR-30 and miR-322-5p had the highest negative FC values of miRs predicted to target Dll4. (C) 3'UTR alignment scores from 3 online databases.

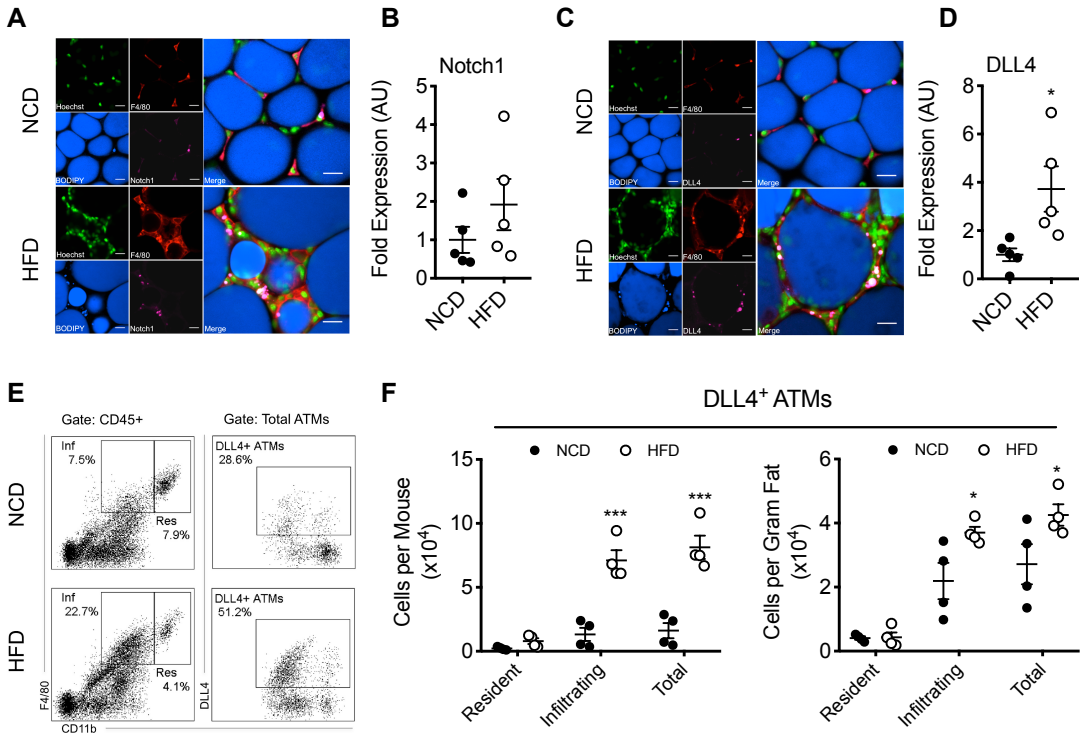

Figure 2.4 DLL4 Expression is Elevated in Obese ATMs.
HFD-induced obesity was studied as described in Figure 2.1 legend. At 22-weeks-old, visceral adipose tissue and adipose SVF were analyzed for DLL4 expression. (A&C) Immunofluorescent staining of whole-mount epididymal fat. Scale bar = 20 μm. Presented are representative confocal micrographs of Notch1 (A) or DLL4 (C). (B&D) Image quantification of Notch1 (B) or DLL4 (D) in adipose tissue. The values are shown as mean ± SEM and are from a single experiment representative of 2 independent experiments with 5 mice per experimental group. (E) Flow cytometry dot plots of DLL4+ ATMs in epididymal fat. $CD11b^{int}$ are denoted as infiltrating ("Inf") and $CD11b^{hi}$ are denoted as resident ("Res"). (F) Quantification of DLL4+ ATM cell counts represented per mouse and per gram fat. Values are presented as mean ± SEM and are from a single experiment representative of 2 independent experiments with 4 biological replicates (pools of 1-6 mice) per experimental group. Statistical significance was determined by Student's t-test. *p<0.05, **p<0.01, ***p<0.001.

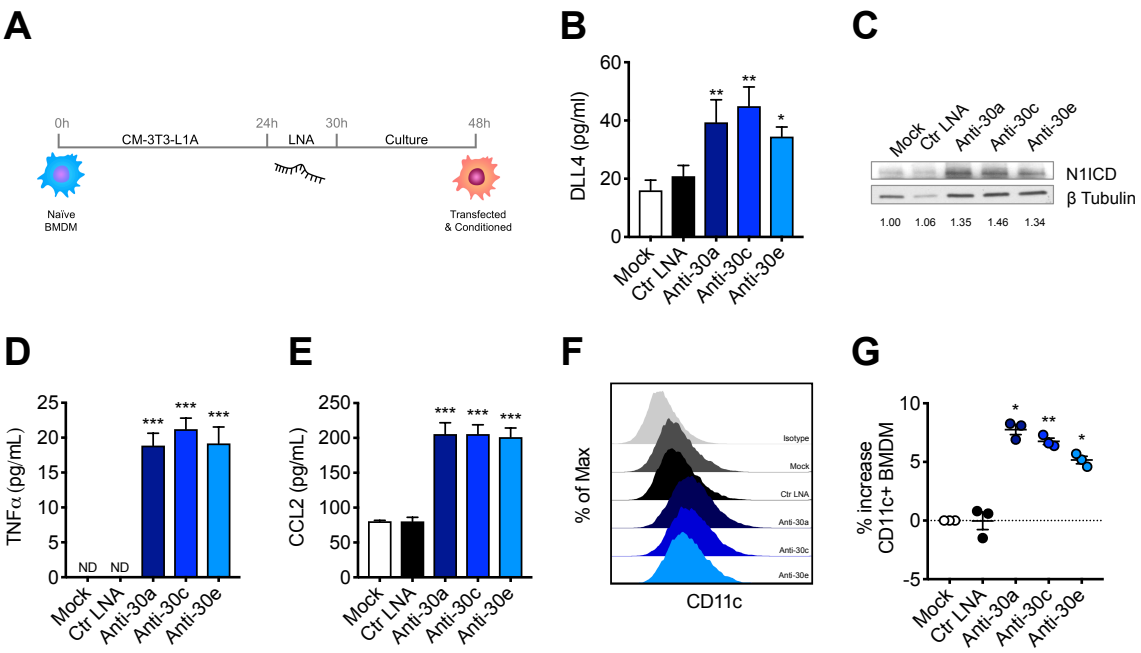

Figure 2.5 miR-30 Inhibition Induces DLL4-Notch1 Signaling and M1 polarization.
BMDM were differentiated from the bone marrow of normal mice then used to study in vitro consequences of miR-30 inhibition on Notch signaling and macrophage polarization. (A) Schematic of in vitro experimental timeline. Differentiated BMDM were incubated in CM-3T3-L1A prior to transfection with microRNA inhibitor LNA and subsequent culture. Cells and supernatants were harvested at 48h. (B) DLL4 detected in culture supernatants by ELISA. (C) Western blot of cleaved/activated Notch1 (N1ICD). Fold induction relative to Mock is represented below each lane. (D-E) Pro-inflammatory cytokines TNFα (D), and CCL2 (E) detected in culture supernatants by ELISAs. (F) Flow cytometry histograms of CD11c expression in transfected BMDM. (G) Percentage increase in CD11c+ macrophages. For figures B-F, values are presented as mean ± SEM and are from a single experiment representative of 2-3 independent experiments. For figure E, data presented are mean ± SEM of 3 independent experiments. Statistical significance was determined by one-way ANOVA with Bonferroni post hoc correction. *p<0.05, **p<0.01, ***p<0.001 vs. Mock.

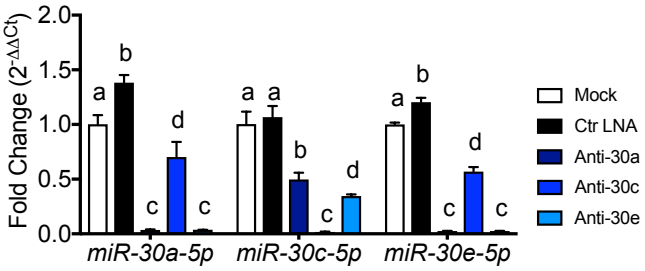

Figure 2.6 MicroRNA-30 Inhibitor LNAs downregulate miR-30 Expression.
As described in Figure 2.5 BMDM were transfected with miR-30 inhibitor LNAs. qRT-PCR estimation of miR-30 knockdown in LNA-transfected BMDMs. miR-30-5p inhibitor LNAs decrease expression of their designated mature miRs however they do display some cross-reactivity to other miR-30 family miRs. Values presented are mean ±SEM and are from a single experiment representative of 2 independent experiments. Statistical significance was determined by one-way ANOVA with Bonferroni post hoc correction. For pairwise comparisons, $p<0.05$ if letter differs between the groups being compared.

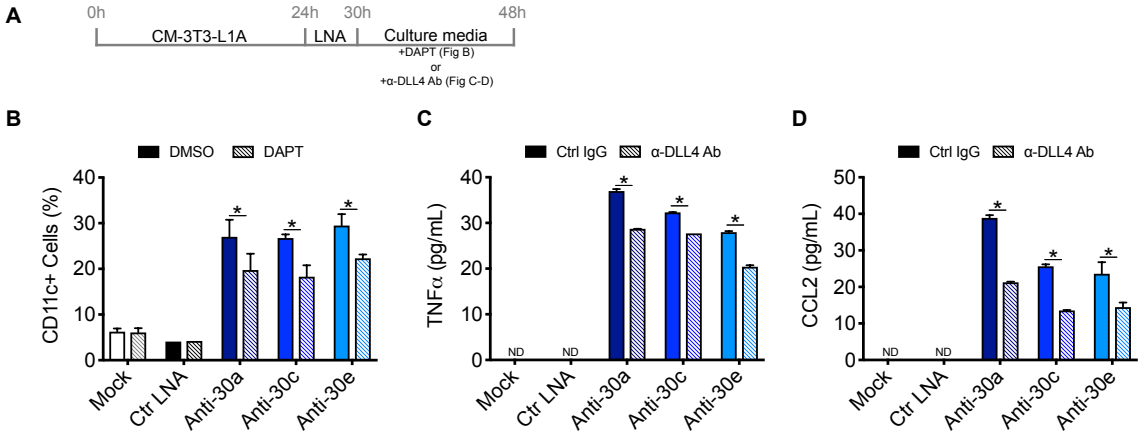

Figure 2.7 Inhibition of DLL4-Notch signaling lessens inflammation in miR-30 inhibitor-transfected macrophages.
Bone marrow derived macrophages were transfected with LNA as performed in Figure 2.5, and then cultured in the presence of vehicle (DMSO), the Notch/γ-secretase inhibitor DAPT, control IgG (Ctrl IgG), or anti-DLL4 antibody (α-DLL4 Ab, clone: HMD4-1). (**A**) Experimental timeline. (**B**) Flow cytometry percentage of CD11c+ M1 macrophages. (**C**) TNFα concentration in cellular supernatant measured by ELISA. (**D**) CCL2 concentration in cellular supernatant measured by ELISA. *$p<0.05$

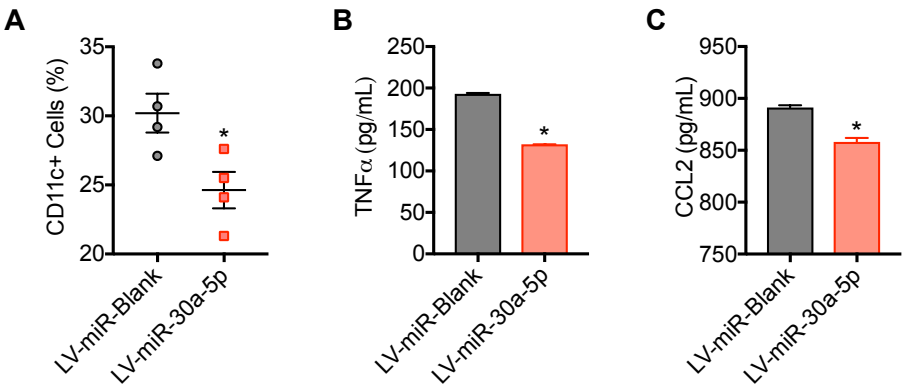

Figure 2.8 Lentiviral overexpression of miR-30a-5p in RAW264.7 macrophages reduces inflammation.
RAW264.7 macrophages were transduced with control lentivirus (LV-miR-Blank) or miR-30a-5p lentivirus (LV-miR-30a-5p), then M1 macrophage phenotype was assessed. (**A**) Flow cytometry percentage of CD11c+ cells. (**B**) TNFα concentration in cellular supernatant measured by ELISA. (**C**) CCL2 concentration in cellular supernatant measured by ELISA. *p<0.05

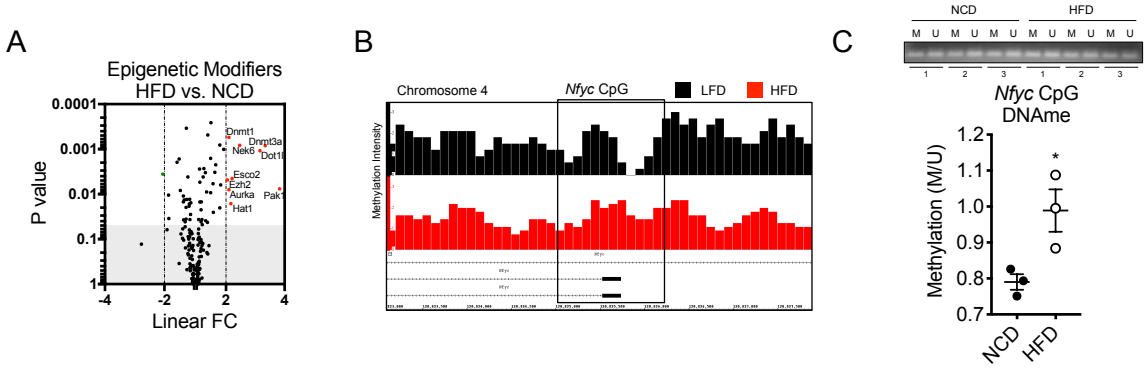

Figure 2.9 DNA Methylation-Dependent Regulation of miR-30.
As shown in Figure 2.1, F4/80+ ATMs were isolated from epididymal fat of 22-week-old HFD-induced obese and lean mice. Gene expression and DNA methylation were evaluated in ATMs. (**A**) Volcano plot displaying linear FC of genes encoding epigenetic modification enzymes and factors. Fold change and p value observations were extracted from transcriptome microarrays (See Figure 2.1 and Figure 2.2). (**B**) IGB visualization of meDIP-seq peak intensity of DNA methylation in the Nfyc promoter CpG island. (**C**) Methylation-specific PCR quantification of DNA methylation (DNAme) in the Nfyc promoter CpG island. For (A and C), values presented are representative of 3 independent experiments with 20 pooled NCD mice and 10 pooled HFD mice per experiment. For (B), data are representative of one experiment of 60 pooled LFD and 30 pooled HFD mice. Statistical differences were determined by using Student's t-test. *p<0.05, **p<0.01, ***p<0.001.

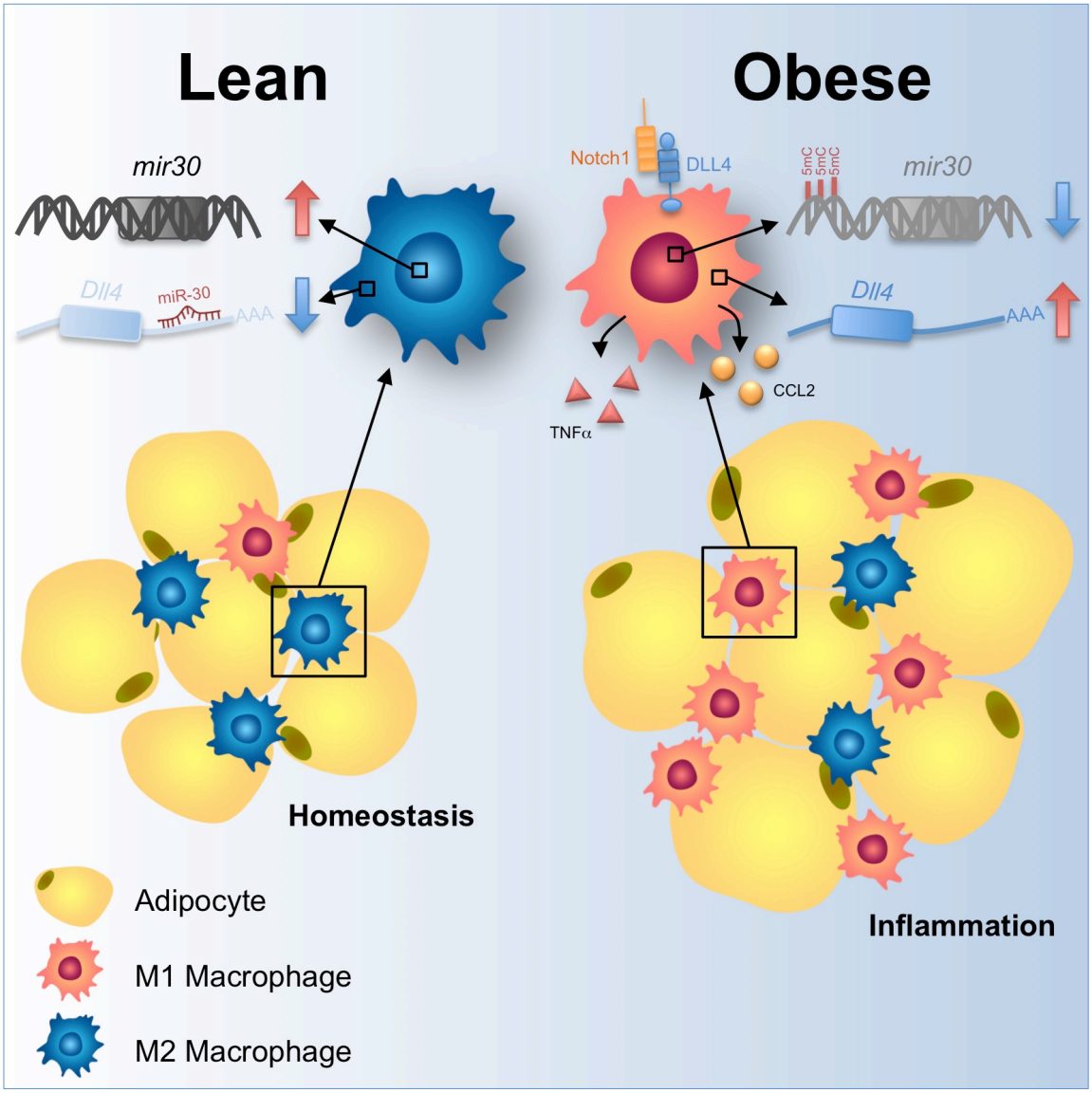

Figure 2.10 Illustrative summary.
At steady state, lean ATMs express elevated miR-30, which inhibits Delta-like-4 (DLL4) and Notch signaling-induced inflammation. Obesity promotes inflammation and M1 ATM polarization. DNA hypermethylation of mir30 downregulates miR-30 expression in obese ATMs, which leads to upregulation of DLL4, Notch signaling activation, and pro-inflammatory cytokine production.

CHAPTER 3

CANNABINOID RECEPTOR 1 BLOCKADE ATTENUATES OBESITY AND ADIPOSE TISSUE TYPE 1 INFLAMMATION THROUGH MIR-30E-5P REGULATION OF DELTA-LIKE-4 IN MACROPHAGES AND CONSEQUENTLY DOWNREGULATION OF TH1 CELLS[2]

[2] Miranda, K., P. Mehrpouya-Bahrami, P.S. Nagarkatti, and M. Nagarkatti. (2019) "Cannabinoid receptor 1 blockade attenuates obesity and adipose tissue type 1 inflammation through miR-30e-5p regulation of Delta-like-4 in macrophages and consequently downregulation of Th1 cells." *Frontiers in Immunology*. 10:1049.
Reprinted here with permission of publisher.

3.1 ABSTRACT

Obesity is characterized by chronic low-grade inflammation that contributes to development of cardiometabolic disorders. Cannabinoid receptor 1 (CB1) antagonists attenuate diet-induced obesity (DIO) and related inflammation, although the precise anti-inflammatory mechanisms involved have not been fully explored. In the current study we used a mouse model of DIO intervention to determine the microRNA (miRNA, miR)-mediated anti-obesity and anti-inflammatory effects of the CB1 antagonist, AM251. DIO mice that were fed high-fat diet (HFD) for 12 weeks were treated with AM251 (10mg/kg) for an additional four weeks. HFD+AM251 mice experienced rapid and prolonged weight loss and reduced inflammatory M1 adipose tissue macrophage (ATM) infiltration. To investigate miRNA-mediated regulation of ATMs, F4/80+ cells from stromal vascular fractions of epididymal fat were subjected to miR microarray analysis. Several miRs were differentially expressed in AM251-treated mice that were independent of calorie restriction. Prominently, miR-30e-5p was upregulated in ATMs from HFD+AM251 mice while the miR-30e-5p target, DLL4, was downregulated. Consistent with a decrease in DLL4-Notch signaling, fat storage and pro-inflammatory cytokine/chemokine expression was reduced following AM251 treatment. Furthermore, we found that AM251-treated macrophages can suppress DLL4-mediated Th1 polarization in CD4+ T cells. Together these data demonstrate that blocking CB1 receptors leads to upregulation of miR-30e-5p and down regulation of DLL4 in ATMs, which in turn suppress DLL4-Notch signaling-induced polarization of inflammatory Th1 cells

and adipocyte energy storage. This combined effect of ATMs and T cells leads to an anti-inflammatory state and attenuation of diet-induced obesity. These data support therapeutic potential of miR-30 in the treatment of cardiometabolic disorders.

3.2 Introduction

Obesity is a chief contributor to the global health burden as the World Health Organization estimates nearly forty percent of the population is overweight or obese. Obesity presents a risk to development of comorbid disorders such as type II diabetes, cardiovascular disease, and cancer (Haslam and James 2005; Kerr, Anderson, and Lippman 2017). Causes of obesity can be environmental— such as diet composition, overconsumption, and physical inactivity; or genetic— such as having a genetic mutation in the genes encoding the satiety hormone leptin or its receptor (Haslam and James 2005; MacReady 2014). All things considered, environmental factors involving poor diets, such as high-fat diets, are a driving force in the ongoing expansion of the disease.

Therapeutic strategies employed to combat diet-induced obesity (DIO) include lifestyle modifications and pharmacological interventions. While lifestyle changes would be most effective to curtail the obesity pandemic, such changes can be difficult to attain and/or maintain and combinations with pharmacological therapy have been shown to improve health outcomes (Yanovski and Yanovski 2014). Notably, the endocannabinoid (eCB) system is a major target for pharmacological therapy as its over activation is associated with obesity. The

eCB system is comprised of cannabinoid receptors type 1 and 2 (CB1 and CB2) and their endogenous ligands called “endocannabinoids”. CB1 expression is highly concentrated in the central nervous system and to a lesser extent in peripheral metabolic tissues, as well as, immune cells. Thus, CB1 is highly involved in appetite and metabolic regulation. Nearly two decades ago, it was discovered that activation of CB1 increases appetite and could promote development of obesity (Di Marzo et al. 2001). Thus, CB1 knockout mice were found to be resistant to development of DIO (C. Ravinet Trillou et al. 2004, 1). This led to the use of SR141716A (aka Rimonabant), a CB1 antagonist that reduces food intake, to treat DIO (Rinaldi-Carmona et al. 1994; Jbilo et al. 2005, 1; Christine Ravinet Trillou et al. 2003, 1). Unfortunately, adverse neuropsychiatric side effects caused this drug to fail to gain US Food and Drug Administration approval (Sam, Salem, and Ghatei 2011). However, research into unveiling the mechanisms by which CB1 blockade attenuates obesity has continued in the hopes of identifying additional target pathways for obesity treatment.

Another opportunity for attenuating obesity is targeting inflammation. Obesity is well characterized as having a state of chronic low-grade inflammation (Haiyan Xu et al. 2003). Increased adiposity initiates a switch from anti-inflammatory pro-insulin sensitive type 2 immune surveillance, to pro-inflammatory type 1 metabolic inflammation, which promotes metabolic dysfunction (Haiyan Xu et al. 2003). In adipose tissue, excess fat storage and adipocyte death leads to recruitment, polarization, and proliferation of pro-

inflammatory M1 adipose tissue macrophages (ATMs), which secrete cytokines such as TNFα, IL-6, CCL2, and IL-1β that decrease adipocyte insulin sensitivity and promote tissue damage (Amano et al. 2014; Boutens and Stienstra 2016). Additionally, M1 ATMs can act as antigen presenting cells to stimulate adaptive immune responses such as Th1 polarization and interferon gamma (IFNγ) production in CD4+ T cells, which further impairs insulin sensitivity (Morris et al. 2013; Winer et al. 2009). Pro-inflammatory ATMs dominate obese adipose tissue and therefore therapeutic strategies that reduce or skew ATMs from M1 to anti-inflammatory M2 phenotypes have been reported to improve tissue homeostasis and metabolism (Darkhal et al. 2015; Zheng et al. 2015). Interestingly, work done by our group has shown that treatment of DIO mice with the CB1 antagonist SR141716A reverses obesity and is associated with a decrease in ATM-dependent inflammation in epididymal fat of high-fat diet (HFD)-induced obese mice (Mehrpouya-Bahrami et al. 2017).

Macrophages are heterogeneous myeloid-derived innate immune cells that are capable of polarizing between a broad spectrum of pro- (M1) and anti- (M2) inflammatory phenotypes. Dynamic switching of their polarization state and gene expression can be achieved through microRNA (miRNA, miR)- mediated regulation (Zhang et al. 2013). miRNAs are short, non-coding RNAs that repress mRNA translation through complementary binding of a seed sequence with the 3' untranslated region (3'UTR) of target mRNAs (Bartel 2004). Recently, we characterized dysregulated miRNAs in ATMs during DIO, which indicated miRNA expression in ATMs modulates their inflammatory phenotype (Miranda et al.

2018). Importantly, miRNA-based therapeutics are currently being developed and tested for treatment of a variety of disorders including cardiovascular and metabolic diseases (Chakraborty et al. 2017). Thus, identification of miRNA involved in DIO, may help develop miRNA-based treatment modalities.

Notch signaling is an evolutionarily conserved signaling pathway that is involved in cellular development and cell-cell communication. It regulates a variety of cellular processes such as proliferation, differentiation, survival, and inflammation (Guruharsha, Kankel, and Artavanis-Tsakonas 2012). The Notch ligand Delta-like 4 (DLL4) contributes to many cardiometabolic disease mechanisms. In macrophages, DLL4 expression can be induced by M1-promoting stimuli such as the toll-like receptor 4 (TLR4) ligands lipopolysaccharide (LPS), IL-1β, and minimally modified low-density lipoprotein (Nakano et al. 2016). Macrophage DLL4-Notch signaling promotes a feed-forward loop of inflammatory polarization through nuclear factor κB and interferon regulatory factor 8 transcriptional pathways leading to production of pro-inflammatory cytokines such as TNFα and CCL2 (Nakano et al. 2016; Haixia Xu et al. 2012, 8). Additionally DLL4+ macrophages can signal through Notch1 on other cell types such as adipocytes and CD4+ T cells to promote excess energy storage and Th1 polarization, respectively (Morris et al. 2013; Bi et al. 2014; Skokos and Nussenzweig 2007; Amsen et al. 2004). Thus targeting the DLL4-Notch1 signaling pathway would be highly beneficial in treatment of cardiometabolic disorders. DLL4 blockade has been shown to improve atherosclerosis and metabolic disease while Notch1 blockade promotes

browning of white adipose tissue and improves energy expenditure and metabolism (Fukuda et al. 2012; Bi et al. 2014). Interestingly, miRNAs that target DLL4 have also been identified and include the miR-30 family (Bridge et al. 2012, 4; Shan et al. 2016, 4).

In the current study, we used a mouse model of DIO intervention to characterize miRNAs regulated by CB1 blockade in ATMs. DIO mice were treated with the high affinity CB1 antagonist AM251. We found several miRNAs to be differentially expressed following AM251 treatment that were independent of food restriction. Notably, miR-30e-5p was induced following AM251 treatment in DIO mice and was accompanied by a decrease in pro-inflammatory gene expression and reduced plasma IFNγ concentration. CB1 blockade in macrophages also suppressed Dll4-mediated Th1 polarization in lymphocytes. Our findings support a role for CB1 in regulation of miRNAs that dampen ATM inflammation and improve metabolism, which suggests that manipulation of miRNA in ATMs could be used to treat DIO and other inflammatory disorders.

3.3 Materials and Methods

Mice

Sixteen-week-old C57Bl/6J DIO (JAX Stock # 380050 & 380056) mice were obtained from The Jackson Laboratory and maintained on purified diets of either HFD (60% kcal from fat, D12492, Research Diets) or LFD (10% kcal fat, D12450J, Research Diets). Mice were housed in an AAALAC-accredited, specific-pathogen-free facility at the University of South Carolina School of

Medicine. After two weeks acclimation and 12-weeks of diet feeding, mice were treated with 10mg/kg AM251 (1117, Tocris) or Vehicle by oral gavage daily for 4 weeks. At the conclusion of the study, mice were euthanized by overdose isoflurane inhalation. All experiments were performed according to protocols approved by the University of South Carolina Institutional Animal Care and Use Committee.

Analytical procedures

Body composition was determined by dual-energy x-ray absorptiometry (DEXA) in isoflurane-anaesthetized mice. Body weight measurements were determined using an electronic gram scale with precision ± 0.1g. Blood glucose concentration was determined in 5h fasted mice by applying approximately 5uL tail-tip blood to a glucose test strip in a glucometer (Contour Next, Bayer). Fasting plasma insulin concentration was determined by ELISA kit according to manufacturer protocol including a standard curve (ThermoFisher Scientific). The homeostatic model assessment of insulin resistance (HOMA-IR) index was calculated by the equation (Fasting glucose x fasting insulin / 405) (Matthews et al. 1985).

Adipose tissue dissociation

Stromal vascular fractions (SVF) of epididymal fat were isolated by collagenase digestion as previously detailed (Miranda et al. 2018). In brief, minced adipose tissue was placed in Hank's Balanced Salt Solution containing 2% bovine serum albumin (BSA) and 1mg/mL collagenase then homogenized with a gentleMACs dissociator (Miltenyi Biotec), and incubated for 30-40 minutes

at 37°C with gentle shaking until fully dissociated. SVF cells were pelleted and floating adipocytes removed. SVFs were filtered, RBC-lysed, and washed, then used immediately for either flow cytometry or ATM isolation. To isolate ATMs, SVF cells were labeled with either Fluorescein isothiocyanate (FITC)- or Phycoerythrin (PE)-anti-F4/80 antibody (Clone: BM8, Biolegend) then F4/80+ ATMs were immunomagnetically selected with either FITC- or PE-Positive Selection Kit (StemCell Tech). Flow cytometry was used to evaluate selection purity, which was routinely >75%.

Flow cytometry

SVF cells or co-cultured cells were washed in staining buffer consisting of phosphate buffered saline (PBS), 2% heat-inactivated fetal bovine serum (FBS), and 1mM EDTA. Blocking of Fc receptors was performed by incubation with TruStain FcX (BioLegend) for 10m. Next, cells were incubated with appropriate fluorochrome-conjugated antibodies for 30m on ice (CD45-APC/Cy7, clone: 30-F11; CD11b-AlexaFluor700, clone: M1/70; F4/80-BV421, clone BM8; T-bet-BV605, clone 4B10, CD4-APC-Cy7, clone GK1.5). Cells were washed 3X in staining buffer then analyzed on a BD FACSCelesta flow cytometer. Data was analyzed with FlowJo v10 software.

RNA purification, cDNA synthesis, and qRT-PCR

ATMs were lysed in Qiazol and total RNA was purified with Qiagen miRNeasy Micro/Mini kit. RNA concentration and purity was measured using a NanoDrop 2000 spectrophotometer or Agilent Bioanalyzer. RNA was reverse transcribed to cDNA with the miScript II RT kit (Qiagen). Quantitative RT-PCR

was performed with miScript SYBR Green PCR kit (Qiagen) or SSO Advanced Universal SYBR Green (BioRad). MiScript miRNA Primer Assays (Qiagen) were used for miRNA qRT-PCR. Genes were amplified with the following primers purchased from Integrated DNA Technologies— Beta-Actin: Fwd-GGC TGT ATT CCC CTC CAT CG, Rev-CCA GTT GGT AAC AAT GCC ATG T; Tnfa: Fwd-CTG AAC TTC GGG GTG ATC GG, Rev-GGC TTG TCA CTC GAA TTT TGA GA; IL6: Fwd-CCA AGA GGT GAG TGC TTC CC, Rev-CTG TTG TTC AGA CTC TCT CCC T; Ccl2: Fwd-TTA AAA ACC TGG ATC GGA ACC AA, Rev-GCA TTA GCT TCA GAT TTA CGG GT; Ccl3: Fwd-TTC TCT GTA CCA TGA CAC TCT GC, Rev-CGT GGA ATC TTC CGG CTG TAG. Fold change in expression was determined by the comparative cycle method ($2^{-\Delta\Delta Ct}$).

MicroRNA microarrays and analysis

ATM RNA was prepared for microRNA microarrays and microarrays performed as previously described (Mehrpouya-Bahrami et al., in review). Probe signal values were used to determine linear fold change between pairwise comparisons. Log2 fold change values were then calculated. MiRNAs were considered differentially expressed between groups if the Log2 fold change was at least ±2. Mean normalized expression (MNE) was calculated for each of the dysregulated miRs and a heatmap displaying MNE was made with GraphPad Prism Version 7.000 (GraphPad Software).

Immunofluorescence and histology

Epididymal fat pads were fixed in 4% paraformaldehyde and embedded in paraffin. Five μm tissue sections were cut, deparaffinized, and rehydrated then

incubated in blocking buffer consisting of 1X PBS and 1% (w/v) BSA for 30m. Tissues were then incubated with 1ug TruStain FcX (Clone: 93, BioLegend) for 10m followed by primary antibodies (F4/80-AlexaFluor488, clone: BM8, [1:100], BioLegend; DLL4-unconjugated, clone: HMD4-1, [1:100] BioLegend) for 30m at room temperature. DLL4 signal was amplified with Biotin Goat-anti-Armenian Hamster IgG, (Clone: Poly4055, [1:500], BioLegend) followed by Streptavidin-DyLight 633 [1:1000], Invitrogen 21844). Tissues were counterstained with 40uM Hoechst 33342 (Molecular Probes H21492), and 2ug Phalloidin-tetramethylrhodamine (Sigma P1951), then mounted with ProLong Diamond Anti-fade Mountant (ThermoFisher P36965). Hematoxylin and eosin (H&E) staining of epididymal adipose tissue sections was performed by the University of South Carolina Intrumentation Resource Facility under standard protocols. Adipocyte size was quantified using the Adiposoft plugin in FIJI (FIJI is Just ImageJ, NIH) (Galarraga et al. 2012).

Confocal imaging and analysis

Confocal microscopy and analysis were performed as previously described (Miranda et al. 2018). In brief, confocal images of sectioned epididymal adipose tissue were taken on a Zeiss LSM 510 Meta Confocal Scanning Laser Microscope. Five images per sample were acquired using a 40X water immersion objective. Original LSM data files were imported into Fiji (Fiji Is Just ImageJ, NIH) then split into channels. Thresholds were applied to the Cy5 channel using Fiji's max Entropy algorithm to identify regions of interest (ROI)

that express DLL4. Then, area was measured for each ROI. Each biological replicate is the mean expression of 5 images.

Macrophage: lymphocyte co-culture

Bone marrow derived macrophages (BMDM) were generated by isolating bone marrow cells from the tibia and femur of 6-8 week old naïve female C57Bl6/J mice and culturing in complete DMEM/F12 medium supplemented with 10% heat-inactivated FBS, 1% penicillin/streptomycin, 2mM L-glutamine, and 1U/mL macrophage-colony stimulating factor (M-CSF, Biolegend 576406) for 7 days as previously described (Miranda et al. 2018). Lymphocytes from mesenteric, inguinal, axillary, and cervical lymph nodes were isolated from naïve 6-8 week old female C57Bl6/J mice as previously described (Becker, Nagarkatti, and Nagarkatti 2018). Day 7 BMDM were re-plated in complete RPMI 1640 medium supplemented with 10% heat-inactivated FBS, 1% penicillin/streptomycin, 2mM L-glutamine, 10mM HEPES buffer, and 0.0002% β-mercaptoethanol. Next the BMDM were pretreated with AM251 (10uM), α-DLL4 blocking mAb (1ug/mL), AM251 (10uM) + α-DLL4 (1ug/mL), or appropriate vehicle and isotype controls for 1 hr. Then, polarization factors were added to the medium. For polarization to M1, 100ng/mL LPS + 50ng/mL IFNγ was added (eBioscience 00-4976 and BioLegend 575302). For M2, 10ng/mL IL-4 was added (BioLegend 574302). The cells were cultured for 24hr then BMDM supernatant was collected and the BMDM were washed, counted, and co-cultured at ratios 1:1 or 1:3 (BMDM:lymphocyte) with naïve lymphocytes. $1x10^5$ macrophages were cultured with either $1x10^5$ lymphocytes (1:1) or $3x10^5$

lymphocytes (1:3). ConcanavalinA (ConA, Sigma C5275) was added to the culture at a dose of 1ug/mL to induce Th1 cell polarization. After 48hr of co-culture, the cells were collected for flow cytometry and supernatants were isolated for IFNγ ELISA (BioLegend 430801). BMDM supernatants were used for TNFα ELISA to confirm M1 polarization.

Statistical analysis

Statistical analyses were performed using GraphPad Prism Version 7.000 for Mac (GraphPad Software). Values are expressed as mean ± standard error. One-way ANOVA was used for multiple group analyses. Two-way ANOVA was used for significance across time points. The null hypothesis was rejected if $p<0.05$.

3.4 RESULTS

CB1 blockade with AM251 reverses DIO

To study the anti-obesity and anti-inflammatory effects of weight loss due to CB1 blockade, we used a well-established DIO intervention model whereby 6-week-old mice were fed HFD or control LFD for 12 weeks to induce an obese or lean phenotype, respectively. Following 12 weeks of purified diet feeding, baseline body composition was measured by DEXA and HFD-fed mice were stratified into experimental groups with equivalent mean fat mass. The mice were then treated with the CB1 antagonist AM251 at a dose of 10mg/kg or Vehicle (Veh, 0.1% Tween80) for 4-weeks by daily oral gavage while continuing purified diet (Figure 3.1A). The experimental groups included: ad libitium fed LFD+Veh

(lean reference), ad libitum fed HFD+Veh, ad libitum fed HFD+AM251, and a Vehicle-treated HFD group that was pair-fed to the HFD+AM251 group (called "HFD-Pair-fed").

During the study, LFD+Veh mice maintained their initial body weight and HFD+Veh mice gained 15% of their baseline weight (Figure 3.1B). In contrast, HFD+AM251 mice experienced rapid and sustained weight loss during the 4-week DIO intervention model (Figure 3.1B). Acute weight loss was observed during the first week, which coincided with intense suppression of appetite (Figures 3.1B and 3.1C). For the remainder of the study, AM251-treated mice experienced persistent weight loss of approximately 20% their starting weight despite an increase in appetite (Figure 3.1B). Furthermore, appetite-independent weight loss was observed in HFD+AM251 mice as the HFD-Pair-fed group lost significantly less weight than the AM251-treated mice (Figure 3.1B). At the end of the study, the HFD-Pair-fed group was ~94% of it's baseline weight. Body weight changes were consistent with alterations in adiposity and not lean mass (Figure 3.1C). DEXA scans showed that fat mass was increased in HFD+Veh mice, decreased in HFD+AM251 mice, and unchanged in LFD+Veh and HFD-Pair-fed mice when compared to baseline measures (Figure 3.1C).

Glucose intolerance and decreased insulin sensitivity are hallmarks of the obese state. To evaluate AM251-dependent effects on glucose metabolism; fasting glucose, fasting insulin, and a homeostatic model assessment of insulin resistance index (HOMA-IR) were determined. HFD+AM251 mice did not experience an increase in fasting glucose over the duration of the 4-week

intervention, whereas HFD+Veh and HFD-Pair-fed experienced significant increases in fasting glucose (Figure 3.1D). AM251-treatment in HFD-fed mice also led to decreases in fasting insulin and HOMA-IR measurements that were similar to LFD+Veh mice (Figures 3.1E-3.1F). Although, these decreases may be primarily an effect of decreased appetite as HFD+AM251 measures were similar to those in HFD-Pair-fed mice (Figures 3.1E-3.1F).

AM251 treatment in DIO mice reduces adipose tissue macrophage accumulation

A chief characteristic of obesity is adipose tissue inflammation, which can lead to metabolic dysfunction. ATMs are the key initiators and instigators of this inflammation as they typically dominate obese adipose tissue through monocyte recruitment and local proliferation (Amano et al. 2014; Boutens and Stienstra 2016). To determine macrophage burden in adipose tissue, stromal vascular fractions (SVF) of epididymal fat were isolated after the 4-week intervention and subjected to flow cytometry analysis (Figure 3.2A). The percentages and total cell numbers of CD45+CD11b+F4/80+ ATMs and CD45+CD11b+F4/80+CD11c+ M1 ATMs in SVFs were elevated in HFD+Veh mice vs. LFD+Veh mice, and reduced in HFD+AM251 mice vs. HFD+Veh and HFD-Pair-fed (Figures 3.2A, 3.2C, 3.2E). Epididymal fat pad mass was also reduced in AM251-treated mice (Figure 3.2B). To account for alterations in fat mass, ATM number per gram of adipose tissue was calculated and likewise AM251 treatment led to a reduction in ATM number that was significant when compared to HFD+Veh group and trended less than HFD-Pair-fed group (Figures 3.2D and 3.2F).

AM251 intervention modulates miRNA expression in ATMs

Next we determined if AM251-intervention alters miRNA expression in ATMs as we have previously shown that miRNA dysregulation is observed in ATMs from obese mice and contributes to their inflammatory state (Miranda et al. 2018). To perform this, F4/80+ ATMs were isolated from epididymal fat and used for miRNA microarray analysis. Of approximately 3000 miRs tested, 41 and 25 were found to be up- and down-regulated, respectively in HFD+AM251 vs. HFD+Veh. Additionally, 123 and 42 were up- and down-regulated, respectively in HFD+AM251 vs. HFD-Pair-fed. Also, 196 were up- and 70 were down-regulated in LFD+Veh vs. HFD+Veh.

To distinguish differentially expressed miRs in HFD+AM251 ATMs that were independent of appetite restriction, we identified miRs that were similarly dysregulated in HFD+AM251 vs. HFD+Veh and in HFD+AM251 vs. HFD-Pair-fed. This analysis led to identification of 35 miRNAs that were differentially expressed due to appetite-independent AM251 treatment. Of these 35 miRNAs, 24 were up-regulated and 11 were down-regulated (Figure 3.3A and Table 3.1). A core analysis of these miRs with Qiagen Ingenuity Pathway Analysis (IPA, Qiagen) revealed significant overlap ($p<0.05$) with processes such as cancer, inflammatory response, metabolic disease, and hepatitis (Figures 3.4A and 3.4B). Furthermore, the top affected networks involved carbohydrate metabolism and cell cycle (Figures 3.4C and 3.4D). Interestingly, miR-30e-5p expression was found to be elevated in HFD+AM251 (Figure 3.3A), which as per the IPA analysis was associated with DLL4-Notch signaling-induced inflammation (Figure 3.3B).

In addition, miR-30 was found to target the Dll4 3'UTR which was conserved among humans and mice (Figure 3.3C).

AM251 treatment leads to induction of miR-30e-5p and reduces DLL4

Next, we validated expression of miR-30e-5p in F4/80+ ATMs by qRT-PCR (Figure 3.3D). Consequently, we evaluated protein expression of the miR-30e-5p target DLL4 in adipose tissue by immunofluorescence (Figures 3.3E and 3.3F). DLL4 expression was significantly decreased in HFD+AM251 vs. HFD+Veh (Figures 3.3E and 3.3F).

CB1 blockade reduces energy storage and type 1 adipose tissue inflammation

Dll4-Notch1 signaling has been characterized to promote energy storage and type 1 inflammatory responses. Consistent with a decrease in DLL4, epididymal adipocyte size and fat mass was reduced following AM251 treatment (Figures 3.5A, 3.5B, 3.5B). We performed qRT-PCR of pro-inflammatory genes in ATMs, which revealed that Tnfa, Ccl2, IL6, and CCL3 expression are reduced following AM251 treatment in vivo (Figure 3.5C). In accordance with a decrease in M1 ATM activation and DLL4 expression, the Th1 response was reduced in HFD+AM251 vs. HFD+Veh-treated mice as evidenced by decreased levels of circulating IFNγ (Figure 3.5D).

AM251 reduces Th1 inflammation by regulating macrophage DLL4

To test the possibility that AM251-mediated suppression of DLL4 was causing reduced Th1 polarization, we pre-treated naïve BMDM with anti-DLL4 blocking antibody (α-DLL4), AM251, or AM251 + α-DLL4, then added polarization factors to the medium to promote M1 (LPS + IFNγ) or M2 (IL-4) phenotypes.

After 24hr of polarization, the BMDM supernatant was collected and used for TNFα ELISA to confirm M1 polarization (Figure 3.6A) Next, the BMDM were washed and co-cultured with naïve lymphocytes in the presence of the T-cell mitogen, ConA for 48hr. Culture of lymphocytes alone with ConA was able to induce a Th1 response as evidenced by elevated T-bet expression and IFNγ secretion (Figure 3.6B and 3.6C). The most Th1 polarization was observed in the M1-DMSO+IgG vehicle/Isotype control co-culture (Figures 3.7A-3.7C). Blocking DLL4 signaling (M1-DMSO+α-DLL4) caused reduced Th1 polarization (Figures 3.7A-3.7C). Similarly, CB1 blockade with AM251 reduced Th1 polarization to the same extent as blocking DLL4 alone (Figures 3.7A-3.7C). Blocking of both CB1 and DLL4 led to little change in Th1 polarization versus blocking of CB1 alone or DLL4 alone (Figures 3.7A-3.7C). As expected, lymphocyte IFNγ production was observed only in M1 co-cultures as M2 co-cultures served as a negative control (Figure 3.7B and 3.7C).

3.5 Discussion

ATMs are a dominant cell type in the adipose tissue of obese individuals and their production of inflammatory mediators contributes to metabolic dysfunction and progression towards development of cardiometabolic disorders. Therapies that decrease ATM-dependent inflammation are thought to have great potential for decreasing the incidence of obesity and complications (Red Eagle and Chawla 2010). In the current study, we identified miRNAs in ATMs that are

associated with decreased inflammation and weight-loss due to pharmacological intervention of DIO with the CB1 antagonist AM251.

The CB1 receptor is well known to modulate appetite and energy homeostasis. Blockade of CB1 activation attenuates obesity by affecting multiple areas including leptin signaling, white adipose tissue browning, gut microbiota interactions, and reducing inflammation (Di Marzo et al. 2001; C. Ravinet Trillou et al. 2004; Jbilo et al. 2005; Christine Ravinet Trillou et al. 2003; Mehrpouya-Bahrami et al. 2017; Azua et al. 2017). In this study and consistent with previous reports, we found that AM251 induces weight loss, improves glucose metabolism, and decreases adipose tissue inflammation.

To further understand regulation of ATM inflammation in this model, we investigated miRNAs by use of microarrays. MiRNAs are important regulators of gene expression because it is thought that approximately 60% of genes are conserved targets for miRNAs (Bartel 2004). Alterations in miRNA expression can also lead to quick changes in gene expression and use of miRNAs for therapeutic purposes holds high potential. We found that treatment of DIO mice with AM251 for 4-weeks led to various alterations of miRNA expression in ATMs from epididymal fat. Furthermore, use of a pair-fed control led to identification of several of miRs that were independent of AM251-induced appetite restriction. Therefore, we identified several miRNAs that may be involved in regulation of enhanced energy expenditure not due to calorie restriction. These miRNAs were also found to have overlap with several pathways relating to obesity-associated comorbid disorders including cancer, hematological disease, immunological

disease, and metabolic diseases. Together these data indicate miRNA-mediated regulation of ATMs contribute to attenuation of obesity by reducing adipose tissue inflammation, improving energy metabolism, and inducing weight-loss during DIO intervention with AM251.

Excitingly, we found that miR-30e-5p was reproducibly induced following AM251 treatment, which indicates an association between miR-30e-5p upregulation and appetite-independent weight loss. This miRNA has been previously characterized to target DLL4 and reduce DLL4-Notch signaling (Bridge et al. 2012; Shan et al. 2016). We have also previously demonstrated that the miR-30 family is downregulated in ATMs from obese vs. lean mice, while DLL4 expression is increased in ATMs from obese vs. lean mice, which indicates that miR-30e-5p attenuates inflammation in ATMs through regulation of the Notch signaling pathway (Miranda et al. 2018). Downregulation of miR-30 in macrophages also induced secretion of pro-inflammatory mediators TNFα and CCL2 (Miranda et al. 2018). Here our results support our previous findings and excitingly, induction of miR-30e-5p in HFD+AM251 ATMs indicates that miR-30e-5p may be used therapeutically to dampen ATM-mediated inflammation and reduce obesity. Consistent with increased miR-30e-5p expression, we found that DLL4 expression was reduced in adipose tissue from HFD+AM251 mice. It is possible that miR-30e-5p could have additional beneficial effects beyond targeting *Dll4*, however, we found several parameters to be reduced in AM251 treated mice that are consistent with a reduction in DLL4-Notch signaling. These include a reduction in adipocyte size and fat pad mass, which indicates reduction

in energy storage and an increase in energy expenditure, a reduction in ATM pro-inflammatory cytokine gene expression and M1 polarization, and a reduction in Th1 inflammation with reduced circulating IFNγ.

In addition, we demonstrated that blocking of CB1 receptors specifically on M1 macrophages could suppress their ability to promote a Th1 response in CD4+ T cells. This effect appears to be dependent on CB1-mediated regulation of DLL4 expression in macrophages as DLL4 is known to promote Th1 differentiation and we, in this study, showed that CB1 blockade reduces expression of this ligand (Skokos and Nussenzweig 2007). Thus, our data support a mechanism whereby CB1 blockade promotes induction of miR-30e-5p, which downregulates macrophage DLL4 and subsequent type 1 inflammatory responses including M1 macrophage and Th1 CD4+ T cell polarization, along with production of their inflammatory cytokines including TNFα, CCL2, and IFNγ (Figure 3.8).

Previous evidence advocates that miR-30 as well as DLL4 blockade may be therapeutically beneficial to reducing severity of metabolic disorders. MiRNA-30c mitigates hypercholesterolemia and atherosclerosis in mice by altering lipid metabolism (Irani et al. 2016; Soh et al. 2013). Additionally, miR-30b/c promotes thermogenesis and adipose tissue browning (Hu et al. 2015, 30). Moreover, miR-30 expression in ATMs is inversely correlated with obesity (Miranda et al. 2018). DLL4 blockade also protects against atherosclerosis (Fukuda et al. 2012). Blocking the DLL4 receptor Notch1 also attenuates obesity (Bi et al. 2014). Together, these data indicate that blocking of CB1 in ATMs may contribute to

improvement in obesity phenotype through miR-30e-5p regulation of DLL4. Therefore, future studies focusing on in vivo induction of macrophage-specific miR-30 in DIO and other cardiometabolic models could shed new light on the mechanistic potential of this miRNA family for treatment of these macrophage-driven chronic diseases.

Table 3.1 Dysregulated miRNAs and their experimental fold change observations in F4/80^{+} ATMs.

MicroRNA ID	Comparison (Log_2 fold change)		
	LFD+Veh vs. HFD+Veh	HFD+AM251 vs. HFD+Veh	HFD+AM251 vs. HFD-Pair-fed
mmu-miR-30e-5p	6.386	3.450	3.880
mmu-miR-346-5p	6.979	2.131	5.107
mmu-miR-28a-5p	3.288	2.652	4.274
mmu-miR-28a-3p	1.451	2.253	4.292
mmu-miR-425-3p	4.917	2.348	2.021
mmu-miR-671-5p	3.631	2.923	4.117
mmu-miR-668-5p	-1.409	3.236	2.456
mmu-miR-466f-3p	-1.112	2.674	22.225
mmu-miR-466i-3p	-2.023	4.668	3.614
mmu-miR-669e-3p	-1.026	2.142	2.390
mmu-miR-1894-5p	2.554	2.220	5.140
mmu-miR-1894-3p	4.814	4.405	4.637
mmu-miR-1946a	7.775	4.164	2.332
mmu-miR-3081-5p	1.690	3.287	2.353
mmu-miR-3102-5p.2-5p	4.134	3.661	5.222
mmu-miR-6340	-1.007	2.453	3.541
mmu-miR-6906-5p	-3.464	2.037	3.136
mmu-miR-7011-5p	2.712	2.793	3.109
mmu-miR-7040-5p	4.105	3.438	15.522
mmu-miR-7045-3p	1.856	17.438	4.285
mmu-miR-7048-5p	7.016	2.653	2.538
mmu-miR-7238-5p	2.811	4.674	5.337
mmu-mir-883b	1.243	3.196	3.699
mmu-mir-6414	-1.073	2.080	2.122
mmu-miR-99b-3p	1.082	-2.413	-3.258
mmu-miR-195a-3p	2.502	-4.601	-2.357
mmu-miR-34c-5p	5.540	-5.626	-23.750
mmu-miR-25-3p	-1.300	-2.325	-2.021
mmu-miR-676-3p	1.003	-2.051	-3.930
mmu-miR-5112	1.064	-2.500	-3.202
mmu-miR-5121	-1.968	-16.757	-4.637
mmu-miR-6937-5p	3.597	-2.075	-2.827
mmu-miR-6949-5p	-3.261	-4.095	-2.201
mmu-mir-466f-4	1.979	-2.734	-2.182
mmu-mir-5112	-1.837	-4.554	-2.165
Upregulated			
Downregulated			

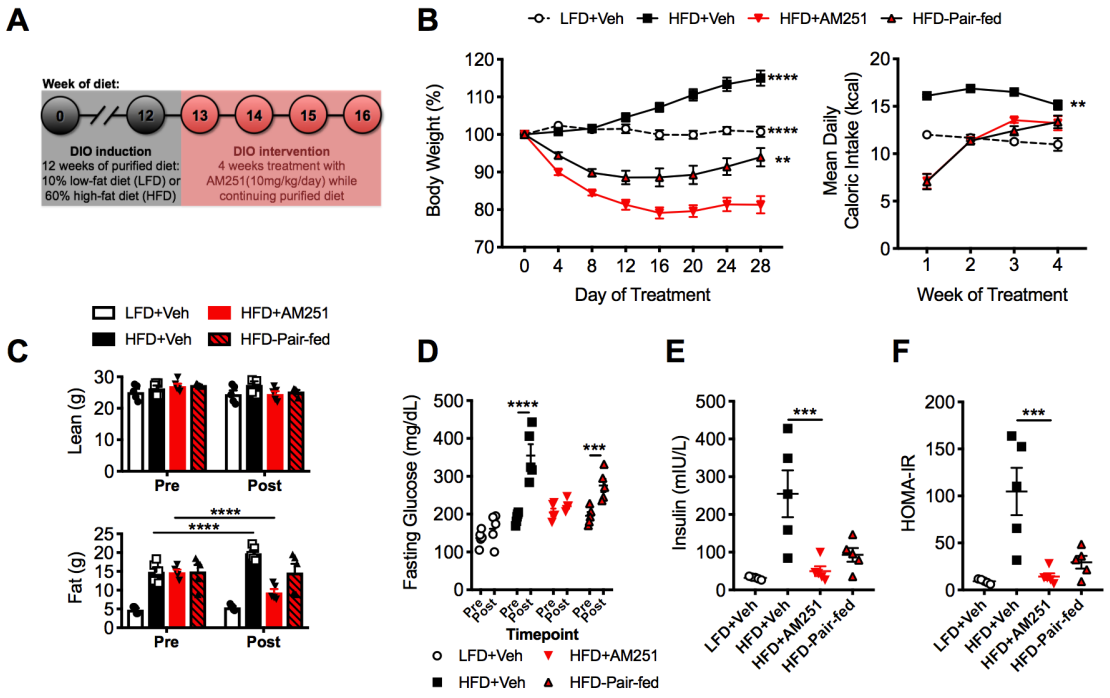

Figure 3.1 Treatment of mice with the CB1 antagonist (AM251) reverses obesity.

12-week HFD-fed obese mice were treated with the CB1 antagonist AM251 (10mg/kg) for 4 weeks to assess intervention of obesity parameters. (A) Experimental timeline. (B) Percentage body weight growth and energy intake during the 4-week intervention.(C) DEXA body composition Pre- and Post- 4 weeks of treatment. (D) 5hr fasting blood glucose Pre- and Post- 4 weeks of treatment. (E) 5hr fasting insulin after 4 weeks of treatment. (F) Insulin resistance index (HOMA-IR) after 4 weeks of treatment. Data are mean +/- SEM. N=5 mice/group. Significance vs. HFD+AM251 was determined by one-way ANOVA (B, E&F). Significance between time points was determined two-way ANOVA (C&D). ****P<0.0001, ***P<0.001, **P<0.01, *P<0.05.

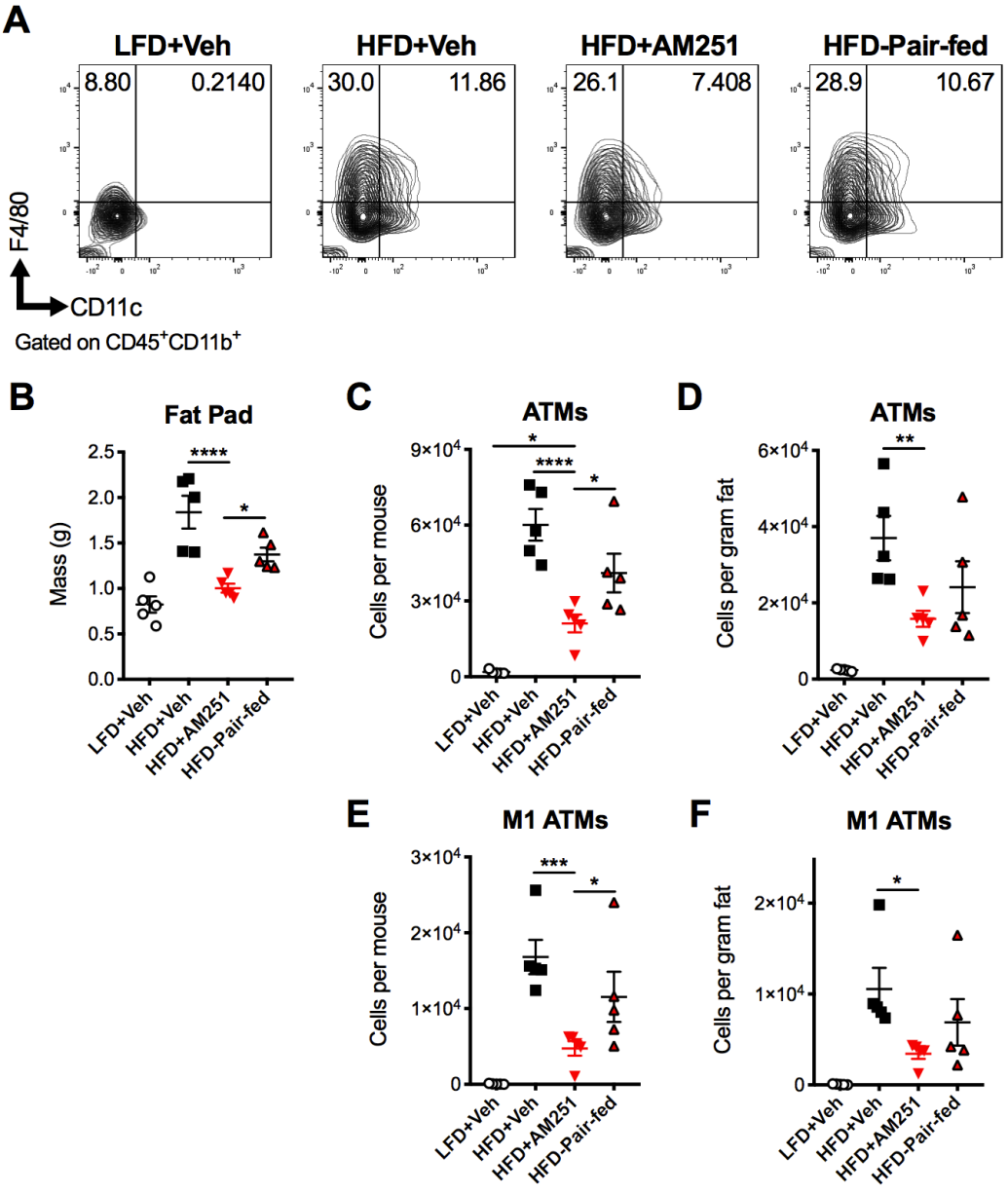

Figure 3.2 CB1 blockade reduces abundance of pro-inflammatory macrophages in epididymal fat.
HFD-fed obese mice were treated with the CB1 antagonist AM251 (10mg/kg) as described in Figure 3.1 legend. Epididymal fat SVFs from AM251-treated DIO mice were analyzed by flow cytometry. CD45+CD11b+F4/80+ cells are considered as "ATMs". CD45+CD11b+F4/80+CD11c+ cells are depicted as "M1 ATMs". (A) Contour plots of ATMs. (B) Epididymal fat mass. (C) Total epididymal fat ATMs per mouse.(D) ATMs per gram of fat. (E) Total epididymal fat M1 ATMs per mouse. (F) M1 ATMs per gram of fat. Data are mean +/- SEM. N=5 mice/group. Significance was determined by one-way ANOVA. ****P<0.0001, ***P<0.001, **P<0.01, *P<0.05.

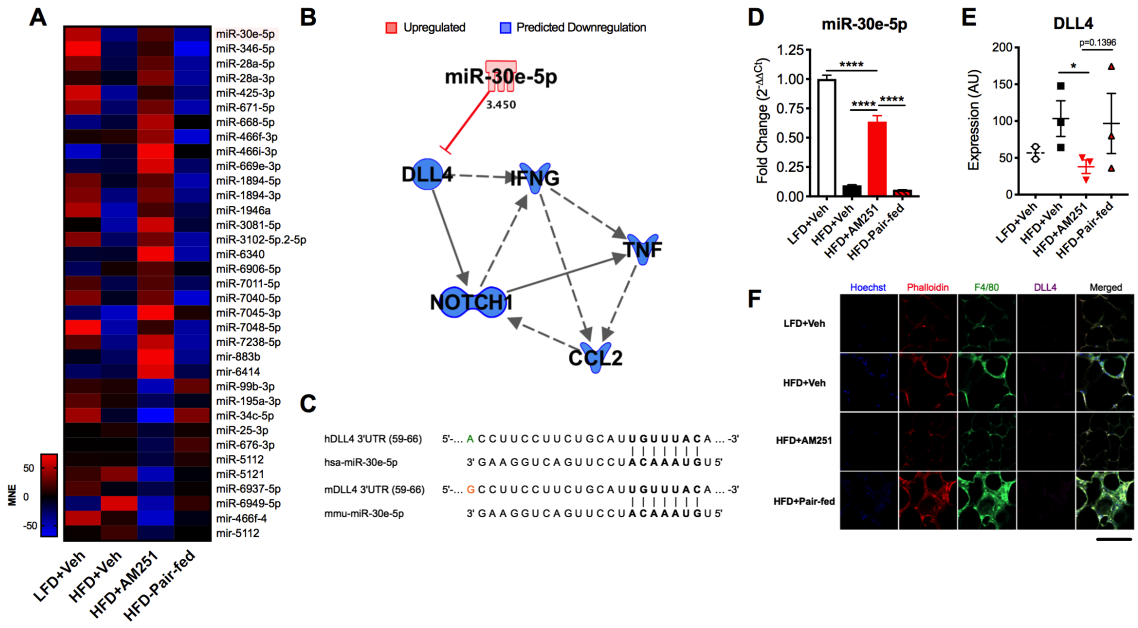

Figure 3.3 AM251 treatment elevates ATM miR-30e-5p and reduces target expression of the pro-inflammatory Notch ligand Delta-like-4.
DIO mice were treated with the CB1 antagonist AM251 (10mg/kg) as described in Figure 3.1 legend. MicroRNA microarrays were performed on F4/80+ ATMs isolated from epididymal fat after the 4-week AM251 intervention.(A) Heatmap of differentially expressed miRs in ATMs resulting from AM251 treatment, independent of effects of caloric restriction. (Log_2 fold change ≥±2) (B) Qiagen IPA network of miRs targeting the DLL4-Notch signaling pathway and downstream inflammatory cytokines. Expression values and predictions are overlaid on the network. (C) Sequence conservation of human and mouse miR-30e-5p binding to Dll4 3'UTR. (D) qRT-PCR of miR-30e-5p in ATMs. (E) Confocal microscopy quantitation of DLL4 expression in epididymal adipose tissue. (F) Representative confocal micrographs. Images are to equal scale. For A and D, data are presented from independent experiments of 4-10 pooled mice per group. For E, N=3 mice/group. Significance was determined by one-way ANOVA. ****P<0.0001, *P<0.05.

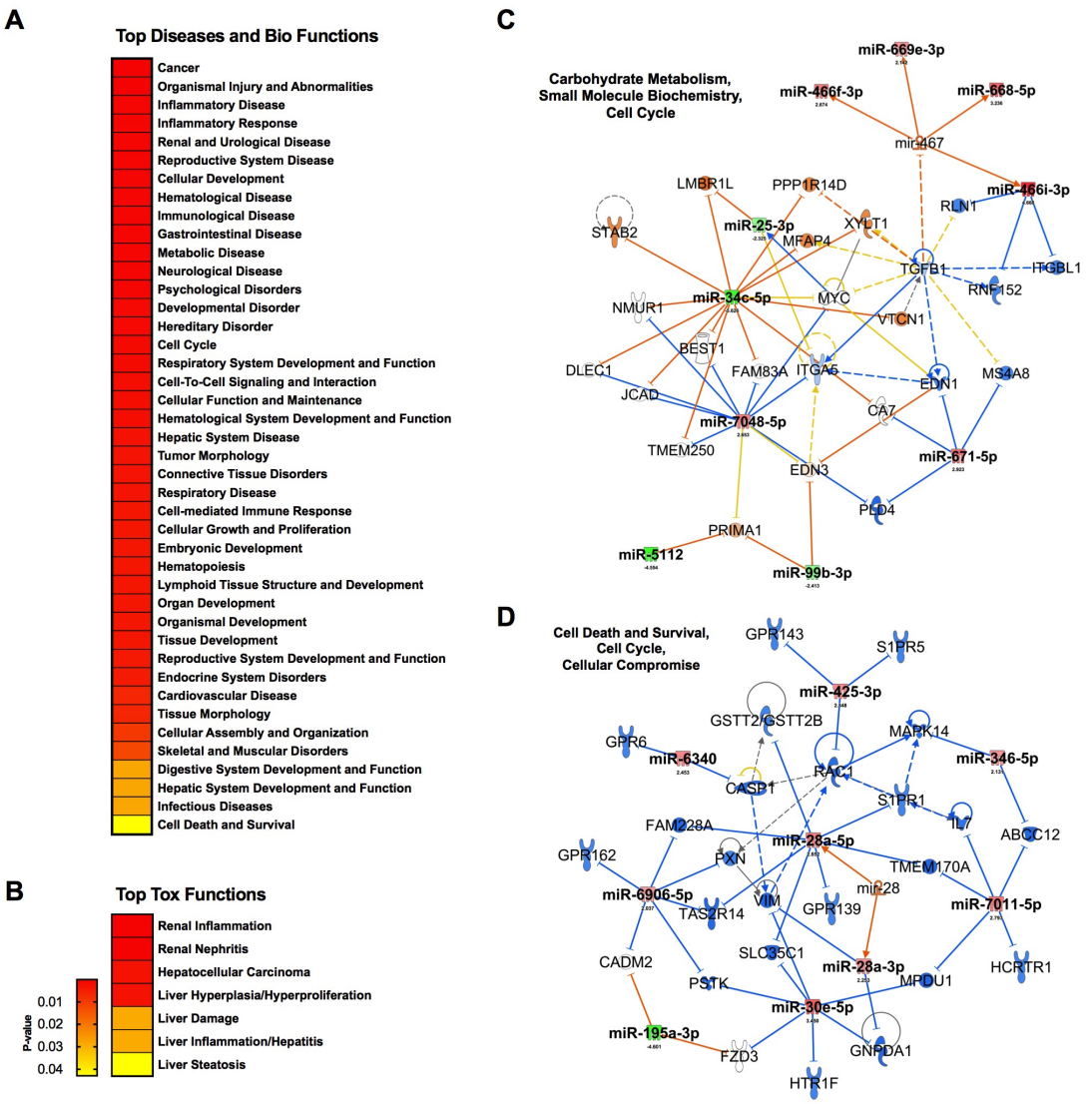

Figure 3.4 Pathway analysis of dysregulated miRNAs following AM251 treatment.

Qiagen IPA was used for core analysis of dysregulated miRNAs in ATMs. (A-B) Top Diseases, biological functions, and toxicological functions affected by the dysregulated miRs. (C-D) The top 2 affected networks. Network pathways are depicted with overlaid expression values and predictions. Red: upregulated, green: downregulated, orange: predicted upregulation, blue: predicted downregulation.

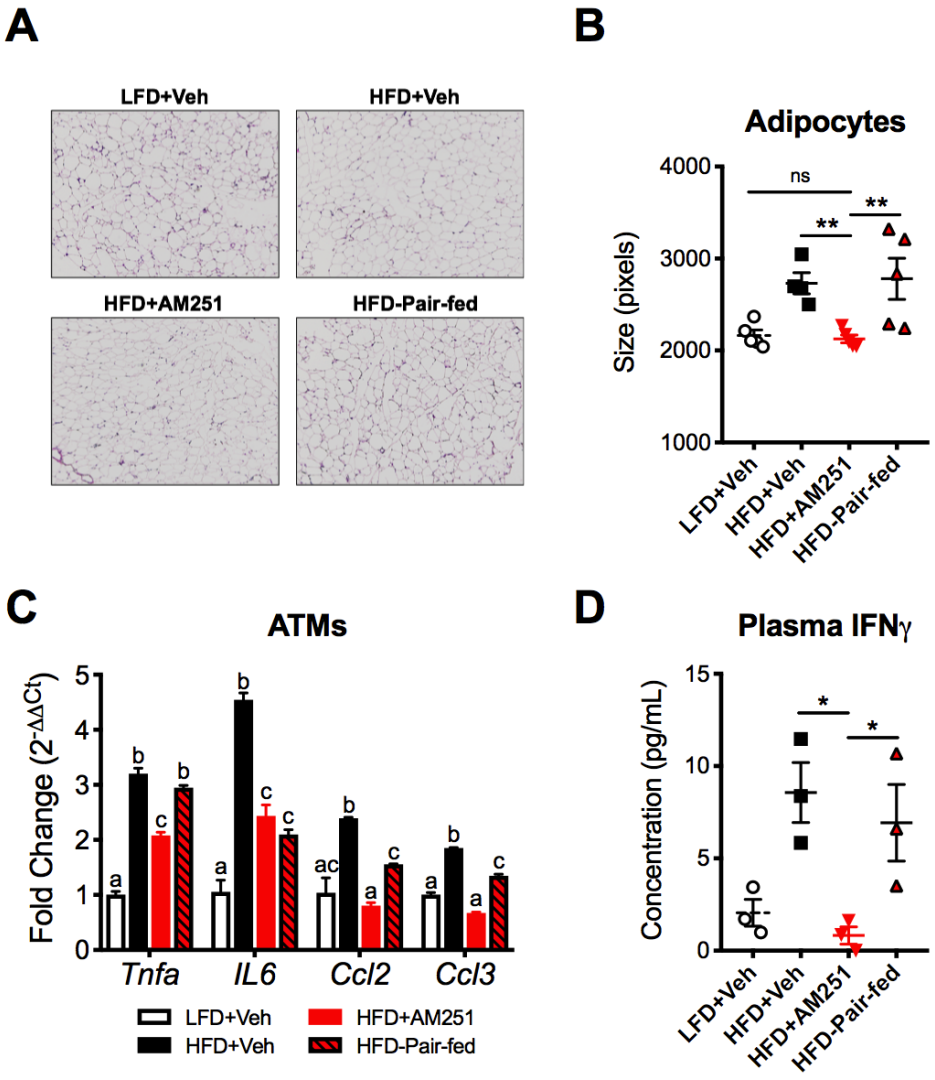

Figure 3.5 AM251 treatment in vivo reduces energy storage and type 1 inflammation associated with DLL4-Notch signaling.
HFD-fed obese mice were treated with AM251 (10mg/kg) for 4 weeks as described in Figure 3.1 legend. Adipocyte size, ATM gene expression, and plasma IFNγ were quantified in mice after the 4-week AM251 intervention. (A) Representative H&E stains of epididymal fat. Images are to equal scale (4X). (B) FIJI adipocyte size quantification. (C) qRT-PCR expression of inflammatory cytokine/chemokine genes in F4/80+ ATMs. (D) Plasma IFNγ concentration measured by ELISA. Data are mean +/- SEM. For A and B, N=4-5 mice/group. For C, data are presented from a single experiment of 4-10 pooled mice per group. For D, N=3 independent experiments of pooled plasma from 4-10 mice/group. Significance was determined by one-way ANOVA. **P<0.01, *P<0.05. For C, p<0.05 if alphabetical characters differ between groups.

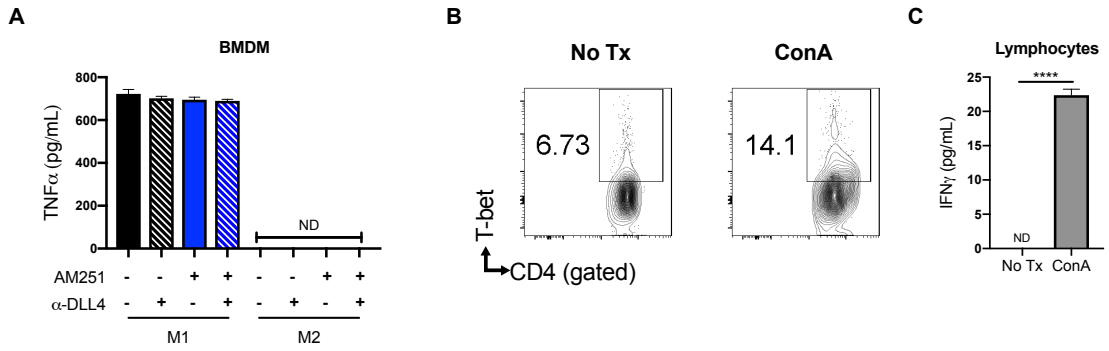

Figure 3.6 Confirmation of M1 polarization in BMDM and Th1 polarization in CD4+ T cells.

For (A), BMDM from naïve mice were pretreated with AM251 (10uM) +/- α-DLL4 blocking mAb (1ug/mL) or vehicle/isotype controls for 1h then polarized to M1 (LPS+IFNγ) or M2 (IL-4) for 24 hr. Supernatants were collected for TNFα ELISA to confirm M1 polarization. For (B-C), naïve lymphocytes were cultured in medium containing 1ug/mL ConA for 48 hr. (A) TNFα concentration detected in BMDM supernatant by ELISA. (B) Flow cytometry of CD4+T-bet+ Th1 lymphocytes. (C) IFNγ concentration detected in lymphocyte supernatant by ELISA. ****p<0.0001 by unpaired two-tailed T-test. ND: not detected.

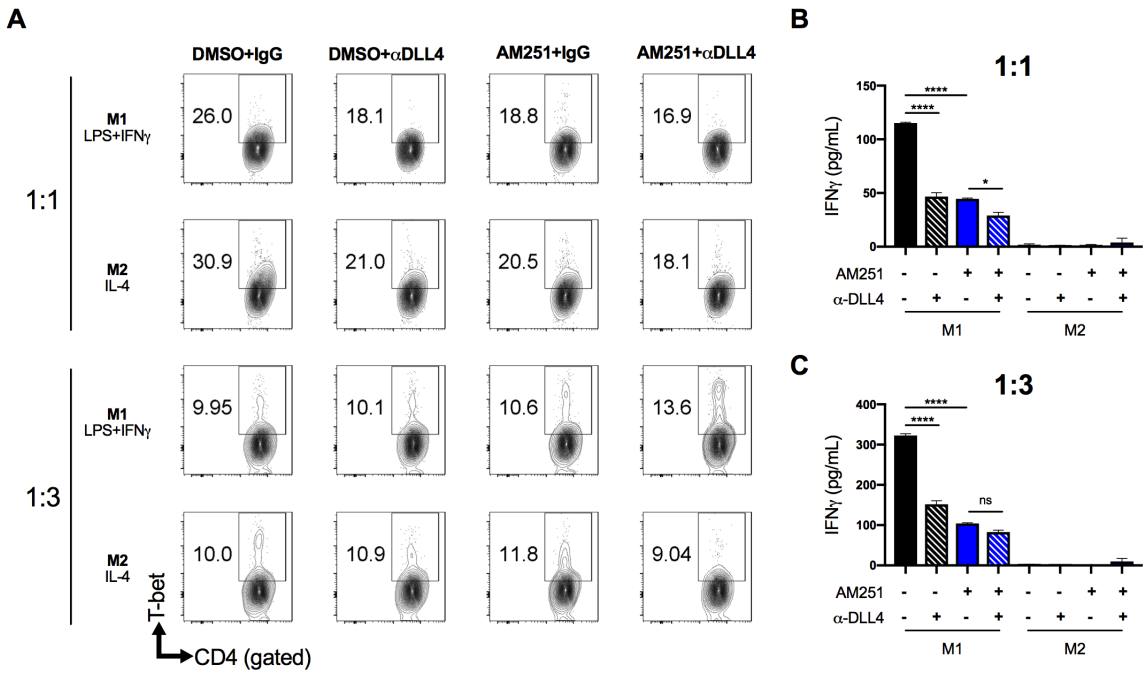

Figure 3.7 AM251 reduces expansion of pro-inflammatory Th1 cells by downregulating DLL4 in macrophages.
BMDM were pre-treated and polarized as described in Figure 3.6 legend. After 24hr of culture, the BMDM were washed and co-cultured with naïve lymphocytes at ratios of 1:1 or 1:3 (BMDM:lymphocytes) in the presence of 1ug/mL ConA for 48 hr. Resulting Th1 polarization of CD4+ lymphocytes was assessed. (A) Flow cytometry of CD4+T-bet+ Th1 lymphocytes. (B-C) IFNγ concentration in cell supernatants. Data are mean +/- SEM. ****p<0.0001, *p<0.05 by one-way ANOVA.

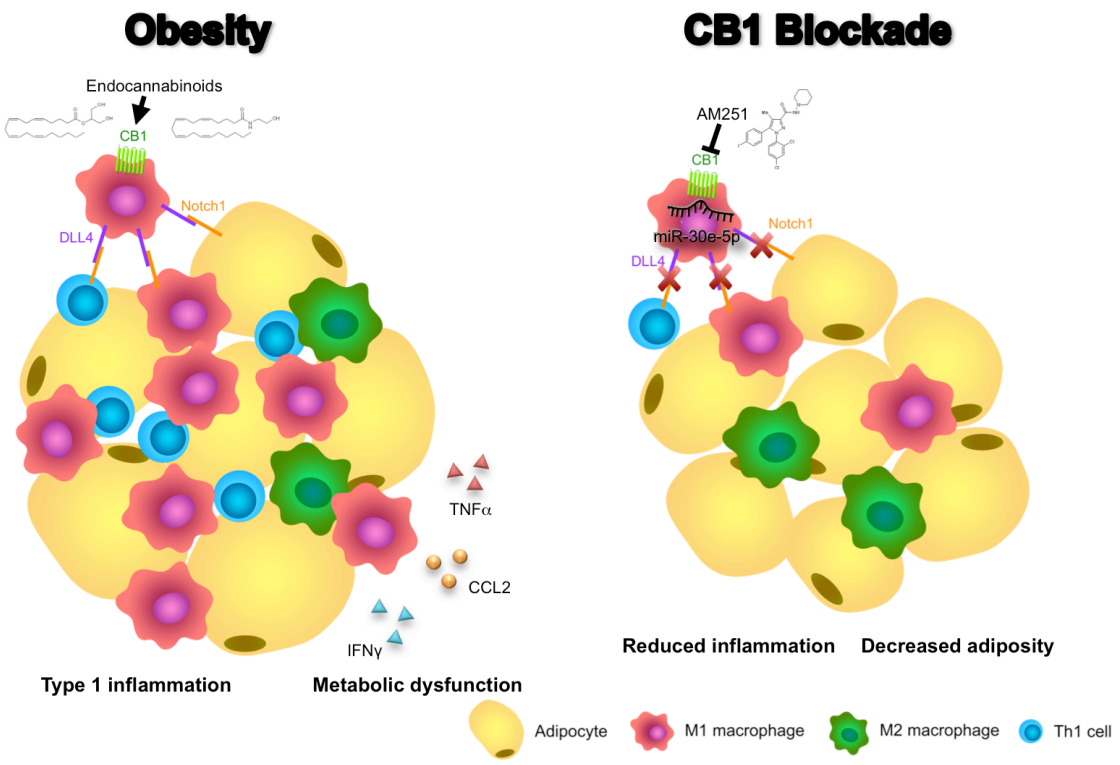

Figure 3.8 Blocking CB1 receptors reverses obesity through miR-30e-5p regulation of DLL4.
In this illustrative summary we demonstrate that blocking of CB1 receptors can reverse the inflammation and metabolic dysfunction observed in obese adipose tissue. During obesity, endocannabinoids activate CB1 to promote pro-inflammatory M1 macrophages and upregulation of DLL4. Subsequently, DLL4 activates Notch signaling on other macrophages, T cells, and adipocytes to promote M1 polarization, Th1 polarization, and adipocyte hypertrophy, respectively. As a result, pro-inflammatory cytokines and chemokines such as TNFα, CCL2, and IFNγ, and fat mass expansion, lead to metabolic dysfunction. Conversely, blocking of CB1 with AM251 reverses DLL4-Notch signaling-mediated inflammation and metabolic impairments due to upregulation of miR-30e-5p and downregulation of DLL4. As a result, fewer M1 macrophages and Th1 cells reside in the adipose tissue and energy expenditure increases to reduce fat mass.

CHAPTER 4

CANNABINOID RECEPTOR SIGNALING MEDIATES SUSCEPTIBILITY TO HIGH FAT DIET-INDUCED INTESTINAL DYSBIOSIS AND REGULATES METABOLIC HEALTH[3]

[3] Miranda, K., W. Becker, N. Dopkins, Y. Zhong, M.D. Walla, S.R. Donepudi, V. Putluri, N. Putluri, P.B. Busbee, P.S. Nagarkatti, and M. Nagarkatti. "Cannabinoid receptor signaling mediates susceptibility to high-fat diet-induced intestinal dysbiosis and regulates metabolic health." (Manuscript in preparation)

4.1 ABSTRACT

The endocannabinoid system (ECS) regulates a variety of obesity-related physiological processes including appetite, inflammation, and metabolism. Recent literature also suggests that the gut microbiota are tightly linked to obesity development; however, the role of the ECS in regulating obesity-induced intestinal dysbiosis is unclear. In the current study, genetic ablation of cannabinoid receptors CB1 and CB2, as well as pharmacological intervention were used in a mouse model of diet-induced obesity to determine the roles of the ECS in modulating inflammation, metabolism, and the gut microbiome. $CB1^{-/-}$ mice were resistant to high fat diet (HFD)-induced weight gain, metabolic dysfunction, and visceral adipose tissue M1 macrophage accumulation. Contrarily, $CB2^{-/-}$ mice displayed more severe obesity than wild-type mice. Additionally, treatment of obese mice with the CB1 antagonist AM251 led to weight loss, decreased adipose inflammation, and improvement in metabolic parameters. Interestingly, CB1 and CB2 were found to oppositely regulate HFD-induced leukocyte infiltration in the cecal-colonic lamina propria. Decreased intestinal inflammation upon CB1-blockade indicated ECS-mediated alterations in the gut microbiome might contribute to obesity phenotype. Microbiota profiling by 16S rRNA gene sequencing showed that $CB1^{-/-}$, but not $CB2^{-/-}$ mice were resistant to development of HFD-induced gut dysbiosis. Moreover, AM251 intervention in obese mice shifted their microbiota towards a lean profile. Co-housing and fecal transfer experiments in wild-type and $CB1^{-/-}$ mice indicated that microbiota composition was largely dispensable for improved obesity in $CB1^{-/-}$

mice, yet some composition differences remained. Further investigation of host:microbiota interactions by intestinal epithelial cell transcriptomics, serum metabolomics, and microbiota PICRUSt analyses revealed CB1-mediated regulation of intestinal barrier defense and gut microbiota-mediated sugar metabolism were involved in the pathogenesis of obesity. Together this study demonstrates that endocannabinoid signaling through CB1 and CB2 regulates metabolism by shaping intestinal immunity and mediating susceptibility to the obesity-associated microbial dysbiosis that promotes increased energy harvest.

4.2 INTRODUCTION

Obesity incidence is experiencing perpetual growth and robustly contributes to the global health burden due to many related complications that are triggered by chronic low-grade inflammation and metabolic dysfunction (Haslam and James, 2005). The endocannabinoid system (ECS) is a biological system that regulates a variety of obesity-related physiological processes including appetite, inflammation, and metabolism (Cani et al., 2016). Thus, regulation of this system is of high therapeutic interest for reducing obesity.

The ECS is comprised of cannabinoid receptors (CB) and their ligands called cannabinoids; named as such due to binding affinity for herbal ligands derived from *Cannabis sativa*. CBs are a class of G-protein coupled receptors widely expressed throughout the body. The two main cannabinoid receptors, CB1 and CB2, are expressed in various anatomical locations that coincide with their regulatory functions. CB1 expression is highly localized to the central

nervous system where it is well know to mediate the psychotropic effects of *Cannabis*, and additionally expressed in peripheral metabolic tissues such as the liver, adipose tissue (AT), muscle, gastrointestinal (GI) tract, and in some immune cells (Laprairie et al., 2012). As such, CB1 is heavily involved in regulation of energy metabolism and appetite. Conversely, CB2 is largely expressed in the immune system where it modulates inflammatory pathways including pain and cytokine release (Turcotte et al., 2016). Various studies from our laboratory have shown anti-inflammatory/immunosuppressive properties of CB2 agonists (Lombard et al., 2007; Singh et al., 2012; Tomar et al., 2015). Importantly, obesity is characterized by energy imbalance, chronic low-grade inflammation, and chronic ECS activation. Therefore, the ECS provides a mechanistic link between inflammation and metabolism during obesity that necessitates further investigation.

In the early 2000's it was discovered that stimulation of CB1 promotes development of obesity (Cota et al., 2003; Di Marzo et al., 2001). Blockade of CB1 reduced food intake in rodents and thus treatment of diet-induced obese mice with the CB1 antagonist SR141716A led to amelioration of both obesity and metabolic impairments (Cota et al., 2003; Ravinet Trillou et al., 2003). Furthermore, CB1 knockout mice were shown to be resistant to development of high fat diet (HFD)-induced obesity and insulin resistance (Ravinet Trillou et al., 2004). Indeed, pharmacological blockade or genetic ablation of CB1 lessened appetitive behaviors, however additional appetite-independent metabolic benefits were observed indicating an increase in energy expenditure when CB1 signaling

is impaired. Thus, CB1 became an attractive target for treatment of the ongoing obesity epidemic. Unfortunately, due to adverse neuropsychiatric effects, SR141716A, also known as Rimonabant, was removed from market. Despite this, research in the last decade has further characterized mechanisms of CB1 blockade-mediated metabolic improvements. Beneficial mechanisms of systemic CB1 antagonism beyond appetite regulation include decreasing obesity-associated inflammation through microRNA regulation of adipose tissue macrophages (ATM), increased brown adipose tissue thermogenesis, and increased insulin-dependent glucose utilization (Bajzer et al., 2011; Mehrpouya-Bahrami et al., 2019; Miranda et al., 2019). Adipocyte-specific CB1 knockout also increases energy expenditure and promotes anti-inflammatory M2 ATM polarization, which highlights the importance of peripheral CB1 receptors in metabolic regulation (Azua et al., 2017). In addition, recent evidence shows that peripherally restricted CB1 antagonists can be used to treat obesity without central side effects, albeit, their anti-obesity effects are slightly less than that of central-acting CB1 antagonists (Dong et al., 2018; Han et al., 2018).

While regulation of multiple obesity parameters appears to be CB1-dependent, the role of CB2 should not be discounted due to its involvement in immune system regulation. Knowing that obesity promotes a stage of chronic low-grade systemic and metabolic inflammation, which positively correlates with adiposity and insulin resistance, it is likely that CB2 plays important roles in obesity-related processes. Recent studies have identified non-synonymous polymorphisms in the *Cnr2* gene (the gene encoding CB2) can contribute to

overeating disorders (Ishiguro et al., 2010; de Luis et al., 2018). Aged $CB2^{-/-}$ mice also spontaneously develop pro-inflammatory obesity (Schmitz et al., 2016). Furthermore, treatment of mice with CB2 antagonists increases food intake, while CB2 agonists decrease appetite (Schmitz et al., 2016; Verty et al., 2015). Treatment of DIO mice with the CB2 agonist JWH-015 induces weight loss, lipolysis, and reduces inflammation in white adipose tissue (WAT), and additionally these effects were found to be independent of food restriction (Verty et al., 2015). These recent findings demonstrate that CB2 also plays key roles in energy homeostasis through modulation of the immune cells that contribute to insulin resistance, and moreover, reveals complementary roles of the CB1/CB2 balance in regulating immunometabolism that warrant further investigation.

Another entity that influences obesity phenotype is the community of trillions of microbes within the GI tract, also known as the gut microbiota (Cani, 2014; Zhao, 2013). It is becoming increasingly evident that environmental factors such as diet, exercise, stress, pharmaceuticals, and the like can alter the gut microbiota and impact host health (Dopkins et al., 2018). During obesity, altered microbiota composition leads to microbial dysbiosis that impairs health by contributing to gut inflammation, intestinal permeability, and increased energy harvest (Turnbaugh et al., 2006). To date, studies on ECS regulation of DIO-induced microbial dysbiosis are limited. Indeed a recent study from our laboratory demonstrated that blockade of CB1 signaling attenuates obesity and is associated with a shift in the gut microbiome composition that is associated with decreased intestinal permeability, increased microbial short chain fatty acid

(SCFA) production, and dampened adipose tissue macrophage (ATM)-mediated inflammation (Mehrpouya-Bahrami et al., 2017). Others have also demonstrated relationships between CB1 activation, intestinal permeability, decreased gut motility, and lipopolysaccharide (LPS)-regulated adipogenesis (Alhamoruni et al., 2010; Izzo et al., 2001; Muccioli et al., 2010). These findings indicate that gut microorganisms and the ECS are closely connected; however, the metabolites, receptors and signaling pathways that couple these, need to be more clearly defined in order to develop new therapeutic modalities (Cani et al., 2016).

In the current study, we used a mouse model of HFD-induced obesity in mice lacking functional CB1 or CB2 receptors to characterize influences of ECS on the gut microbiome, intestinal barrier function, inflammation, and metabolism. Microbiota composition and immune: microbial interactions in these models have not been previously reported. We also used a DIO intervention model to confirm therapeutic anti-obesity mechanisms of CB1 blockade. We hypothesized that the ECS contributes to metabolic and inflammatory tone through modulations of gut microbiota composition/metabolism and/or host microbial defense mechanisms, primarily through CB1-dependent mechanisms. Metabolic analyses, immune profiling, gut bacterial predictive metagenomics, intestinal epithelial cell transcriptomics, and serum metabolomics revealed CB1-dependent regulation of intestinal integrity and barrier protection, as well as regulation of microbial metabolic processes that correlate with body weight gain. Loss of CB2 signaling also worsened some obesity-related parameters that warrant further investigation. This study provides new insights into beneficial mechanisms of

CB1 blockade that promote metabolic health through host: microbial interactions, which may form the basis for new therapeutic modalities for obesity and related disorders.

4.3 Materials and Methods

Mice

Six- to 8-week-old male C57Bl/6J mice and 18-week-old male C57Bl/6J mice fed either 60% kcal HFD (D12492, Research Diets), or purified 10% low-fat diet (LFD, D12450J, Research Diets) where indicated, for 12 weeks were obtained from The Jackson Laboratory and housed in a specific-pathogen-free facility. $CB1^{-/-}$ constitutive knockout mice were gifted from Dr. James Pickel (NIH National Institute of Mental Health Transgenic Core Facility, Bethesda, MD, USA). $CB2^{-/-}$ constitutive knockout mice were obtained from The Jackson Laboratory. $CB1^{-/-}$ and $CB2^{-/-}$ mice were bred in-house and colonies maintained at the University of South Carolina School of Medicine animal facility. Mice were housed in separate cages (3-5 mice per cage) according to treatment group in all experiments except for the specified co-housing experiment. In all experiments, each treatment group consisted of mice from multiple litters and cages. In some instances mice were singly housed due to fighting. For DIO intervention studies, 12 week fed HFD-induced obese mice were stratified into treatment groups by equivalent mean DEXA fat mass. The treatment group was treated with AM251 (Tocris, 1117) at a dose of 10mg/kg suspended in 0.1% Tween 80 by oral gavage. All other experimental groups received Vehicle (Veh) gavages. Pair

feeding was performed by measuring the weight of HFD consumed each day, then administering that same weight of food to the Pair-fed group. At the conclusion of each study, mice were euthanized by overdose isoflurane inhalation. Experiments were performed in accordance with ethical standards approved by the University of South Carolina Institutional Animal Care and Use Committee.

Analytical Procedures

Body composition was measured by dual-energy x-ray absorptiometry (DEXA, LUNAR PIXImus) scanning as previously described(Miranda et al., 2018). Body weight was monitored using an electronic gram scale with precision ± 0.1g. For glucose tolerance tests, mice were fasted for 5hr, then fasting glucose was measured followed by oral gavage of 2g/kg lean mass glucose (Sigma G7528). Blood glucose was measured 15m, 30m, 60m and 120m after glucose gavage by applying approximately 5uL tail-tip blood to a glucose test strip in a glucometer (Contour Next, Bayer). To calculate a homeostatic model assessment of insulin resistance index (HOMA-IR), mice were fasted for 5hr then blood glucose was measured from the tail-tip. Immediately following, mice were euthanized by overdose isoflurane inhalation and ~500uL portal vein blood was collected and gently mixed with 15uL 0.5M EDTA. To isolate plasma, blood was centrifuged 5000 RPM, 5 min, 4°C and the top layer was collected and stored at -20°C. Insulin concentrations were measured in fasted plasma by ELISA (Invitrogen, EMINS). HOMA-IR index was calculated by the following equation [HOMA-IR= (fasting glucose x fasting insulin)/22.5] (Matthews et al., 1985).

Adipose Tissue Dissocation

Epididymal fat pads were excised, weighted, and dissociated using MACS adipose tissue dissociation kit and a gentleMACS dissociator according to manufacturer protocol (130-105-808, Miltenyi Biotec). The isolated stromal vascular fraction (SVF) was spun through a 33% (v/v) isotonic Percoll solution (1500 RPM, 15min, 25°C) prior to flow cytometry staining.

Intestinal dissociation for IEC and LPMC isolation

The cecum and colon were isolated from euthanized mice, cleaned of fecal matter, opened longitudinally, and mucus layer removed by gentle scraping in 1X HBSS. Cleaned tissues were cut into 0.5 cm segments and incubated in pre-warmed 1X HBSS (without Ca^{2+} and Mg^{2+}) containing 3% FBS, 10mM EDTA, and 5mM Dithiothreitol (DTT, Sigma) for 45 minutes at 37°C with shaking. The supernatant containing intra-epithelial leukocytes (IELs) and epithelial cells was recovered by filtering colon pieces through a 100um nylon mesh. This fraction was put on ice for at least 10 minutes to allow sedimentation of cellular debris. EpCAM+ IECs in the supernatant were then labeled with PE-labeled EpCAM (Clone G8.8, BioLegend) and immunomagnetically selected by PE-Positive Selection Kit (StemCell Tech). Flow cytometry was used to verify selection purity, which was greater than 85%.

For LPMC isolation, the remaining colon tissue was incubated in 15 mL digestion buffer for 45 m at 37°C with shaking to dissociate lamina propria cells. Digestion buffer consisted of 1X HBSS (with Ca^{2+} and Mg^{2+}) containing 3% FBS, 1% L-glutamine, 1% penicillin–streptomycin, 10 mM HEPES, 0.5 mg/mL

Collagenase D (Roche), 0.5 mg/mL Dispase (Sigma), and 0.04 mg/mL DNase I (Sigma). The supernatant was filtered through a 70um nylon mesh into ice cold 1X HBSS. Lamina propria cells were passed through a 40%/80% (v/v) Percoll (GE Healthcare) gradient and spun at 620xg for 20 minutes with low acceleration and no brake. LPMC at the 40/80 interface were collected and washed twice with Fluorescence Activated Cell Sorter (FACS) buffer (1X PBS, 2% FBS, 1mM EDTA) and used flow cytometry analysis.

Isolation of spleen single cell suspensions

Spleens were excised from euthanized mice and disrupted in 5mL FACS buffer utilizing a Stomacher80 machine (Seward). Homogenates were filtered through a 70um nylon mesh, pelleted, RBC-lysed, and washed in FACS buffer prior to flow cytometry staining.

Flow Cytometry

For surface staining, cells were incubated with FcR-Blocker for 10m followed by appropriate fluorochrome-conjugated antibodies for 30m (CD45 clone 30-F11, CD11b clone M1/70, F4/80 clone BM8, CD11c clone N418, CD4 clone GK1.5, Foxp3 clone MF-14, T-bet clone 4B10, LAP clone TW7-16B4, BioLegend). For intracellular staining of transcription factors, Biolegend TrueNuclear Intracellular Staining kit was used according to manufacturer protocol. Stained cells were washed with FACS buffer then analyzed on a BD FACSCelesta flow cytometer. Data were analyzed and visualized with FlowJo v10.

Short chain fatty acid extraction and quantification

SCFA were acidified and extracted from flash frozen cecal contents according to a previously published protocol from our laboratory (Mehrpouya-Bahrami et al., 2017). The extraction method was modified to use tert-Butyl methyl ether as the extraction solvent. 2-ethylbutyric acid was used as the internal standard. External calibration standards were prepared to determine retention times. Samples and standards were detected by gas chromatography coupled with flame-ionization detection at the University of South Carolina Mass Spectrometry Center. Sample concentrations were calculated as previously described (Mehrpouya-Bahrami et al., 2017).

Intestinal permeability measurements

In vivo assay of intestinal epithelial barrier permeability was performed by FITC-Dextran assay as previously described (Chassaing et al., 2015). Mice were food and water fasted for 4 h then gavaged with 15 mg of FITC-labeled 4kD dextran (Sigma, FD4), then re-allowed ad libitum access to food and water. Blood was collected retro-orbitally 4 h after gavage in isoflurane-anaesthetized mice. Serum was collected and diluted 1:1 (v/v) with PBS and the fluorescein (excitation 485nm) measurements were performed on a plate reader (Victor2). FITC concentration was calculated using a standard curve of serially diluted FITC-dextran in normal mouse serum. Lipopolysaccharide leakage into blood circulation was quantified in mouse serum by LPS ELISA kit (LSBio, LS-F17912).

16S Predictive Metagenomics Sequencing and Analysis

Stool DNA was isolated with QIAamp DNA Stool Mini Kit (Qiagen). 16S rRNA gene V3-V4 regions were amplified and sequencing libraries were

generated following the Illumina Demonstrated Protocol “16S Metagenomic Sequencing Library Preparation” (Part # 15044223 Rev. B). Equimolar pooled libraries were quantified using Qubit dsDNA HS assay (Life Technologies) then sequenced using an Illumina MiSeq sequencer (paired-end reads, 2 x 301 base pairs). De-multiplexed FASTQ files were obtained from Illumina BaseSpace Sequence Hub and analyzed through the NIH Nephele pipeline (FASTQ Paired-end 16S using QIIME)(Weber et al., 2018). Sequences were pre-processing filtered by a minimum quality score of 19 and max ambiguous score of 0. Reads were joined with a maximum bad run length of 3, minimum overlap length of 10, and percent differences within overlap of 25. The Greengenes_99 Reference database was used for a closed reference clustering and classification analysis including Phylogenetic Investigation of Communities by Reconstruction of Unobserved States (PICRUSt) annotations (Langille et al., 2013). Chimeras were removed using UCHIME (Edgar et al., 2011). For diversity analysis, the fraction of maximum sample size was set to 0.2. For Linear discriminant analysis (LDA) effect size (LEfSe), the Huttenhower Lab Galaxy instance (https://huttenhower.sph.harvard.edu/galaxy) was used(Segata et al., 2011). Data input were % of total operational taxonomic units (OTUs) per sequencing sample. All default analysis parameters were used. LEfSe results were plotted as cladograms in Galaxy.

Antibiotic administration and fecal microbiota transfer

Five-week-old male C57BL6 mice were depleted of resident microbiota by housing mice in autoclaved cages containing autoclaved food and sterile drinking

water containing antibiotics (Abx) as previously described(Li et al., 2017). The antibiotics administered include 1 mg/mL bacitracin, 170 ug/mL gentamycin, 125 ug/mL ciprofloxacin, 100 ug/mL neomycin, 100 U/mL penicillin, 100 ug/mL metronidazole, 100 ug/mL ceftazidime, 50 ug/mL streptomycin, and 50 ug/mL vancomycin (Sigma) and were provided fresh once per week. After 4 weeks of Abx administration, stool was isolated for bacterial culture and qRT-PCR for *Eubacteria* normalized to *18S* to confirm microbiota depletion. The Abx-treated mice were then transferred into dirty donor cages for 4 days then gavaged with 200mg donor feces suspended in PBS, which was harvested under anaerobic conditions. The mice were then maintained in autoclaved cages and fed ad libitum irradiated HFD (Research Diets, D12492i) for 3 weeks to monitor weight gain.

RNA isolation, cDNA synthesis, and qRT-PCR

Total RNA was isolated from cells by lysing in Qiazol then using miRNeasy Mini/Micro kits (Qiagen) according to manufacturer protocol. When required, the RNA was reverse transcribed to cDNA with iScript cDNA synthesis kit (BioRad). Quantitative RT-PCR for mRNA expression was performed with SSO Advanced Universal SYBR Green supermix (BioRad). For bacterial qRT-PCR QuantiFast SYBR Supermix (Qiagen) was used. The primers used were purchased from Integrated DNA Technologies (Lyz2- Fwd: ATG GAA TGG CTG GCT ACT ATG G, Rev: ACC AGT ATC GGC TAT TGA TCT GA, Beta-actin- Fwd: GGC TGT ATT CCC CTC CAT CG, Rev: CCA GTT GGT AAC AAT GCC ATG T , 18S- Fwd: GCC CGA GCC GCC TGG ATA, Rev: CCG GCG GGT CAT

GGG AAT AAC , Eubacteria- Fwd: ACT CCT ACG GGA GGC AGC AGT, Rev: ATT ACC GCG GCT GCT GGC).

Transcriptome microarrays

Ten ng of total RNA isolated from ccIECs was used as starting material for each transcriptome microarray. cDNA synthesis, in vitro transcription, cRNA amplification, ss-cDNA synthesis, purification and quantification steps, fragmentation and labeling, and hybridization to MTA1.0 chips was performed with the Applied Biosystems GeneChip WT Pico Reagent Kit. The hybridized chips were then washed, stained, and scanned on an Affymetrix GCS 3000 system using the fluidics protocol FS450_0001. The generated .CEL files were analyzed for quality and normalized to converted .CHP files using Transcriptome Analysis Console v.4.0.1.36 (Applied Biosystems). The summarization and normalization method used was Gene + Exon – SST-RMA. Genes were considered differentially expressed between groups if the Log_2 fold change was ≥ 1.5 or ≤ -1.5.

Serum Metabolomics

Serum metabolomics experiments were performed at the Baylor College of Medicine according to previously published methods (Amara et al., 2019; Putluri et al., 2011a, 2011b; Vantaku et al., 2017, 2019). Reagents and internal standards, high-performance liquid chromatography (HPLC)-grade acetonitrile, methanol, and water were procured from Burdick & Jackson (Morristown, NJ). Mass spectrometry-grade formic acid was purchased from Sigma-Aldrich (St

Louis, MO). Calibration solution containing multiple calibrants in a solution of acetonitrile, trifluroacetic acid, and water was purchased from Agilent Technologies (Santa Clara, CA). Metabolites and internal standards, including N-acetyl Aspartic acid-d3, Tryptophan-15N2, Sarcosine-d3, Glutamic acid-d5, Thymine-d4, Gibberellic acid, L-Threonic acid, Trans-Zeatine, Jasmonic acid, 15N Anthranilic acid, and Testosterone-d3, were purchased from Sigma-Aldrich (St. Louis, MO).

Internal Standard Solution and Quality controls- Aliquots (200 µL) of 10 mM solutions of N-acetyl Aspartic acid-d3, Tryptophan-15N2, Sarcosine-d3, Glutamic acid-d5, Thymine-d4, Gibberellic acid, L-Threonic acid ,Trans-Zeatine, Jasmonic acid, 15N Anthranilic acid, and Testosterone-d3 were mixed and diluted up to 8 ml (final concentration 0.25 mM) and aliquoted into a 20 µL portions. The aliquots were dried and stored at -80°C. Two kinds of controls were used to monitor the sample preparation and mass spectrometry. To monitor instrument performance, 20 µL of a matrix-free mixture of the internal standards described above, reconstituted in 100 µL of methanol: water (50:50) and analyzed by SRM. Other control is use of serum pool spiked with mixture of internal standards, extracted along with test samples and measured by SRM.

Sample Preparation- 50ul of each serum sample was taken. To this 750 µL ice-cold methanol:water (4:1) containing 20 µL spiked internal standards was added to each tissue sample. Ice-cold chloroform and water was added in a 3:1 ratio for a final proportion of 4:3:2 methanol:chloroform:water. The organic (methanol and chloroform) and aqueous layers were mixed, dried and resuspended with 50:50

methanol: water. The extract was deproteinized using a 3kDa molecular filter (Amicon ultracel-3K Membrane; Millipore Corporation, Billerica, MA) and the filtrate was dried under vacuum (Genevac EZ-2plus; Gardiner, Stone Ridge, NY). Prior to mass spectrometry, the dried extracts were re-suspended in identical volumes of injection solvent composed of 1:1 water: methanol (100ul) and were subjected to liquid chromatography-mass spectrometry using a 6495-triple quadrupole mass spectrometer (Agilent Technologies, Santa Clara, CA) coupled to a HPLC system (Agilent Technologies, Santa Clara, CA)

Method A: Measurement of glycolytic intermediates, TCA cycle; To target the glycolysis, TCA, the samples were delivered to the mass spectrometer via normal phase chromatography using a Luna 3 um NH2 100 A (150 x 2mm) (Phenomenex, Torrance, CA) in ESI/MS negative ion mode. Source parameters were as follows: Gas temperature was 250 °C; Gas flow was 11 l/min; Nebulizer was 20psi; Sheath gas temperature was 300 °C; Sheath gas flow was 11 l/min; Capillary was 3000 V positive and 3500 V negative; Nozzle voltage was 1500 V positive and 1500 V negative. The mobile phase was water solvent A modified by the addition of 5mM ammonium acetate (pH 9.9), and 100% acetonitrile (ACN) solvent B. The binary pump flow rate was 0.2 ml/min with a gradient spanning 80% B to 2% A over a 20-minute period followed by 2% solvent B to 80% solvent A for a 5 min period and followed by 80% B for 13-minute. The flow rate was gradually increased during the separation from 0.2 mL/min (0–20 mins), 0.3 mL/min (20.1–25 min), 0.35 mL/min (25–30 min), 0.4 mL/min (30–37.99 min) and finally set at 0.2 mL/min (5 min). The injection volume was 10ul.

Method B: In ESI positive mode the HPLC column was waters X-bridge amide 3.5 µm, 4.6 x 100 mm (Waters Milford, MA). Mobile phase A and B were 0.1% formic acid in water and acetonitrile respectively. Gradient flow: 0-3 min 85 % B; 3-12 min 30 % B, 12-15 min 2 % B, 16 min 95% B, followed by re-equilibration till the end of the gradient 23 min to the initial starting condition of 85% B. Flow rate of the solvents used for the analysis is 0.3 ml/min. The injection volume was 5µL.

Method C: In ESI negative mode the HPLC column was waters X-bridge amide 3.5 µm, 4.6 x 100 mm (Waters, Milford, MA). Mobile phase A and B were 20mM ammonium acetate in water with pH 9.0 and 100% acetonitrile respectively. Gradient flow: 0-3 min 85% B, 3-12 min 30% B, 12-15 min 2%B, 15-16 min 85% B followed by re-equilibration till the end of the gradient 23 min to the initial starting condition of 85% B. Flow rate of the solvents used for analysis is 0.3 ml/min. The injection volume was 10µL.

Statistical Analysis

For serum metabolomics, Agilent Mass Hunter Workstation Software Quantitative Analysis was used for manual review of chromatograms, and peak area was integrated based on the retention time. The normalization of each metabolite peak area was done relative to the peak area of the spiked internal standard, and then the data were $\log_2$ transformed.

Other statistical analyses were performed with GraphPad Prism Version 8.1.1 for Mac (GraphPad Software). Data presented are mean (± SEM) or box and whisker plots with individual points representing biological replicates. One-

way ANOVA was used for multiple group analyses and two-way ANOVA was used for significance across multiple variables. Significance differences between body weight curves were determined by non-parametric one-way ANOVA with a Dunn's test. Linear regression analysis was used for correlation analyses. A p value ≤ 0.05 was considered statistically significant.

4.4 RESULTS

Loss of endocannabinoid signaling through CB1 promotes resistance to DIO.

To study the role of the ECS in modulating HFD-induced obesity, metabolic inflammation, and gut microbial dysbiosis, we fed 6-8-week-old male wild-type (WT) C57Bl/6J, $CB1^{-/-}$, and $CB2^{-/-}$ mice with HFD (60% kcal fat) or control LFD (10% kcal fat) for 16 weeks while monitoring DIO development. $CB1^{-/-}$ mice have been previously characterized to display a delayed obesity phenotype whereas HFD-induced DIO in $CB2^{-/-}$ has not been previously reported to our knowledge (Ravinet Trillou et al., 2004). To validate our experimental model, body weight growth was monitored weekly (Figures 4.1A-4.1C). Consistent with previous reports, $CB1^{-/-}$ mice were resistant to HFD-induced weight gain when compared to $CB1^{-/-}$ mice fed LFD (Figure 4.1B). Conversely, HFD-fed WT and $CB2^{-/-}$ mice displayed significant weight gain versus LFD-fed mice over 16 weeks of diet (Figures 4.1A & 4.1C). The mean final weights expressed as a percent of starting weight in WT, $CB1^{-/-}$, and $CB2^{-/-}$ mice fed LFD were 131.2%, 124.6%, and 148.0%, respectively (Figure 4.1D). WT, $CB1^{-/-}$, and $CB2^{-/-}$ mice fed HFD averaged 201.8%, 163.3%, and 205.0% their starting

weight, respectively (Figure 4.1D). The differences in final body weight percent between LFD- and HFD-fed mice within each genotype were 70.6% for WT, 38.7% for $CB1^{-/-}$, and 57.0% for $CB2^{-/-}$ (Figure 4.1D). Food intake was measured weekly and showed that HFD- versus LFD-fed WT and $CB2^{-/-}$ mice displayed hedonic polyphagia while HFD-fed $CB1^{-/-}$ consumed similar calories to LFD-fed $CB1^{-/-}$ (Figure 4.1E). Thus, a WT pair-fed control group (WT HFD $^{PF\ CB1-/-}$) was used to control for differences in feeding behavior in $CB1^{-/-}$ mice. The WT mice that were pair-fed to $CB1^{-/-}$ HFD mice displayed body weight growth similar to $CB1^{-/-}$ HFD mice (Figures 4.1B & 4.1D). DEXA body composition measurements revealed weight gain was consistent with predominantly increased adiposity, although WT and $CB2^{-/-}$ also had significant increases in lean mass after 16 weeks of diet (Figures 4.1G-4.1I). In addition, HFD feeding caused elevated liver weights in WT and $CB2^{-/-}$ mice but not in $CB1^{-/-}$ mice, which indicated that $CB1^{-/-}$ mice might also be resistant to obesity-induced hepatosteatosis (Figure 4.2A). When evaluating feed efficiency, we found that HFD-fed mice of all genotypes gained more body weight per kcal consumed versus LFD-fed mice (Figure 4.1F). Still, $CB1^{-/-}$ HFD mice gained less weight per kcal consumed versus both WT HFD and $CB2^{-/-}$ HFD, which indicated enhanced energy expenditure in $CB^{-/-}$ mice (Figure 4.1F). H&E staining of interscapular brown adipose tissue further supported enhanced energy expenditure in $CB1^{-/-}$ mice because they maintained similar mitochondria to lipid ratios in HFD- versus LFD-fed mice, while WT and $CB2^{-/-}$ displayed increased lipid accumulation after HFD-feeding, that was more pronounced in $CB2^{-/-}$ mice (Figure 4.2B).

To evaluate the development of obesity-associated glucose intolerance and insulin resistance we performed oral glucose tolerance tests and calculated HOMA-IR. HFD-fed mice of all genotypes displayed signs of glucose intolerance versus their LFD-fed counterparts after 16 weeks of diet, although to a lesser extent in $CB1^{-/-}$ mice (Figures 4.1J & 4.1K). Furthermore, the development of HFD-induced glucose intolerance was delayed in $CB1^{-/-}$ versus WT and $CB2^{-/-}$ mice, as glucose intolerance was not observed until 16 weeks on HFD in $CB1^{-/-}$ mice, whereas $CB2^{-/-}$ mice developed intolerance after 8 weeks of HFD and WT mice after 12 weeks of HFD (Figure 4.2C). Further assessments of fasting glucose, insulin, and HOMA-IR revealed that HFD-fed $CB1^{-/-}$ mice maintained insulin sensitivity after 16 weeks of feeding while HFD-fed WT and $CB2^{-/-}$ mice became insulin resistant (Figures 4.1L-4.1M). Together these data indicate $CB1^{-/-}$ mice are resistant, whereas WT and $CB2^{-/-}$ mice are prone to development of HFD-induced obesity and metabolic impairments.

Endocannabinoid signaling regulates obesity-induced inflammation.

A hallmark of the obese state is inflammation in metabolic tissues such as the adipose tissue. Growth in adiposity triggers infiltration of pro-inflammatory immune cells into the adipose tissue, a majority of which are M1 macrophages that produce pro-inflammatory cytokines and chemokines that promote insulin resistance (Lumeng et al., 2007). To determine the role of the ECS in ATM polarization, we isolated stromal vascular fractions (SVF) from epididymal fat of mice after 16 weeks of diet and performed immunophenotyping by flow cytometry. Increased ATM infiltration was observed in WT HFD mice versus WT

LFD mice as well as in $CB2^{-/-}$ HFD versus $CB2^{-/-}$ LFD (Figure 4.3A). Interestingly, $CB1^{-/-}$ mice were resistant to HFD-induced ATM infiltration even though HFD-fed $CB1^{-/-}$ mice had increased epididymal fat mass when compared to $CB1^{-/-}$ LFD (Figures 4.3A & 4.3B). ATM count per gram of adipose tissue was also less in $CB1^{-/-}$ HFD versus both WT HFD and $CB2^{-/-}$ HFD (Figure 4.3C). Furthermore, increased ATM infiltration coincided with an increase in ATM CD11c expression in WT and $CB2^{-/-}$ mice, indicating that the infiltrating ATMs were predominantly M1 macrophages (Figures 4.3A & 4.3D). All together, beneficial effects on adipose inflammation in $CB1^{-/-}$ mice was found to be primarily an effect of decreased appetite as ATM inflammation in WT $HFD^{PF\ CB1-/-}$ mice was similar to $CB1^{-/-}$ HFD mice (Figures 4.3A-4.3D).

Next, to study the role of the ECS in gut immunity we performed flow cytometry on lamina propria mononuclear cells (LPMCs) from the ceca-colons of mice after 16 weeks of diet. We found that HFD feeding in WT and $CB2^{-/-}$ mice promoted infiltration of $CD45^+$ leukocytes into the lamina propria (Figure 4.3E). Immune infiltrates included $CD4^+$T-bet^+ and $CD4^+LAP^+$ populations that have been previously reported to be associated with irritable bowel diseases (Figures 4.4A & 4.4B) (D'Ambrosio et al., 2016; Neurath et al., 2002). Alternatively, $CB1^{-/-}$ HFD mice maintained $CD45^+$ populations similar to $CB1^{-/-}$ LFD mice indicating resistance to HFD-induced intestinal inflammation in mice lacking CB1, although WT pair-fed mice had further reductions in CD45+ cells (Figure 4.3E). $CB1^{-/-}$ also did not experience HFD-induced intestinal permeability as HFD-fed WT and $CB2^{-/-}$ mice had elevated gut leakage shown by increased circulating FITC-dextran

and LPS, respectively (Figure 4.4C & 4.4D). Of note, $CB2^{-/-}$ HFD mice had higher percentages of $CD45^{+}$ cells than WT HFD and $CB1^{-/-}$ HFD mice, indicating that loss of CB2 worsens intestinal inflammation (Figure 4.3E). Furthermore, we investigated the short chain fatty acid (SCFA) profile of cecal content because SCFAs, particularly butyrate, are associated with beneficial effects of microbiota (Baxter et al., 2019). Interestingly, we found that while cecal butyrate was downregulated in HFD- versus LFD-fed WT mice and trended less in HFD- versus LFD-fed $CB2^{-/-}$ mice, concentration remained consistent in $CB1^{-/-}$ mice between diets (Figure 4.3F). $CB1^{-/-}$ HFD mice also had more butyrate versus WT pair-fed mice, which hinted that $CB1^{-/-}$ mice might have an improved microbiota profile that may contribute to improved obesity parameters (Figure 4.3F).

To further investigate the inflammatory status of mice after 16 weeks of purified diet, we performed flow cytometry on splenocytes for T cell subsets and butyrate is known to promote regulatory T cell (Treg) differentiation (Furusawa et al., 2013). We found that LFD- and HFD-fed $CB1^{-/-}$ mice had elevated levels of Foxp3+ Tregs in the spleen versus other genotypes and the pair-fed control (Figure 4.3G). Together, our data from various tissues indicated that $CB1^{-/-}$ suppresses HFD-induced inflammation through beneficial effects of caloric restriction and Treg-mediated immunosuppression, and may improve intestinal immunity and microbial dysbiosis that is associated with obesity.

Non-functional CB1 alters susceptibility to HFD-induced intestinal dysbiosis.

Many reports indicate that obesity is associated with altered gut microbiota that influence host processes such as metabolism and inflammation, promoting

intestinal dysbiosis (Sonnenburg and Bäckhed, 2016). To identify alterations in gut microbiota in our receptor knockout model we performed predictive metagenomics by 16S rRNA gene sequencing. Stool DNA was isolated before (Baseline, “BL”) and after 16 weeks of purified diet feeding and used for 16S V3-V4 amplicon sequencing. We found that baseline alpha-diversity was greater within microbiotas of CB1$^{-/-}$ and CB2$^{-/-}$ versus WT mice (Figure 4.5A). Sixteen weeks of purified diet reduced alpha diversity in all genotypes but to a lesser extent in CB1$^{-/-}$ mice (Figure 4.5A). Beta-diversity principle component analysis (PCoA) showed distinct clustering of the groups (Figure 4.5B). Differences in principle components PC1 and PC3 could be mostly explained by genotype and husbandry practices. At baseline, the CB1$^{-/-}$ and CB2$^{-/-}$ clusters were more similar to each other while the WT mice were more different (Figure 4.5B). Purified diet feeding shifted the gut microbiota composition of all genotypes upward on PC2, though to a lesser extent in LFD- versus HFD-fed mice of all genotypes. Interestingly, CB1$^{-/-}$ HFD mice showed a similar shift as CB1$^{-/-}$ LFD mice because their group clusters overlapped (Figure 4.5B).

At the phyla level of taxonomy, baseline microbiota compositions were significantly altered amongst the genotypes as WT mice had a greater Firmicutes to Bacteroidetes ratio than both the CB1$^{-/-}$ and CB2$^{-/-}$ mice (Figures 4.5C, 4.5E, & 4.6). Verrucomicrobia were also present at baseline in WT but not in CB1$^{-/-}$ or CB2$^{-/-}$ mice. The baseline microbiota composition of CB1$^{-/-}$ and CB2$^{-/-}$ showed a lot of similarity, however CB1$^{-/-}$ had more TM7, while CB2$^{-/-}$ had more Proteobacteria (Figures 4.5C, 4.5E, & 4.6). HFD feeding in WT mice decreased

Bacteroidetes and coincided with a bloom in the Verrucomicrobia phyla, which is comprised of the species *Akkermansia muciniphila,* and whose abundance was similar between *ad libitum*-fed and pair-fed control groups (Figures 4.5C, 4.5E, & 4.6). Microbiota composition in $CB1^{-/-}$ showed little change at the phyla level after 16 weeks of LFD or HFD, but $CB1^{-/-}$ HFD mice had greater abundance of Deferribacteres (comprised solely of the murine commensal *Mucispirillum schaedleri*) and TM7 (comprised of unclassified F16) than HFD-fed mice of other genotypes (Figure 4.5C, 4.5E, & 4.6). Similar to WT mice, $CB2^{-/-}$ mice experienced HFD-induced reduction in Bacteroidetes, but instead coincided with expansion of Proteobacteria (Figures 4.5C & 4.5E).

Microbiota transfer between WT and $CB1^{-/-}$ mice does not alter obesity susceptibility.

Given that $CB1^{-/-}$ mice were resistant to HFD-induced gut microbial changes, we asked whether their microbiota composition could also directly confer resistance to DIO development in WT mice, or if WT HFD feces transfer could accelerate DIO development in $CB1^{-/-}$ mice. We used co-housing and fecal microbiota transplant (FMT) experiments to transfer microbial populations between genotypes then challenged the mice with HFD feeding. Co-housing has been shown to lead to continual seeding of microbiota between animals (Blanton et al., 2016). We first placed naïve C57BL6 WT and $CB1^{-/-}$ into 2 mice per cage that were separated by genotype (Separate-housing) or co-housed between genotypes (Figure 4.7A). Mice continued a standard chow diet for 10 days to promote microbiota transfer through coprophagy then challenged with 16 weeks

of HFD. Body weight growth curves demonstrated that co-housing did not alter susceptibility to DIO development because weight gain was similar between separate- and co-housed mice of each genotype (Figure 4.7B). Co-housing also did not affect body composition or adipose inflammation (Figures 4.8A-4.8C). We next sequenced 16S V3-V4 rRNA gene regions of stool DNA to confirm microbial transfer in co-housed mice. Stool samples were collected after 10 days of co-housing but before HFD (Pre/Baseline) and again after 16 weeks of HFD (Post). In separately housed groups, $CB1^{-/-}$ mice again had greater alpha diversity at baseline versus WT mice (Figure 4.7C). Co-housing of WT with $CB1^{-/-}$ increased alpha diversity of WT mice (Figure 4.7C). Sixteen weeks of HFD led to minimal changes in alpha-diversity versus baseline measures (Figure 4.7C). Principle component analysis of beta diversity revealed that just 10 days of co-housing of mice could shift WT microbiotas towards the dominant $CB1^{-/-}$ microbiota composition, while separately housed WT mice maintained a distinct microbiota profile (Figure 4.7D). Interestingly, $CB1^{-/-}$ mice were resistant to microbial alterations regardless of housing conditions (Figure 4.7D). At the phyla level of taxonomy, similar trends were seen in separately housed groups as shown in Figure 4.5 (i.e. HFD induced decreased Bacteroidetes and increased Verrucomicrobia in WT mice whereas $CB1^{-/-}$ mice were resistant to microbial changes) (Figure 4.7E). Co-housed WT and $CB1^{-/-}$ mice showed microbiota compositions very similar to separately housed $CB1^{-/-}$ mice; however, the $CB1^{-/-}$ microbiotas remained distinctly clustered of co-housed WT mice (Figure 4.7D).

Phyla level and genera level microbiota profiles of the individual mice are represented in Figures 4.8D & 4.8E.

In addition to the co-housing experiment, we performed a fecal microbiota transfer (FMT) experiment in antibiotic (Abx) treated mice. C57BL6 WT mice were treated with Abx in drinking water for 4 weeks and maintained on standard chow diet in autoclaved cages to deplete their microbiota (Figure 4.9A). Abx-treated mice were then placed in dirty donor cages 4 days prior to FMT gavage of donor feces (Figure 4.9A). Microbiota depletion after 4 weeks of Abx was confirmed by stool culture and bacterial qRT-PCR (Figures 4.9B & 4.9C). As a result, FMT from $CB1^{-/-}$ to WT mice did not confer resistance to acute weight gain after HFD challenge (Figure 4.9D).

Together our co-housing and FMT experiments indicated that transfer of $CB1^{-/-}$ feces into WT mice did not alter susceptibility to DIO development, albeit complete microbial transfer was not achieved. Thus $CB1^{-/-}$ mice may likely be resistant to HFD-induced intestinal dysbiosis due to host microbial defense mechanisms or the rare microbes that are maintained in the dominant $CB1^{-/-}$ microbiota.

Blockade of CB1 receptors reverses DIO and shifts the gut microbiota composition.

To further understand how CB1 regulates microbiota and host interactions we used a DIO intervention model with the CB1 antagonist AM251. CB1 antagonists are well-known to induce weight loss, reduce inflammation, and improve glucose metabolism however studies on the interactions with the gut

microbiota are few to date (Mehrpouya-Bahrami et al., 2017, 2019; Miranda et al., 2019). Male C57BL6 mice were fed LFD or HFD for 12 weeks prior to intervention. AM251 was administered daily for 4 weeks at a dose of 10mg/kg by oral gavage. Non-treated mice received Vehicle (Veh) gavages. In addition, a pair-fed control was included to control for decreased appetite observed in AM251-treated mice. Body weight was monitored during the 4-week intervention and showed that LFD+Veh mice maintained initial weight while HFD+Veh mice gained weight (Figure 4.10A). HFD+AM251 mice quickly lost weight during the first week of treatment and maintained weight loss for the remainder of the experiment (Figure 4.10A). Weight loss coincided with suppressed appetite (Figure 4.10B). Interestingly, the HFD-Pair-fed mice did not loose as much weight and eventually gained back all their starting weight (Figure 4.10A). Overall, body weight curves were significantly different in all of the experimental groups (Figure 4.10A). DEXA fat percentage measurements showed that HFD-fed groups had equivalent Pre treatment (Tx) fat mass that was significantly greater than LFD+Veh mice (Figure 4.10C). Post 4 weeks of treatment, HFD+Veh and HFD-Pair-fed mice gained, whereas LFD+Veh mice maintained, and HFD+AM251 mice lost fat percentage versus Pre Tx (Figure 4.10C). At the Post Tx timepoint fat percentage was significantly less in HFD+AM251 treated mice versus both HFD+Veh and HFD-Pair-fed, though pair-fed mice displayed an intermediate fat percentage (Figures 4.10C & 4.10D). Fasting blood glucose was also significantly reduced in HFD+AM251 mice versus both HFD+Veh and HFD-Pair-fed mice (Figure 4.10E). In addition, DIO-induced inflammation was reduced

in adipose tissue and the ccLP (Figures 4.10F-4.10H). Furthermore intestinal barrier integrity appeared improved with treatment, as HFD+AM251 mice had reduced plasma LPS concentrations versus HFD+Veh mice (Figure 4.10I).

When investigating microbiota composition Pre Tx and Post Tx by 16s V3-V4 rRNA gene sequencing, we observed little alterations in alpha diversity (Figure 4.10J). Beta diversity was similar Pre Tx in all the HFD-fed groups but distinct from LFD+Veh (Figure 4.10K). Post Tx, HFD+AM251 microbiota composition shifted on PC3 similarly to LFD+Veh, while HFD+Veh and HFD-Pair-fed clustered closer together (Figure 4.10K). At the phyla level, Post Tx HFD+AM251 microbiotas more closely resembled those of LFD+Veh (Figurse 4.10L & 4.11A). Interestingly, HFD+AM251 mice had increased abundance of genera belonging to the Clostridiales order (Figures 4.11B & 4.11C). This trend was similar to that observed in WT LFD versus WT HFD mice shown in Figure 4.6C indicating that AM251 treatment in DIO WT mice shifts microbiota composition towards a lean profile and may have beneficial effects on DIO.

CB1 alters transcriptome profiles of intestinal epithelial cells relating to host defense.

To investigate potential host microbial defense mechanisms we performed transcriptome analyses on EpCAM+ intestinal epithelial cells (IEC) isolated from the ceca: colons of mice from the both the CB receptor knockout model and AM251 DIO intervention model (Figures 4.12A-4.12D). $CB1^{-/-}$ HFD IECs were found to have 188 genes differentially expressed (Fold change ≥ ± 1.5) versus all other HFD-fed groups (WT HFD, WT $HFD^{PF\ CB1-/-}$, and $CB2^{-/-}$ HFD), and are

displayed in a heatmap (Figure 4.12A). HFD+AM251 IECs displayed 203 differentially expressed genes versus both HFD+Veh and HFD-Pair-fed (Figure 4.12B). When comparing those genes that were similarly dysregulated in $CB1^{-/-}$ HFD and HFD+AM251 IECs, we identified 15 genes that are likely regulated by appetite-independent CB1 knockout or antagonism (Figure 4.12C). These include upregulation of antimicrobial peptide (AMP) genes *Lgals2*, *Lyz2*, and *Reg3b* (Figure 4.12D). Ingenuity Pathway Analysis (IPA, Qiagen) showed that the upregulated genes related to an increased antimicrobial response and decreased inflammatory response with increased cellular viability and cell-cell adhesion (Figure 4.12E). Expression of *Lys2* was found to be reproducibly induced by qRT-PCR validation (Figure 4.12F). Together, transcriptome data from our models indicated that CB1 may regulate intestinal integrity and host antimicrobial defense through modulation of AMP gene expression.

CB1 regulates host and microbiota carbohydrate metabolism.

We next investigated potential gut microbiota metabolic pathways that are affected following CB1 knockout/blockade, which may contribute to altered host metabolism. To first identify host metabolic pathways affected, we performed tricarboxylic acid cycle (TCA)-targeted metabolomics on fasting serum samples from WT, $CB1^{-/-}$, or $CB2^{-/-}$ mice fed LFD or HFD for 16 weeks. Of the 108 metabolites detected, 33 were differentially expressed in $CB1^{-/-}$ HFD versus at least one other HFD-fed group and whose mean expression relative to internal control are displayed in a heatmap (Figure 4.13A). ANOVA analyses further identified metabolites that were similarly regulated in $CB1^{-/-}$ HFD versus both WT

HFD and CB2$^{-/-}$ HFD and are identified by bold text* (Figure 4.13A). Furthermore, 4 metabolites that were similarly regulated in CB1$^{-/-}$ HFD versus all three HFD-fed groups (WT HFD, WT HFD$^{PF\ CB1-/-}$, and CB2$^{-/-}$ HFD) are denoted by bold text** (Figure 4.13A). MetaboAnalyst pathway analysis of the host metabolic pathways affected by these 4 differentially expressed metabolites identified overlap with TCA cycle, glycolysis/gluconeogenesis, and alanine, aspartate, and glutamate metabolism (Figure 4.13B). The two metabolites that correlated with these pathways, were ketoglutarate and phosphoenolpyruvate (PEP), and were downregulated in CB1$^{-/-}$ HFD mice (Figures 4.13C & 4.13D). Furthermore, we looked to microbiota metabolic pathways regulated by CB1 through PICRUSt analysis of 16S sequencing data. We found that the microbial functional pathways of glycolysis: gluconeogenesis, phosphotransferase system (PTS), and fructose and mannose metabolism were upregulated in HFD- vs. LFD-fed mice of WT and CB2$^{-/-}$ genotypes but unchanged or downregulated with CB1$^{-/-}$ HFD (Figures 4.13E-4.13G).

We looked further at the reproducibility of this trend in our co-housing and AM251 DIO intervention model. In the co-housing model, glycolysis: gluconeogenesis, PTS, and fructose and mannose metabolism were again downregulated in separately housed HFD-fed CB1$^{-/-}$ versus WT mice (Figures 4.13H-4.13J). Interestingly, co-housed CB1$^{-/-}$ mice maintained downregulation of PTS, and fructose and mannose metabolism pathways versus co-housed WT mice, which indicated that regulation of these pathways were specific to CB1$^{-/-}$ mice and may result from the rare microbes that remained differentially

expressed in co-housed CB1$^{-/-}$ mice versus co-housed WT mice (Figures 4.13I and 4.13J). PEP is also the phosphate donor for the PTS system, which imports sugars such as fructose and mannose into bacterial cells, and PEP was greatly reduced in CB1$^{-/-}$ HFD mice versus all other groups (Figure 4.13D). In addition, downregulation of these microbial metabolic pathways appeared to be dependent on CB1 signaling as blockade of this receptor in DIO mice also reduced microbial gene counts of glycolysis: gluconeogenesis, PTS, and fructose and mannose metabolism pathways versus DIO vehicle and pair-fed controls (Figures 4.13K-4.13M). Together these data indicated that CB1 signaling activation promotes carbohydrate metabolism pathways that may increase energy harvest of intestinal microbiota and contribute to body weight gain.

Microbiota sugar metabolism positively correlates with body weight.

Given that we had downregulation of serum metabolites and microbial metabolic pathways related to sugar metabolism, we performed linear regression analyses to correlate microbial metabolic pathways with host obesity parameters including fasting blood glucose and end-point body weight. Data from mice of receptor knockout, co-housing, and DIO intervention models were pooled for analyses (Figure 4.14A). Fasting blood glucose measurements were not associated with abundance of glycolysis: gluconeogenesis, PTS, or fructose and mannose metabolism pathways in microbiota, indicating that host substrate availability may not be responsible for altered expression of these pathways (Figures 4.14B-4.14D). Excitingly, these metabolic pathways positively correlated with body weight, which supports the overall conclusion that increases in these

microbial pathways contribute to increased capacity for energy harvest in DIO microbiomes (Figures 4.14E-4.14G). In particular, enrichment of PTS and fructose and mannose metabolism PICRUSt pathways in human obesity are supported in previous publications (Hou et al., 2017; Liu et al., 2017).

4.5 Discussion

The anti-obesity effects of $CB1^{-/-}$ and CB1 antagonism are well documented yet the anti-obesity, microbiota-related mechanisms are not well understood. Additionally, the role of CB2 in obesity-related processes has not been widely investigated, but is important for understanding ECS regulation of immunometabolism. In this study, we used multiple DIO models to identify novel host: microbial interactions regulated by cannabinoid receptor signaling that could form the basis for microbiota-related therapeutics.

First, we performed HFD-induced obesity studies in CB1 and CB2 knockout mice. In accordance with previous reports, $CB1^{-/-}$ mice were resistant to HFD-induced weight gain, adipose expansion, and development of insulin resistance versus WT and $CB2^{-/-}$ mice. These effects appeared to be largely due to decreased calorie intake in $CB1^{-/-}$ mice; however, energy intake-independent benefits observed in $CB1^{-/-}$ HFD mice included decreased fasting blood glucose that was similar to lean mice. It is also noteworthy that anti-obesity effects observed in the WT $HFD^{PF\ CB1-/-}$ pair-fed control group could have been in part due to intermittent fasting because this group ate all the supplied food each day and likely experienced significant amounts of time without food access between

daily feedings. The anti-obesity effects of intermittent fasting have been previously documented, therefore it was challenging to control for appetite in our model (Li et al., 2017). Indeed, the DIO intervention model with AM251 demonstrated some anti-obesity effects of CB1 blockade beyond the effect of appetite restriction including increased weight loss, decreased ATM percentage, and decreased fasting blood glucose. We also report here for the first time the development of HFD-induced obesity in $CB2^{-/-}$ mice. Body weight growth and body composition of $CB2^{-/-}$ HFD mice was similar to WT HFD mice, however $CB2^{-/-}$ HFD mice developed glucose intolerance earlier and had more lipid accumulation in brown adipose tissue and therefore, were more susceptible to DIO than WT mice. These data confirm previous anti-obesity effects of $CB1^{-/-}$ and identify the importance of CB2 signaling in metabolic regulation.

Inflammation in adipose tissue is a hallmark of the obese state that can be triggered by metabolic stress that activates innate immunity due to the release of damage-associated molecular patterns (Vandanmagsar et al., 2011). In addition, alterations of obese microbiome increase circulating LPS levels that activate cytokine production and promote metabolic endotoxemia that exacerbates chronic inflammation and metabolic dysfunction (Cani et al., 2007, 2008). In the current study, we found that adipose tissue, intestinal inflammation, and intestinal barrier function improved in $CB1^{-/-}$ mice primarily through beneficial effects of reduced caloric intake. Furthermore, $CB1^{-/-}$ mice showed HFD-induced increases in the anti-inflammatory microbial metabolite butyrate, which could have contributed to their increased induction of Tregs overall decreased inflammatory

state, as previously shown in other models (Furusawa et al., 2013). Together these data indicated that CB1$^{-/-}$ mice were resistant to the exacerbation of metabolic inflammation that arises from gut microbiota-mediated intestinal dysbiosis. Furthermore, elevated intestinal inflammation and leakage in DIO CB2$^{-/-}$ mice demonstrates an important role for CB2 activation in maintaining gut homeostasis. Our group has previously shown therapeutic value of the CB2 agonist JWH-133 in the IL10$^{-/-}$ murine model of chronic colitis (Singh et al., 2012). More recently we have shown that administration of the phytocannabinoid, delta-9-tetrahydrocannabinol, reduces severity of multiple murine colitis models through immune-mediated effects of CB2 activation (data not shown, Becker et al., in submission). Overall, the opposing observations of intestinal barrier function between DIO CB1$^{-/-}$ and CB2$^{-/-}$ mice suggested that in normal mice, increased endocannabinoid signaling through CB2 is beneficial in maintaining gut homeostasis and that this may have contributed to the improvements observed in CB1$^{-/-}$ mice.

When we characterized the microbiota composition of WT, CB1$^{-/-}$, and CB2$^{-/-}$ mice before and after 16 weeks of diet we noticed many significant alterations but markedly, CB1$^{-/-}$ mice were resistant to HFD-induced alterations in microbiota composition. This suggested that either their dominant microbiota composition could be protective against DIO development, or alternatively, reduced DIO development in CB1$^{-/-}$ could have been responsible for these reduced alterations in microbiota profile. Surprisingly, *A. muciniphila* was absent in CB1$^{-/-}$ and CB2$^{-/-}$ microbiotas. This bacterium has been reported to improve

obesity and metabolism by increasing intestinal levels of the endocannabinoids, 2-Oleoylglycerol and 2-Arachidonylglycerol, which improve barrier function and decrease inflammation (Everard et al., 2013; Plovier et al., 2017). It is possible that endocannabinoid signaling through CB1 and CB2 is necessary for the survival of *A. muciniphila*, or *A. muciniphila* could be out-competed by other microbes present in $CB1^{-/-}$ and $CB2^{-/-}$ microbiotas, but the mechanisms involved require further investigation. Also unexpectedly, we observed a substantial increase of *A. muciniphila* in WT HFD versus WT LFD mice, suggesting that overgrowth of this bacterium could be detrimental in the context of DIO. On the whole, it is evident that the mechanisms of *A. muciniphila* regulation of metabolism are complex and context-dependent. Other differences observed in $CB1^{-/-}$ HFD mice included increased abundances of *M. schaedleri,* and unclassified F16. *M. schaedleri* is a border dwelling, mucus-degrading commensal that protects against *Salmonella*-induced colitis in mice, and has been shown to thrive in niche established by extrathymically generated Tregs (Campbell et al., 2018; Herp et al., 2019). The F16 family has been reported to be enriched in lean male mice; however, the precise functions of this family are currently unknown (Qin et al., 2018). Furthermore, $CB1^{-/-}$ versus $CB2^{-/-}$ mice had less abundance of the phylum Proteobacteria that contains many pathogenic bacteria and whose abundance is enriched in human obesity (Méndez-Salazar et al., 2018). Overall, the gut microbiome of $CB1^{-/-}$ mice displayed a dominant phenotype that was resistant to changes associated with obesity, and enriched in

protective commensals that likely maintain barrier function and immune homeostasis.

To better understand the role of the $CB1^{-/-}$ microbiome in protecting against DIO, we performed co-housing and FMT experiments in WT and $CB1^{-/-}$ mice. This was especially important for data interpretation inasmuch as baseline microbiota composition of WT and $CB1^{-/-}$ were dramatically different, and co-housing is an effective way to standardize microbiota, though the mucosal microbiota can be difficult to normalize (Robertson et al., 2019). Remarkably, only 10 days of co-housing was able to shift the WT stool microbiota composition towards a $CB1^{-/-}$ profile, yet the $CB1^{-/-}$ composition did not change between co-housed and separately housed mice. This further demonstrated that $CB1^{-/-}$ mice have a dominant microbiota composition whose colonization is firmly established. Despite similar microbiome compositions in WT and $CB1^{-/-}$ mice, DIO development was not altered indicating that the beneficial effects of $CB1^{-/-}$ are due to host-driven mechanisms or the small community of microbes that remained differentially expressed after co-housing.

We also investigated the microbiome composition of DIO mice treated with the CB1 antagonist AM251. In accordance with a previous report from our lab, CB1 antagonist treatment attenuated obesity, decreased inflammation in adipose tissue and cecum: colon, and reduced metabolic endotoxemia (Mehrpouya-Bahrami et al., 2017). The gut microbiota shift with AM251 treatment also showed a change similar to that of lean control mice. These data confirmed that $CB1^{-/-}$ or CB1 blockade have beneficial effects on the DIO gut microbiota

composition, yet from our co-housing and FMT experiments we found that the microbiota composition is largely dispensable for the improved obesity phenotype. Therefore, we further investigated host- and microbiota-mediated mechanisms of intestinal barrier function and metabolism, and correlated the findings between our receptor knockout and intervention models.

To accomplish this, we performed transcriptomics on EpCAM+ intestinal epithelial cells from ceca: colons of mice. $CB1^{-/-}$ and AM251 treatment altered the transcriptome profiles of ccIECs. Interestingly, upregulation of a few AMPs were observed in both models, indicating their expressions are regulated by CB1. For example, *Lyz2* expression was reproducibly elevated in HFD+AM251 ccIECs. This gene encodes lysozyme 2 and lysozymes are glycosidases produced by Paneth cells that can directly kill bacteria by hydrolyzing peptidoglycan (Mukherjee and Hooper, 2015). Paneth cell production of lysozyme is decreased in both murine and human obesity (Guo et al., 2017; Hodin et al., 2011). This suggests that upregulation of *Lyz2* contributes to shaping gut immunity, barrier integrity, and microbiota composition during CB1 knockout/blockade and provides protection against DIO-induced dysbiosis (Figure 4.15).

Next we investigated the serum metabolome and altered gut microbiota PICRUSt pathways to correlate changes in circulating metabolites with microbial processes. Most strikingly, serum PEP was reduced in $CB1^{-/-}$ HFD. PEP is an important intermediate in biochemistry involved in glycolysis: gluconeogenesis in organisms as well as the microbial PTS. PEP contains the highest energy phosphate bond found in all organisms. Phosphoenolpyruvate carboxykinase-

mediated conversion of oxaloacetate to PEP is the rate-limiting step in gluconeogenesis (Nelson et al., 2008). In the PTS, PEP provides the source of energy for bacterial import and phosphorylation of various monosaccharides such as glucose, fructose, and mannose (Mahowald et al., 2009). Reduced levels of PEP in $CB1^{-/-}$ HFD mice indicated that gluconeogenesis was reduced in these animals. Importantly, increased PEP-dependent gluconeogenesis contributes to increased adiposity in human obesity (Chevalier et al., 2006). Furthermore, predicted PICRUSt pathways in the gut microbiota showed downregulation of glycolysis: gluconeogenesis, PTS, and fructose and mannose metabolism pathways across our various models. It was recently shown that PTS and fructose and mannose metabolism are enriched in obese human microbiomes, yet the precise mechanisms of how these pathways relate increased energy harvest were not investigated (Liu et al., 2017). In our model, correlation analysis showed that these microbial pathways are positively correlated with body weight gain but not fasting blood glucose measurements. Overall, these findings supported gut microbiota involvement in regulation of host obesity through CB1-dependent regulation of microbial sugar metabolism. Future research aimed at modulating these bacterial pathways during obesity could provide further insight into microbiota-mediated mechanisms of energy harvest.

In summary, our study shows that over activation of the ECS in DIO impairs intestinal barrier function and promotes increased energy storage. CB1 knockout or blockade had beneficial effects on host metabolism that was at least in part due to improved host intestinal barrier function, likely due to increased

endocannabinoid signaling through CB2, as well as downregulation of carbohydrate metabolic pathways in gut microbiota that together decreased inflammatory tone and energy harvest, thus reducing obesity and its complications.

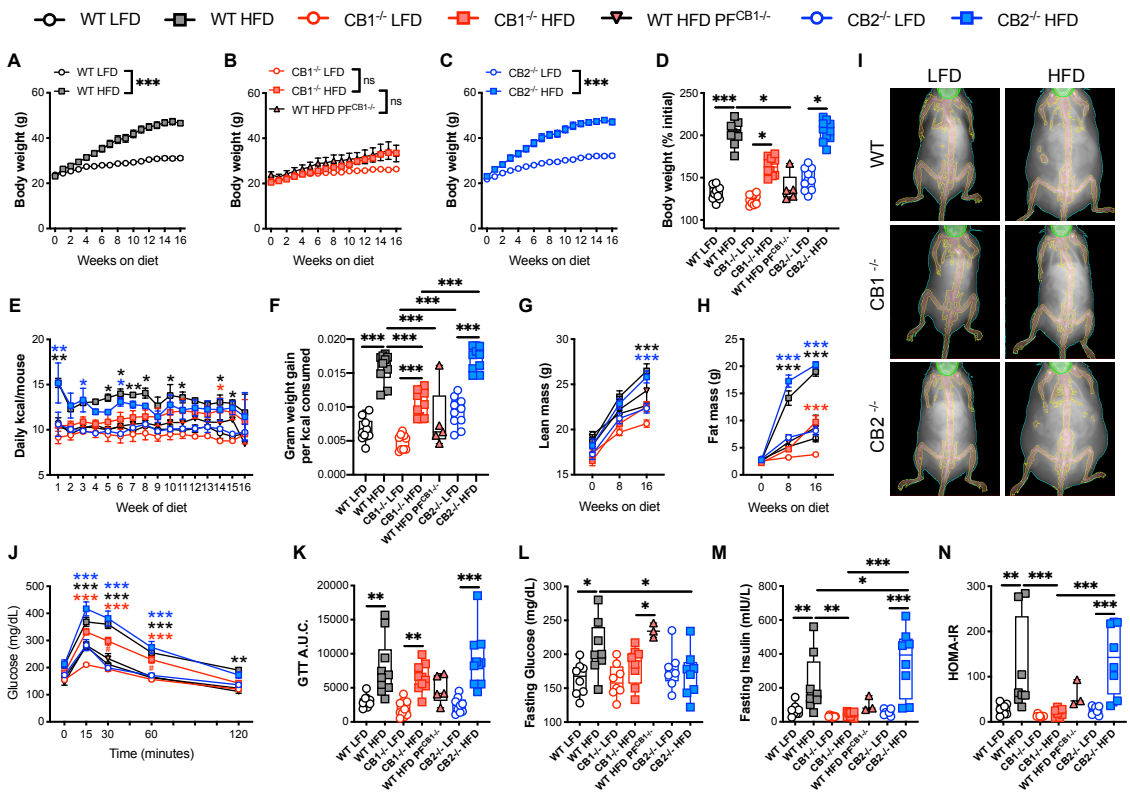

Figure 4.1 CB1 deletion promotes resistance to DIO.
Male C57Bl6 WT, CB1$^{-/-}$, and CB2$^{-/-}$ mice were fed purified LFD or HFD for 16 weeks. Body weight and composition as well as glucose metabolism were repeatedly analyzed during 16 weeks of diet feeding. (A-C) Body weight growth curves for WT (A), CB1$^{-/-}$ (B), and CB2$^{-/-}$ (C) mice over 16 weeks of diet. (D) Percentage of body weight gain during 16-weeks of feeding. (E) Mean daily kcal consumed per mouse. N=2 experiments. (F) Feed efficiency calculated by weight gain per kcal consumed over 16 weeks of diet. (G) DEXA lean mass measured every 8 weeks of diet. (H) DEXA fat mass measured every 8 weeks of diet. (I) Representative DEXA scans. (J) Oral glucose tolerance test (GTT) performed after 16 weeks of diet. (K) Area under the curve (A.U.C) for the GTT performed in (J). (L) Fasting glucose measured after 16 weeks of diet. (M) Fasting insulin measured after 16 weeks of diet. (N) HOMA-IR measured after 16 weeks of diet. Data shown are mean +/- SEM or box and whisker plots with each point representing biological replicates. N=10 mice/group except N=5 for WT HFD$^{PF\ CB1-/-}$. *p<0.05, **p<0.01, ***p,0.001 vs. LFD within each genotype (colored by genotype- WT: black, CB1$^{-/-}$: red, CB2$^{-/-}$: blue) or as indicated by a line. Significance was determined by one- or two-way ANOVA.

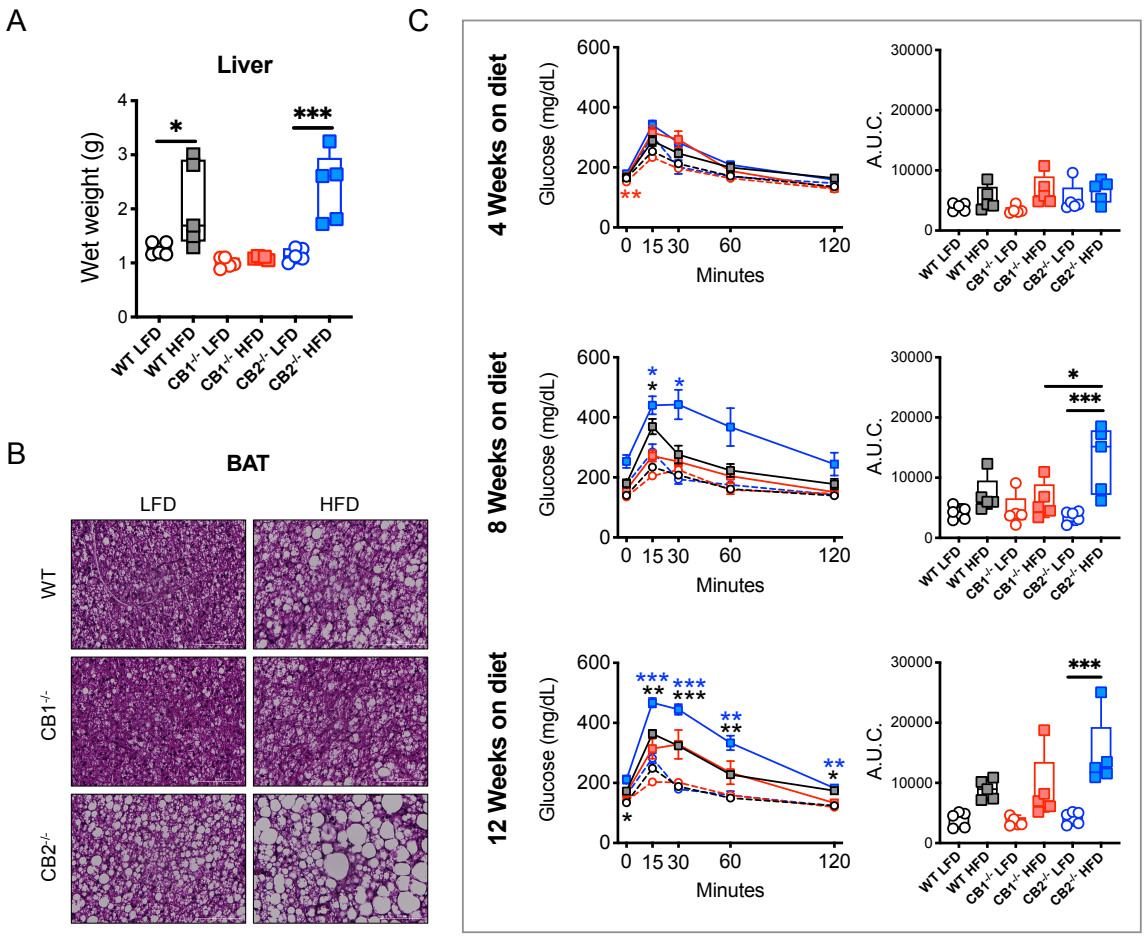

Figure 4.2 CB1 knockout delays DIO development and glucose intolerance. As described in Figure 4.1, male C57Bl6 WT, CB1-/-, and CB2-/- mice were fed purified LFD or HFD for 16 weeks. (A) Liver wet weight after 16 weeks of diet. (B) Representative H&E micrographs of interscapular brown adipose tissue (BAT) after 16 weeks of diet. (C) GTTs and A.U.C.s performed after 4, 8, and 12 weeks of diet. Data shown are mean +/- SEM or box and whisker plots with each point representing biological replicates. N=5 mice/group except N=3 mice/group for (B). *p<0.05, **p<0.01, ***p,0.001 vs. LFD within each genotype (colored by genotype- WT: black, CB1$^{-/-}$: red, CB2$^{-/-}$: blue) or as indicated by a line. Significance was determined by one- or two-way ANOVA.

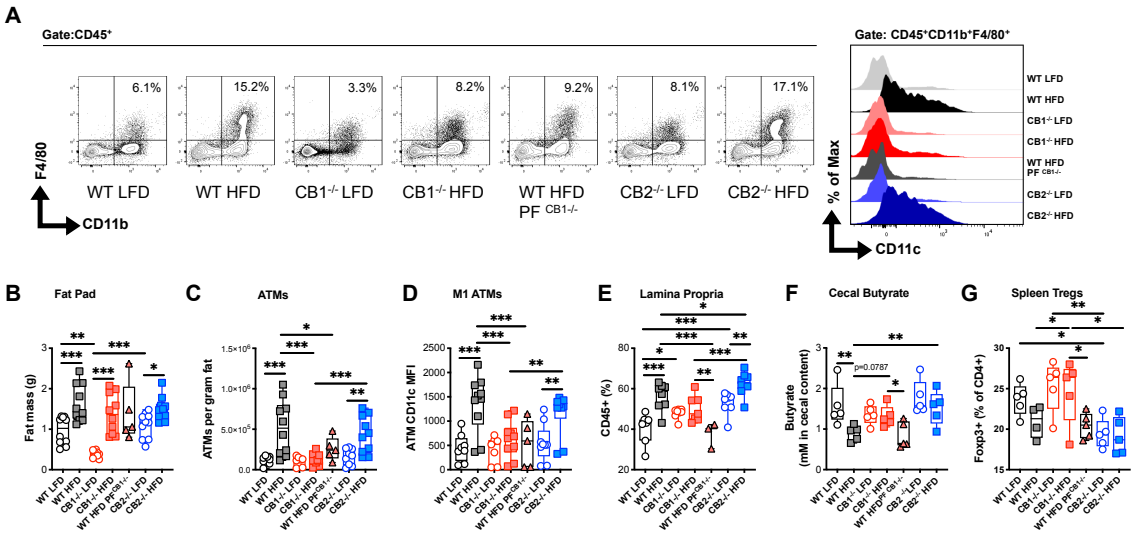

Figure 4.3 Loss of CB1 suppresses HFD-induced inflammation.
As described in Figure 4.1 legend, male C57Bl6 WT, CB1-/-, and CB2-/- mice were fed purified LFD or HFD for 16 weeks. Inflammation in adipose tissue, spleen, and cecal-colonic lamina propria was analyzed by flow cytometry. (A) Representative flow cytometry plots of epididymal fat ATMs and ATM-gated CD11c MFI. (B) Epididymal fat pad mass. (C) Total ATMs per gram of epididymal adipose tissue. (D) CD11c MFI on ATMs to estimate M1 ATM polarization. (E) Percentage of CD45+ leukocytes in cecal-colonic lamina propria. (F) Concentration of butyrate in cecal content after 16 weeks of diet. (G) Percentage of CD4+Foxp3+ Tregs in spleen. Data shown are mean or box and whisker plots with each point representing biological replicates. N=5-10 mice/group. *p<0.05, **p<0.01, ***p,0.001 by one-way ANOVA.

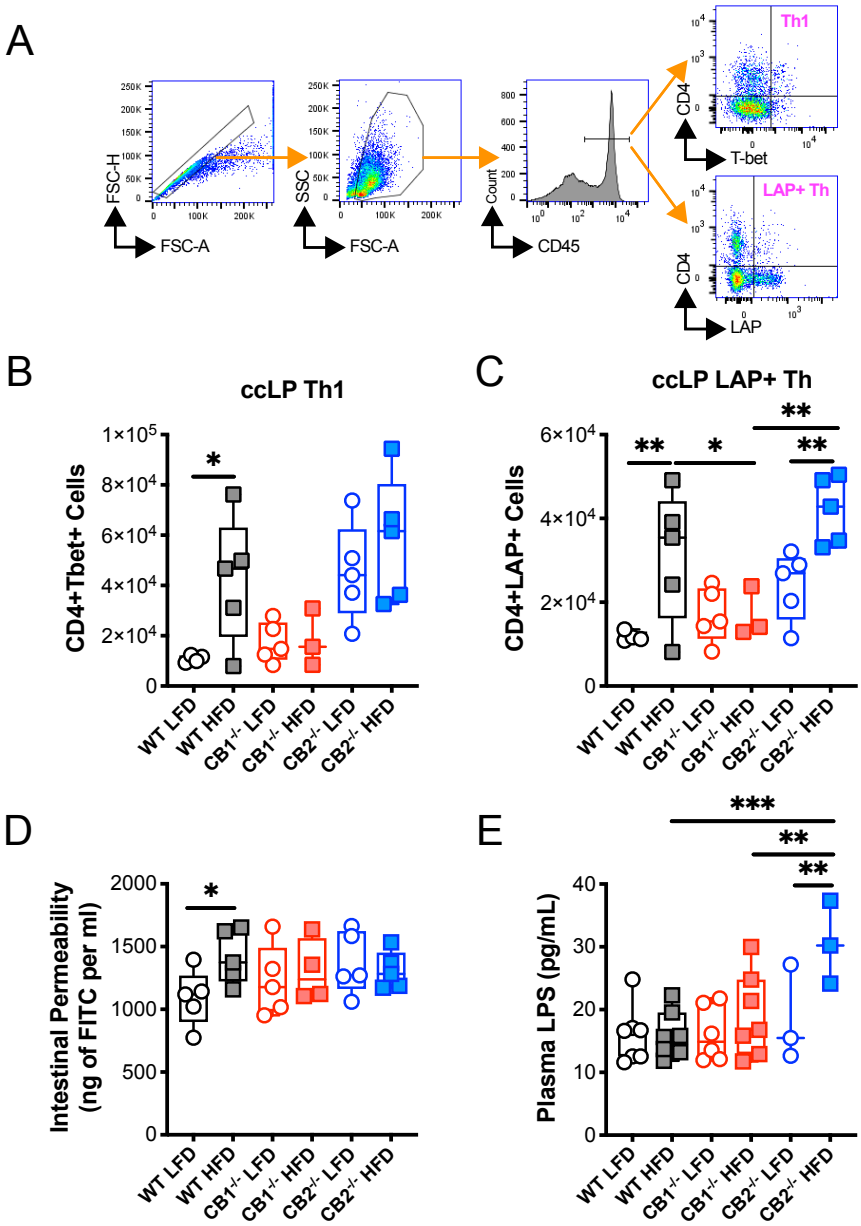

Figure 4.4 Loss of CB1 suppresses HFD-induced intestinal inflammation and permeability.
As described in Figure 1 legend, male C57Bl6 WT, CB1-/-, and CB2-/- mice were fed purified LFD or HFD for 16 weeks. Inflammation in cecal-colonic lamina propria (ccLP) was analyzed by flow cytometry. Estimates of intestinal permeability were assessed by FITC-dextran assay and plasma endotoxin levels. (A) ccLP flow cytometry gating strategy. (B) CD4+T-bet+ Th1 cell count in ccLP. (C) CD4+LAP+ Th cell count in ccLP. (D) FITC-dextran (4kD) in plasma. (E) LPS concentration in plasma. Data shown are box and whisker plots with each point representing biological replicates. N=3-8 mice/group. *p<0.05, **p<0.01, ***p,0.001 by one-way ANOVA.

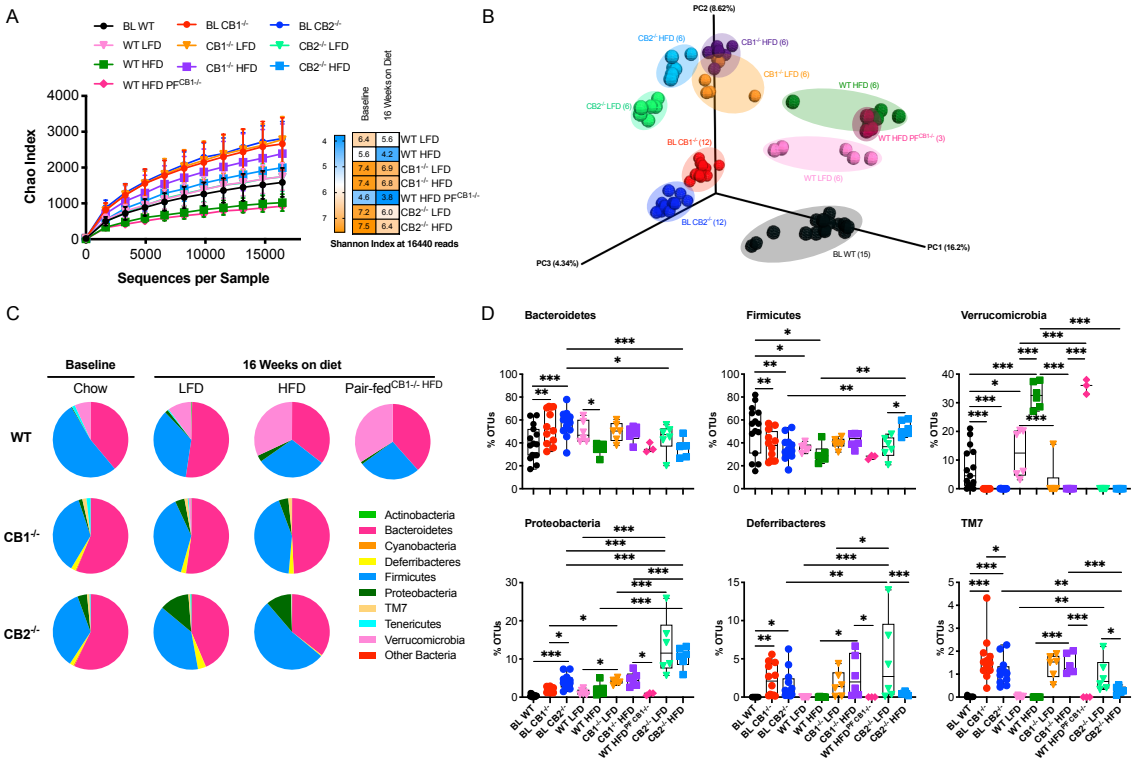

Figure 4.5 CB1$^{-/-}$ mice are resistant to HFD-induced alterations in gut microbiota.

As described in Figure 4.1 legend, male C57Bl6 WT, CB1$^{-/-}$, and CB2$^{-/-}$ mice were fed purified LFD or HFD for 16 weeks. Stool samples were collected pre- (Baseline, "BL") and post- 16 weeks of purified diet for 16S V3-V4 rRNA gene sequencing. (A) Alpha diversity by Chao and Shannon indices. (B) 3D PCoA plot of unweighted UniFrac beta diversity. (C) Mean relative abundance of each bacterial phyla displayed as a pie chart per group. (D) OTU % of significantly altered phyla for each biological replicate. Data shown are mean (+/- SEM) or box and whisker plots with each point representing biological replicates. N=3-15 mice/group. *p<0.05, **p<0.01, ***p,0.001 by one-way ANOVA.

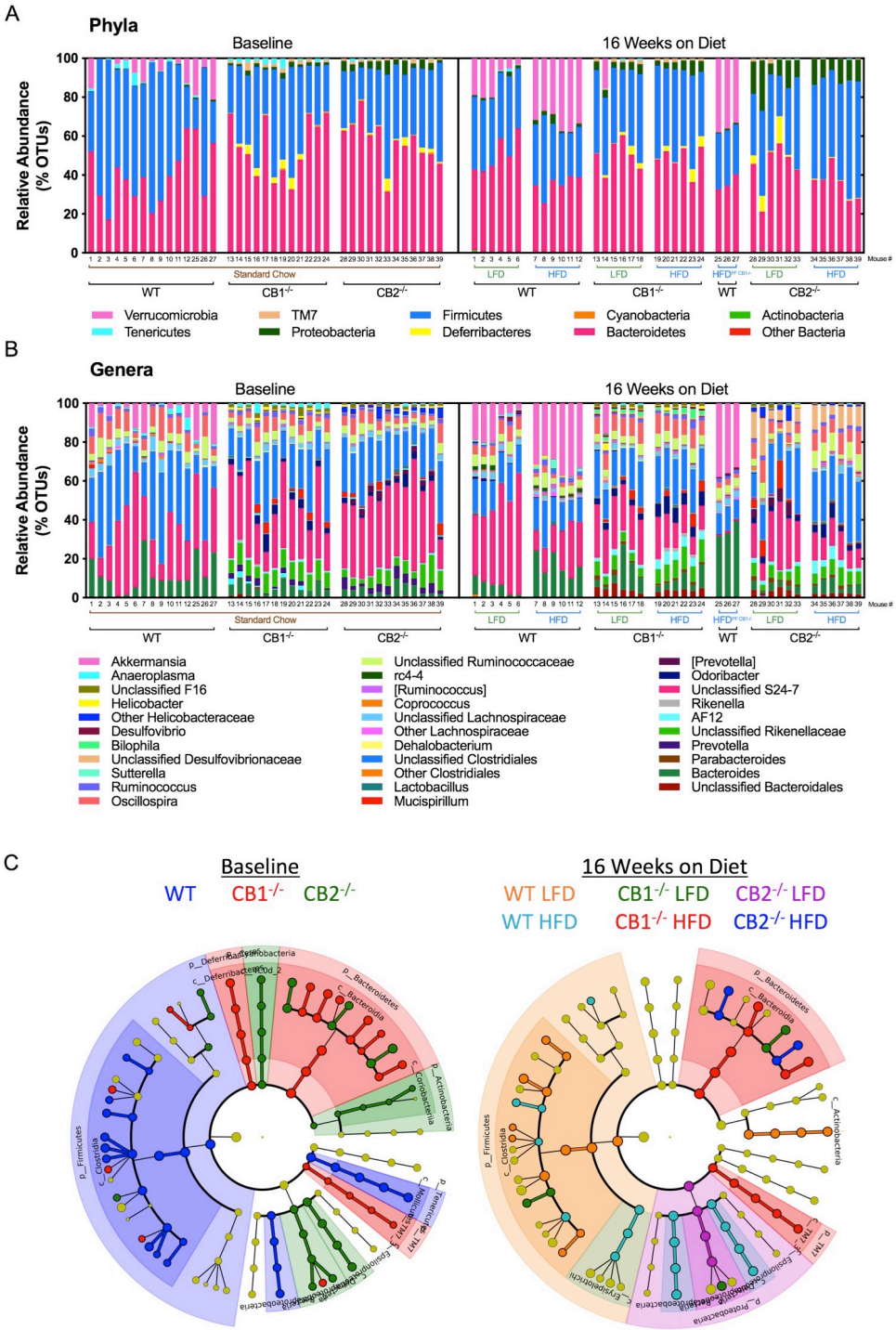

Figure 4.6 Predictive metagenomics by 16S V3-V4 rRNA gene sequencing. As described in Figure 4.5 legend, stool samples were collected pre- (Baseline) and post- 16 weeks of purified diet for 16S V3-V4 rRNA gene sequencing. (A) Phylum level abundance for each biological replicate. (B) Genus level abundance for each biological replicate. (C) LEfSe cladograms of enriched bacterial taxa. For (A-B), each bar represents one mouse's predicted microbiota at the designated time point.

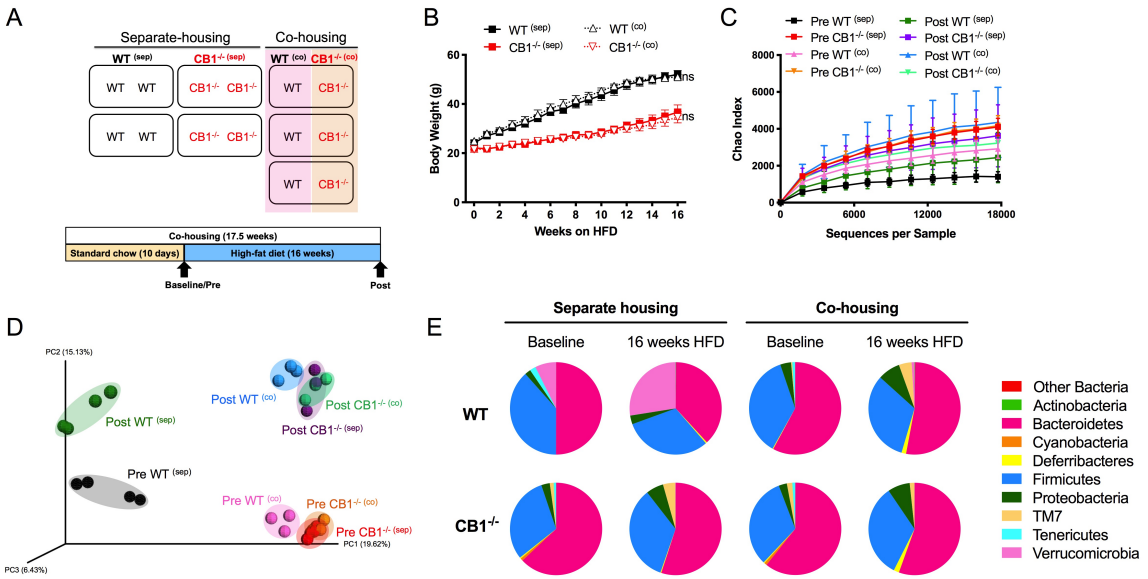

Figure 4.7 Gut microbiota composition is largely dispensable for the improved obesity phenotype observed in CB1$^{-/-}$ mice.

Male C57Bl6 WT and CB1$^{-/-}$ were placed in co-housing or standard separate housing conditions at 6-8 weeks of age and maintained on standard chow diet for 10 days before being placed on HFD for 16 weeks. Stool samples were collected after 10 days of co-housing but pre-HFD (termed “Baseline” or “Pre”) and post-16 weeks of HFD for 16S V3-V4 rRNA gene sequencing. (A) Experimental timeline and caging setup for separate- (sep) and co-housing (co). (B) Body weight growth curves. (C) Chao index alpha diversity. (D) 3D PCoA plot of unweighted UniFrac beta diversity. (E) Mean relative abundance of each bacterial phyla displayed as a pie chart per group. Data shown are mean (+/- SEM). N=3-4 mice/group. ns: not significant ($p>0.05$) between housing conditions within each genotype by one-way ANOVA.

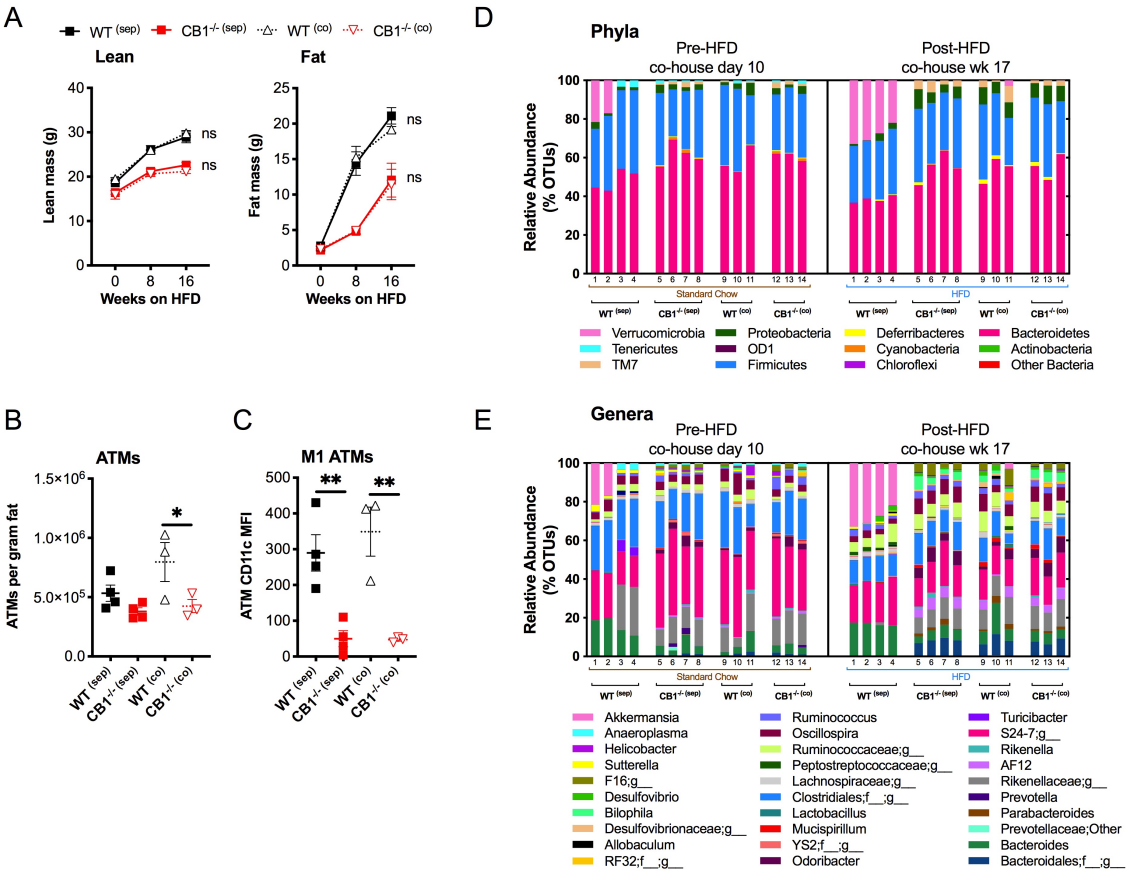

Figure 4.8 Co-housing WT and CB1$^{-/-}$ mice does not confer resistance to DIO development; however, CB1$^{-/-}$ maintain a dominant microbiota composition.

As described in Figure 4.7 legend, mice were placed in co-housing or standard separate housing conditions and challenged with HFD. (A) DEXA lean and fat mass. (B) Epididymal ATM ($CD45^+CD11b^+F4/80^+$) count per gram of fat measured by flow cytometry. (C) Epididymal ATM-gated CD11c MFI. (D) Phylum level abundance for each biological replicate. (E) Genus level abundance for each biological replicate. Data shown are mean +/- SEM. N=3-4 mice/group. ns: not significant ($p>0.05$) between housing conditions within each genotype, *$p<0.05$, **$p<0.01$ by one-way ANOVA.

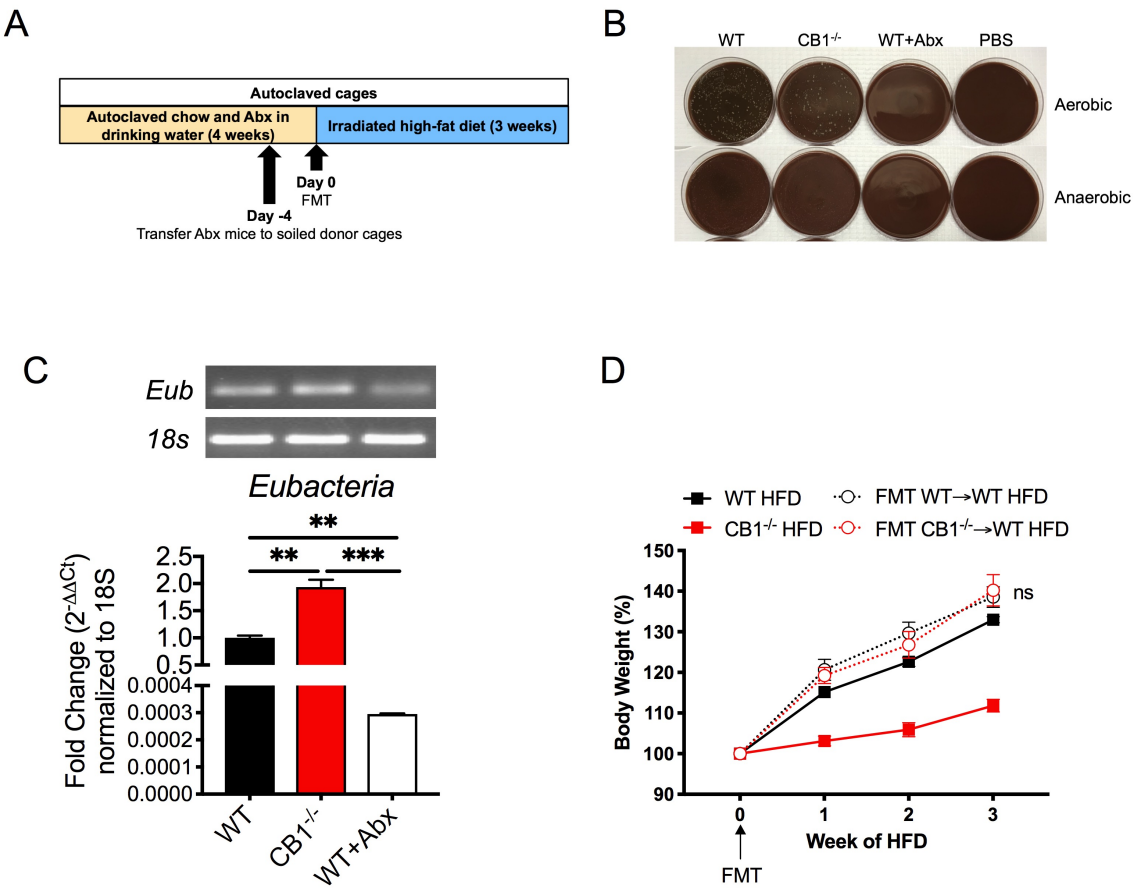

Figure 4.9 Transfer of CB1$^{-/-}$ feces does not confer resistance to DIO development.

Naïve 5-week-old male C57BL6 mice were depleted of gut microbiota by administering antibiotics ("Abx", 1mg/mL Bacitracin, 170ug/mL Gentamycin, 125ug/mL Ciprofloxacin, 100ug/mL Neomycin, 100U/mL Penicillin, 100ug/mL Metronidazole, 100ug/mL Ceftazidime, 50ug/mL Streptomycin, 50ug/mL Vancomycin) in the drinking water for 4 weeks then microbiota from naïve C57BL6 WT and CB1$^{-/-}$ mice were transferred into Abx-treated recipients. The mice were maintained in autoclaved caging and challenged with irradiated HFD after fecal microbiota transfer (FMT). (A) Abx microbiota depletion and FMT experimental timeline. (B) Microbiota depletion validation by culturing feces on chocolate agar for 24h. (C) Microbiota depletion validation by qRT-PCR for *Eubacteria (Eub)* normalizd to host *18S* genes. (D) Body weight growth curves during 3 weeks of HFD feeding. Data shown are mean +/- SEM. ns: not significant ($p>0.05$) between FMT groups by one-way ANOVA. **$p<0.01$, ***$p<0.001$ by one-way ANOVA. For WT HFD and CB1$^{-/-}$ HFD, n=2 mice/group. For FMT groups, n=6 mice/group.

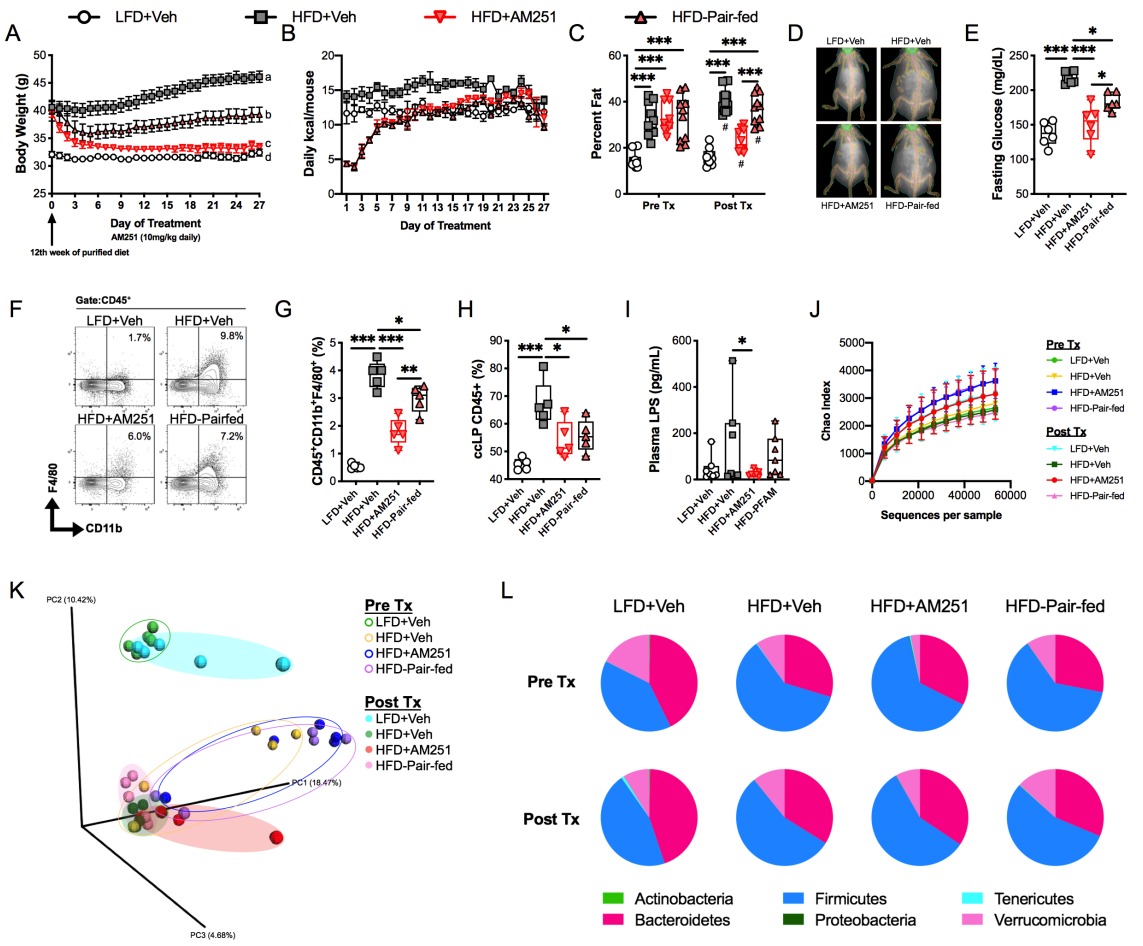

Figure 4.10 DIO intervention with the CB1 antagonist AM251 reverses obesity, inflammation, and shifts intestinal microbiota composition.
Male C57Bl6 mice were fed purified diets for 12-weeks prior to a 4 week DIO intervention with AM251. HFD-fed DIO mice were treated with AM251 (10mg/kg, o.g.) daily for 4 weeks. All other control groups were treated with vehicle (Veh). Mice were fed *ad libitum*, except the pair-fed group received the same amount of food as the HFD+AM251 group consumed daily. Stool samples were collected before and after treatment for 16s V3-V4 rRNA gene sequencing. (A) Body weight. (B) Food intake. (C) Body fat percentage Pre- and Post- treatment (Tx) measured by DEXA. (D) Representative DEXA scans. (E) Fasting blood glucose after 4 weeks of treatment. (F) Representative flow cytometry contour plots of epididymal ATMs after 4 weeks of treatment. (G) CD45+CD11b+F4/80+ ATM percentage of SVF. (H) Cecal:colonic lamina propria (ccLP) percentage of CD45+ leukocytes. (I) Plasma LPS concentration after 4 weeks of treatment. (J) Microbiota alpha diversity by Chao index. (K) Unweighted UniFrac PCoA plot of beta diversity. (L) Phylum level abundance pie charts. Data shown are mean (+/- SEM) or box and whisker plots with each point representing biological replicates. For (A and C), N=9-10 mice/group. For (B), N=3 independent experiments. For (E-L), N=4-6 mice/group*p<0.05, **p<0.01, ***p<0.001 by one-way ANOVA #P<0.05 vs. Pre Tx. For (A) p<0.05 if alphabetical characters differ between the groups being compared by one-way ANOVA.

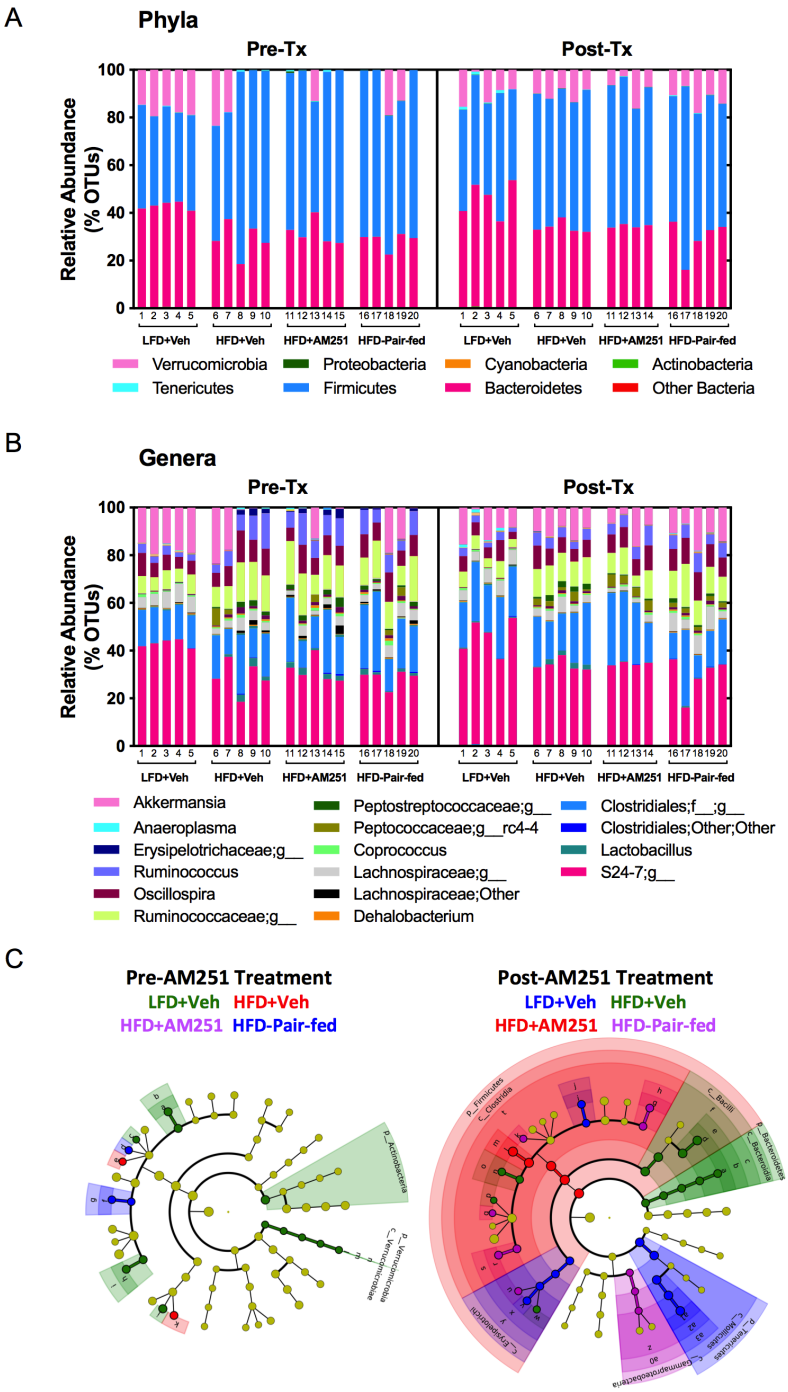

Figure 4.11 AM251 DIO intervetion predictive metagenomics by 16S V3-V4 rRNA gene sequencing.

As described in Figure 4.10 legend, stool samples were collected pre- and post-4 weeks of AM251 DIO intervention for 16S V3-V4 rRNA gene sequencing. (A) Phylum level abundance for each biological replicate. (B) Genus level abundance for each biological replicate. (C) LEfSe cladograms of enriched bacterial taxa. For (A-B), each bar represents one mouse's predicted microbiota at the designated time point.

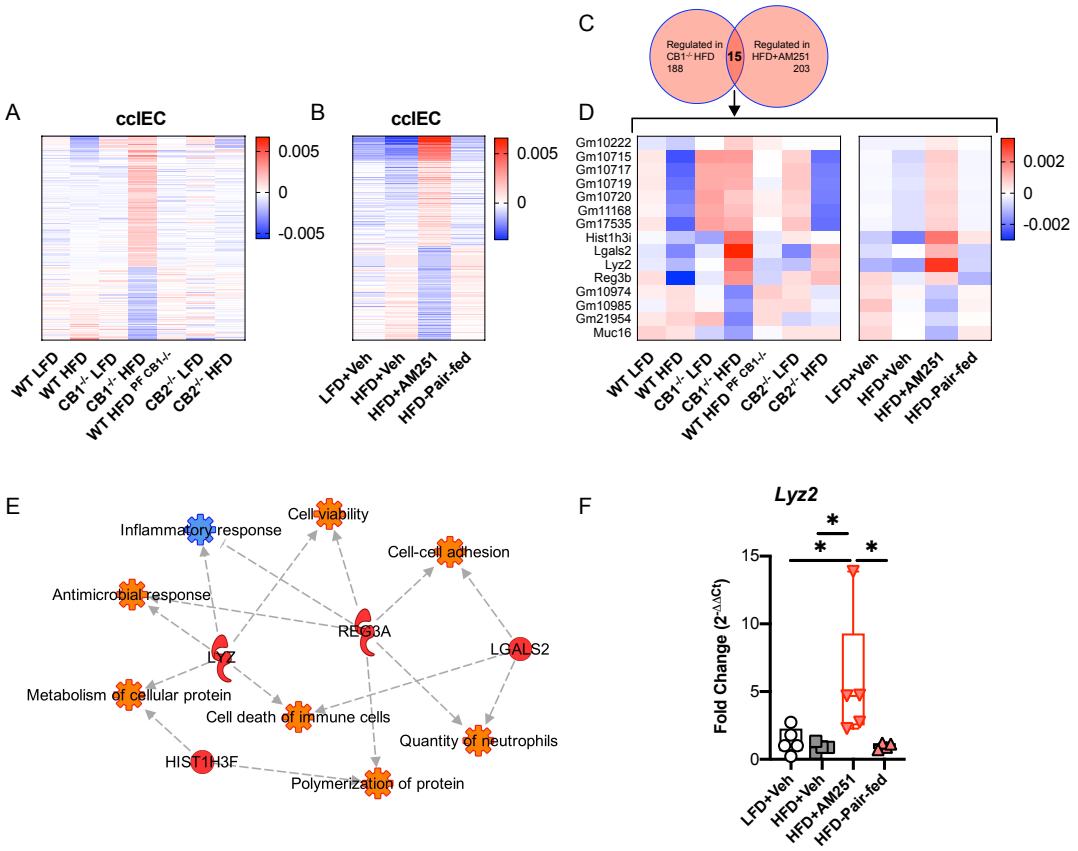

Figure 4.12 CB1 regulates microbial defense in intestinal epithelial cells. EpCAM+ IECs were isolated from ceca: colons of mice at the conclusion of the CB receptor knockout and AM251 DIO intervention studies described in Figure 4.1 and Figure 4.10 legends. (A) Heatmap of 188 differentially expressed genes in ccIEC of CB1$^{-/-}$ HFD mice versus all other HFD-fed groups. (B) Heatmap of 203 differentially expressed genes in ccIEC of HFD+AM251 mice versus all other HFD-fed groups. (C) Venn diagram comparison of similarly regulated genes in CB1$^{-/-}$ HFD and HFD+AM251 mice of each DIO model. (D) Heatmap of appetite-independent CB1 regulated genes. (E) IPA pathway analysis of differentially expressed genes in panel D. (F) qRT-PCR validation of AMPs in the AM251 DIO intervention model. *p<0.05 by one-way ANOVA.

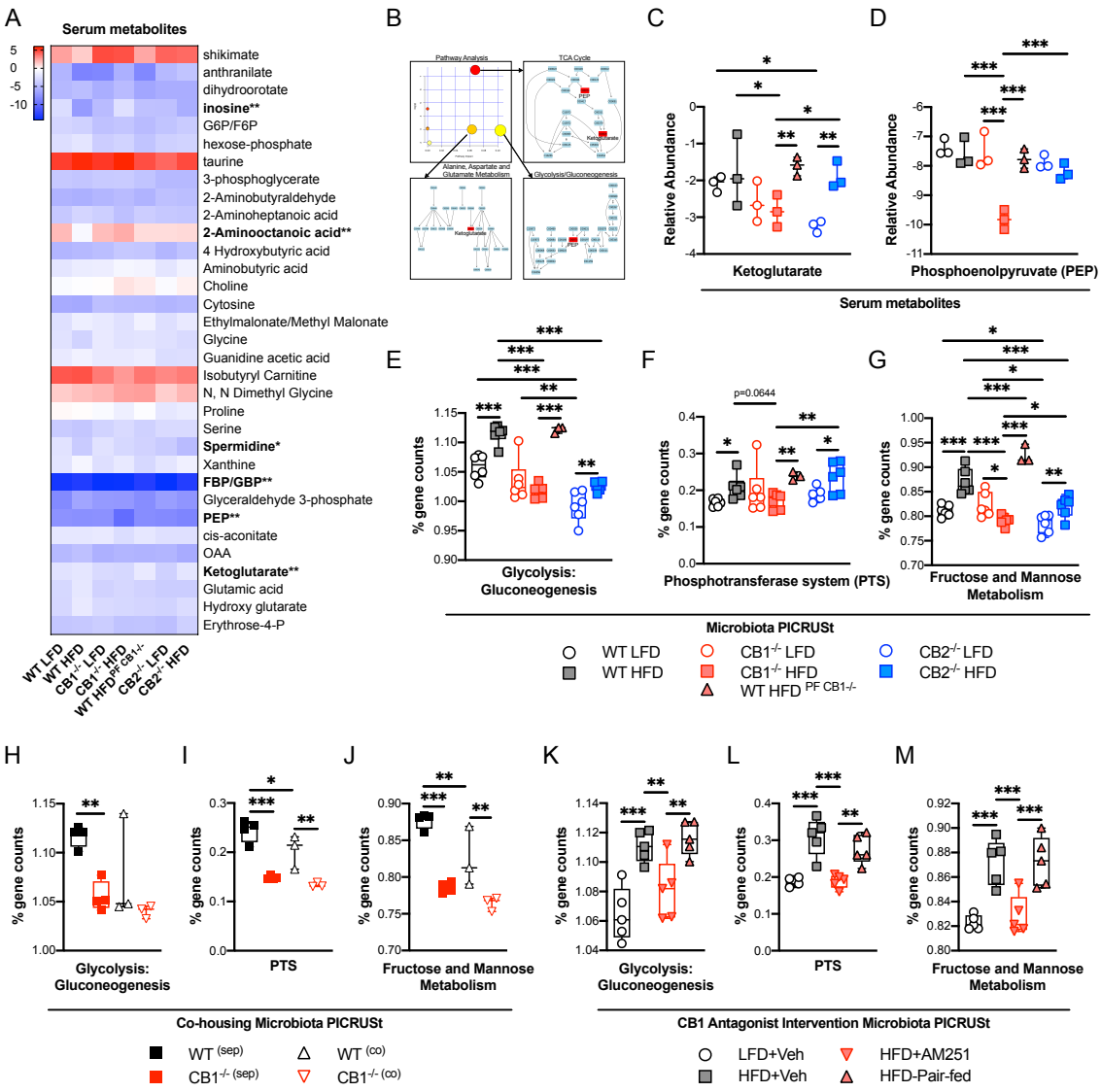

Figure 4.13 CB1 regulates host and intestinal microbiota sugar metabolism. As described in Figures 4.5, 4.7, and 4.10, stool DNA from the three DIO models (CB receptor knockout, co-housing, and AM251 intervention) were used for 16S predictive metagenomics. Serum TCA cycle targeted metabolomics were performed on fasting serum samples from the CB receptor knockout model only. PICRUSt analyses were performed on 16S sequencing data for all three models. (A) Heatmap of serum metabolites differentially expressed in $CB1^{-/-}$ HFD versus at least one other HFD-fed group. Metabolites in **bold*** indicates ANOVA $p<0.05$ in $CB1^{-/-}$ HFD versus both WT HFD and $CB2^{-/-}$ HFD. Metabolites in **bold** ** indicates ANOVA $p<0.05$ in $CB1^{-/-}$ HFD versus all three HFD-fed groups (WT HFD, WT $HFD^{PF\ CB1-/-}$, and $CB2^{-/-}$ HFD). (B) MetaboAnalyst pathway analysis of metabolic pathways affected by the bold metabolites in panel A. (C) Relative abundance of ketoglutarate versus internal control in fasting serum. (D) Relative abundance of phosphoenolpyruvate (PEP) versus internal control in fasting serum. (E, H, K) 16s % gene counts relating to bacterial glycolysis:

gluconeogenesis pathways by PICRUSt analysis. (F, I, L) 16s % gene counts relating to phosphotransferase system processes (PTS) by PICRUSt analysis. (G, J, M) Gut microbial % gene counts relating to fructose and mannose metabolism by PICRUSt analysis. Data shown are mean or box and whisker plots with each point representing biological replicates. N=3-6 mice/group. *p<0.05, **p<0.01, ***p,0.001 by one-way ANOVA.

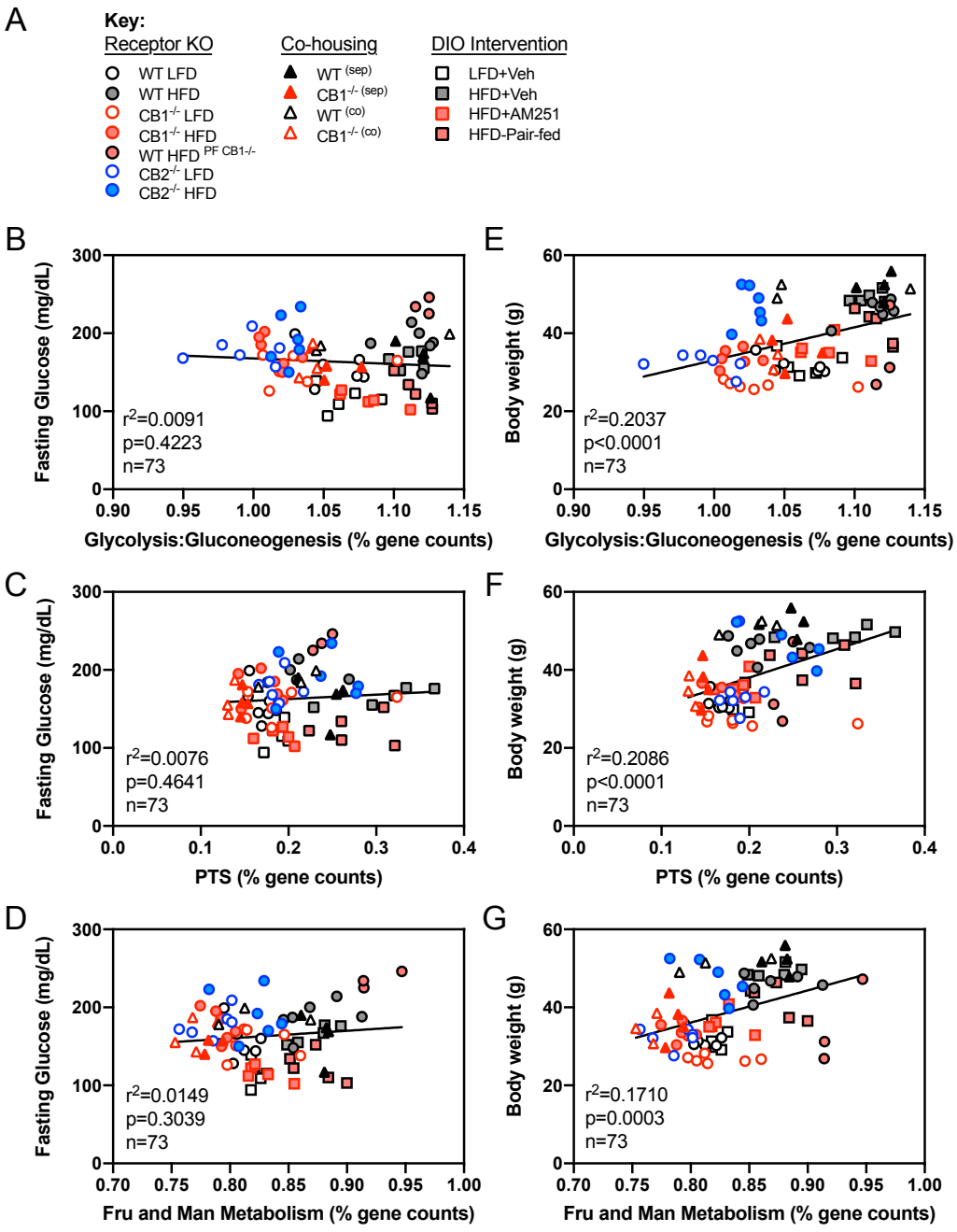

Figure 4.14 Microbiota sugar metabolic pathways correlate with body weight gain.

As described and shown in Figure 4.13, PICRUSt predictions for microbial pathways relating to sugar metabolism were downregulated with CB1 knockout (KO) or knockdown. Linear regression analyses were performed to correlate the metabolic pathways with host fasting glucose concentration and endpoint body weight. (A) Key for groups displayed in B-G. (B-D) Correlation of microbial pathways with fasting blood glucose. (E-G) Correlation of microbial pathways with body weight. Represented are data points for individual mice.

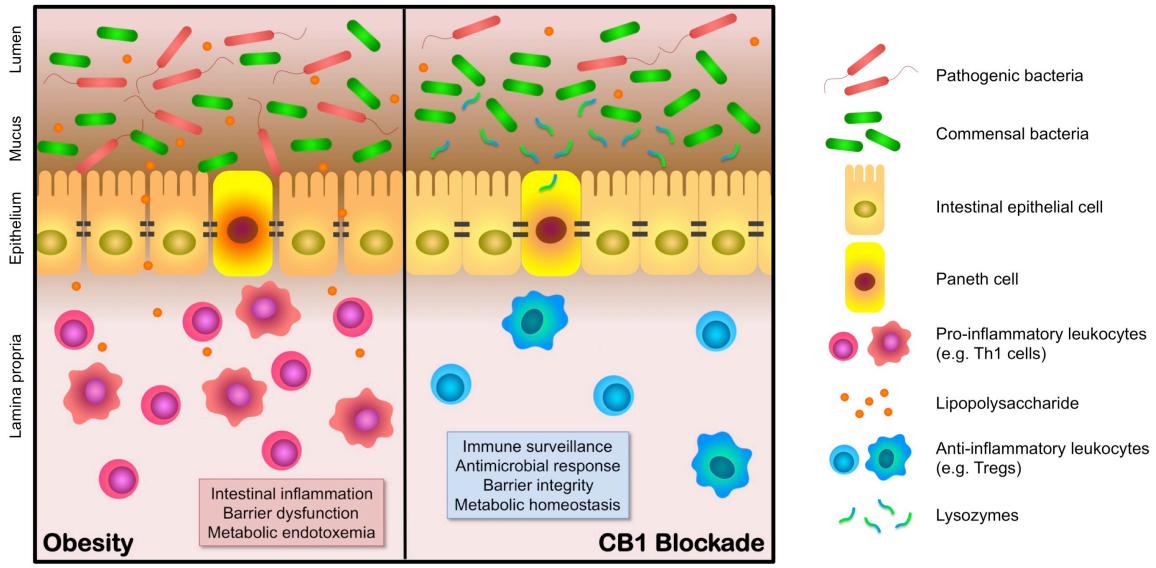

Figure 4.15 CB1 blockade improves DIO-induced intestinal dysbiosis. During obesity, gut microbial dysbiosis promotes intestinal permeability, inflammation, barrier dysfunction, and metabolic endotoxemia. CB1 blockade improves barrier integrity due to antimicrobial response and production of antimicrobial peptides such as Lysozyme 2 by Paneth cells. Immune surveillance and metabolic homeostasis is maintained.

CHAPTER 5

CONCLUSION

In this dissertation, mechanisms involved in ECS regulation of obesity-induced inflammation were investigated, and included epigenetic regulation of ATMs, as well as gut microbiota: host interactions.

We first characterized miRNA expression profiles of ATMs isolated from lean and HFD-induced obese mice. Increased ECS activation and ATM inflammation is observed in obesity, yet miRNA expression profiles of ATMs were not yet established. Interestingly, downregulation of the miR-30 family led to induction of DLL4-Notch signaling-induced ATM M1 polarization and pro-inflammatory cytokine production. Furthermore, miR-30 expression was at least in part regulated by DNA methylation. This study identified miR-30 as a potential therapeutic modality for the treatment of obesity and prevention of associated metabolic impairments.

Secondly, we used a DIO intervention model whereby obese mice were treated with the CB1 antagonist AM251. Investigation of miRNA profiles in ATMs revealed that expression of miR-30e-5p was upregulated following CB1 blockade, independent of reduced calorie intake. Subsequently, DLL4-Notch signaling-induced ATM M1 polarization was reduced. In addition, other DLL4-Notch signaling-associated parameters were altered as a result of CB1 blockade.

These included a reduction in adipocyte size, decreased inflammatory cytokine/chemokine expression in ATMs, and a reduced Th1 inflammatory response. Furthermore, AM251 treatment of macrophages suppressed their capability to promote a Th1 response through regulation of DLL4. This study demonstrated that upregulation of miR-30e-5p in ATMs following CB1 blockade has anti-inflammatory and anti-obesity effects, which further support the therapeutic potential of this miRNA for obesity treatment.

Lastly, we investigated gut microbiota and intestinal immunity during DIO in mice lacking functional cannabinoid receptors as well as in AM251-treated DIO mice. Markedly, we found that resistance to DIO development in $CB1^{-/-}$ mice coincided with resistance to alterations in the gut microbiome. $CB2^{-/-}$ mice also experienced accelerated obesity development and elevated abundance of pathogenic bacteria in their gut microbiomes versus wild-type controls. We further investigated the beneficial effects of $CB1^{-/-}$ microbiota by performing co-housing and fecal microbiota transfer and found that the composition of microbes was largely dispensable for improved obesity phenotype, yet some rare microbes remained differentially expressed after co-housing. This led to the conclusion that $CB1^{-/-}$ mice have a dominant microbiome that is firmly established, which may contribute to metabolic homeostasis. DIO mice treated with AM251 experienced a shift in microbiota profile similar to lean mice. Further investigation of interactions between host and gut microbiota revealed that CB1 regulates antimicrobial peptide production in intestinal epithelial cells. Furthermore, CB1 regulated sugar metabolic pathways in microbiota that correlate with body weight

gain. This study identified novel pathways regulated by CB1 that are involved in intestinal immunity and gut microbiota-mediated metabolic health. This study also provided insight into the detrimental effects of impaired CB2 signaling that should be further investigated.

REFERENCES

Alexander, R., Lodish, H., and Sun, L. (2011). MicroRNAs in adipogenesis and as therapeutic targets for obesity. Expert Opin Ther Targets *15*, 623–636.

Alhamoruni, A., Lee, A.C., Wright, K.L., Larvin, M., and O'Sullivan, S.E. (2010). Pharmacological effects of cannabinoids on the Caco-2 cell culture model of intestinal permeability. J. Pharmacol. Exp. Ther. *335*, 92–102.

Allison, D.B., Downey, M., Atkinson, R.L., Billington, C.J., Bray, G.A., Eckel, R.H., Finkelstein, E.A., Jensen, M.D., and Tremblay, A. (2008). Obesity as a disease: a white paper on evidence and arguments commissioned by the Council of the Obesity Society. Obesity (Silver Spring) *16*, 1161–1177.

Amara, C.S., Ambati, C.R., Vantaku, V., Badrajee Piyarathna, D.W., Donepudi, S.R., Ravi, S.S., Arnold, J.M., Putluri, V., Chatta, G., Guru, K.A., et al. (2019). Serum Metabolic Profiling Identified a Distinct Metabolic Signature in Bladder Cancer Smokers: A Key Metabolic Enzyme Associated with Patient Survival. Cancer Epidemiol. Biomarkers Prev. *28*, 770–781.

Azua, I.R. de, Mancini, G., Srivastava, R.K., Rey, A.A., Cardinal, P., Tedesco, L., Zingaretti, C.M., Sassmann, A., Quarta, C., Schwitter, C., et al. (2017). Adipocyte cannabinoid receptor CB1 regulates energy homeostasis and alternatively activated macrophages. J Clin Invest *127*, 4148–4162.

Bäckhed, F., Ding, H., Wang, T., Hooper, L.V., Koh, G.Y., Nagy, A., Semenkovich, C.F., and Gordon, J.I. (2004). The gut microbiota as an environmental factor that regulates fat storage. PNAS *101*, 15718–15723.

Bäckhed, F., Manchester, J.K., Semenkovich, C.F., and Gordon, J.I. (2007). Mechanisms underlying the resistance to diet-induced obesity in germ-free mice. Proc. Natl. Acad. Sci. U.S.A. *104*, 979–984.

Bajzer, M., Olivieri, M., Haas, M.K., Pfluger, P.T., Magrisso, I.J., Foster, M.T., Tschöp, M.H., Krawczewski-Carhuatanta, K.A., Cota, D., and Obici, S. (2011). Cannabinoid receptor 1 (CB1) antagonism enhances glucose utilisation and activates brown adipose tissue in diet-induced obese mice. Diabetologia *54*, 3121–3131.

Balsevich, G., Sticht, M., Bowles, N.P., Singh, A., Lee, T.T.Y., Li, Z., Chelikani, P.K., Lee, F.S., Borgland, S.L., Hillard, C.J., et al. (2018). Role for fatty acid amide hydrolase (FAAH) in the leptin-mediated effects on feeding and energy balance. PNAS *115*, 7605–7610.

Bam, M., Yang, X., Zhou, J., Ginsberg, J.P., Leyden, Q., Nagarkatti, P.S., and Nagarkatti, M. (2015). Evidence for Epigenetic Regulation of Pro-Inflammatory Cytokines, Interleukin-12 and Interferon Gamma, in Peripheral Blood Mononuclear Cells from PTSD Patients. J Neuroimmune Pharmacol *11*, 168–181.

Bam, M., Yang, X., Zumbrun, E.E., Zhong, Y., Zhou, J., Ginsberg, J.P., Leyden, Q., Zhang, J., Nagarkatti, P.S., and Nagarkatti, M. (2016). Dysregulated immune system networks in war veterans with PTSD is an outcome of altered miRNA expression and DNA methylation. Sci Rep *6*, 31209.

Bartel, D.P. (2004). MicroRNAs: genomics, biogenesis, mechanism, and function. Cell *116*, 281–297.

Baxter, N.T., Schmidt, A.W., Venkataraman, A., Kim, K.S., Waldron, C., and Schmidt, T.M. (2019). Dynamics of Human Gut Microbiota and Short-Chain Fatty Acids in Response to Dietary Interventions with Three Fermentable Fibers. MBio *10*, e02566-18.

Bi, P., and Kuang, S. (2015). Notch signaling as a novel regulator of metabolism. Trends Endocrinol. Metab. *26*, 248–255.

Bi, P., Shan, T., Liu, W., Yue, F., Yang, X., Liang, X.-R., Wang, J., Li, J., Carlesso, N., Liu, X., et al. (2014). Inhibition of Notch signaling promotes browning of white adipose tissue and ameliorates obesity. Nat Med *20*, 911–918.

Blanton, L.V., Charbonneau, M.R., Salih, T., Barratt, M.J., Venkatesh, S., Ilkaveya, O., Subramanian, S., Manary, M.J., Trehan, I., Jorgensen, J.M., et al. (2016). Gut bacteria that prevent growth impairments transmitted by microbiota from malnourished children. Science *351*, aad3311.

Borggrefe, T., and Liefke, R. (2012). Fine-tuning of the intracellular canonical Notch signaling pathway. Cell Cycle *11*, 264–276.

Boutens, L., and Stienstra, R. (2016). Adipose tissue macrophages: going off track during obesity. Diabetologia *59*, 879–894.

Bridge, G., Monteiro, R., Henderson, S., Emuss, V., Lagos, D., Georgopoulou, D., Patient, R., and Boshoff, C. (2012). The microRNA-30 family targets *DLL4* to modulate endothelial cell behavior during angiogenesis. Blood *120*, 5063–5072.

Brown, W.H., Gillum, M.P., Lee, H.-Y., Camporez, J.P.G., Zhang, X. -m., Jeong, J.K., Alves, T.C., Erion, D.M., Guigni, B.A., Kahn, M., et al. (2012). Fatty acid amide hydrolase ablation promotes ectopic lipid storage and insulin resistance due to centrally mediated hypothyroidism. Proceedings of the National Academy of Sciences *109*, 14966–14971.

Busbee, P.B., Nagarkatti, M., and Nagarkatti, P.S. (2015). Natural Indoles, Indole-3-Carbinol (I3C) and 3,3'-Diindolylmethane (DIM), Attenuate Staphylococcal Enterotoxin B-Mediated Liver Injury by Downregulating miR-31 Expression and Promoting Caspase-2-Mediated Apoptosis. PLOS ONE *10*, e0118506.

Caiafa, P., and Zampieri, M. (2005). DNA methylation and chromatin structure: the puzzling CpG islands. J. Cell. Biochem. *94*, 257–265.

Campbell, C., Dikiy, S., Bhattarai, S.K., Chinen, T., Matheis, F., Calafiore, M., Hoyos, B., Hanash, A., Mucida, D., Bucci, V., et al. (2018). Extrathymically Generated Regulatory T Cells Establish a Niche for Intestinal Border-Dwelling Bacteria and Affect Physiologic Metabolite Balance. Immunity *48*, 1245-1257.e9.

Cani, P.D. (2014). Metabolism in 2013: The gut microbiota manages host metabolism. Nat Rev Endocrinol *10*, 74–76.

Cani, P.D., Amar, J., Iglesias, M.A., Poggi, M., Knauf, C., Bastelica, D., Neyrinck, A.M., Fava, F., Tuohy, K.M., Chabo, C., et al. (2007). Metabolic Endotoxemia Initiates Obesity and Insulin Resistance. Diabetes *56*, 1761–1772.

Cani, P.D., Bibiloni, R., Knauf, C., Waget, A., Neyrinck, A.M., Delzenne, N.M., and Burcelin, R. (2008). Changes in gut microbiota control metabolic endotoxemia-induced inflammation in high-fat diet-induced obesity and diabetes in mice. Diabetes *57*, 1470–1481.

Cani, P.D., Plovier, H., Van Hul, M., Geurts, L., Delzenne, N.M., Druart, C., and Everard, A. (2016). Endocannabinoids--at the crossroads between the gut microbiota and host metabolism. Nat Rev Endocrinol *12*, 133–143.

Chassaing, B., Koren, O., Goodrich, J.K., Poole, A.C., Srinivasan, S., Ley, R.E., and Gewirtz, A.T. (2015). Dietary emulsifiers impact the mouse gut microbiota promoting colitis and metabolic syndrome. Nature *519*, 92–96.

Chevalier, S., Burgess, S.C., Malloy, C.R., Gougeon, R., Marliss, E.B., and Morais, J.A. (2006). The greater contribution of gluconeogenesis to glucose production in obesity is related to increased whole-body protein catabolism. Diabetes *55*, 675–681.

Cota, D., Marsicano, G., Tschöp, M., Grübler, Y., Flachskamm, C., Schubert, M., Auer, D., Yassouridis, A., Thöne-Reineke, C., Ortmann, S., et al. (2003). The endogenous cannabinoid system affects energy balance via central orexigenic drive and peripheral lipogenesis. J. Clin. Invest. *112*, 423–431.

D'Ambrosio, A., Cossu, A., Amendola, A., Zandri, A., Butera, A., Sanchez, M., Biffoni, M., Pronio, A., Montesani, C., Kohn, A., et al. (2016). Lamina Propria CD4+LAP+ Regulatory T Cells Are Increased in Active Ulcerative Colitis but Show Increased IL-17 Expression and Reduced Suppressor Activity. J Crohns Colitis *10*, 346–353.

Di Marzo, V., Goparaju, S.K., Wang, L., Liu, J., Bátkai, S., Járai, Z., Fezza, F., Miura, G.I., Palmiter, R.D., Sugiura, T., et al. (2001). Leptin-regulated endocannabinoids are involved in maintaining food intake. Nature *410*, 822–825.

Dong, C., Yoon, W., and Goldschmidt-Clermont, P.J. (2002). DNA methylation and atherosclerosis. J. Nutr. *132*, 2406S-2409S.

Dong, Z., Gong, H., Chen, Y., Wu, H., Wu, J., Deng, Y., and Song, X. (2018). LH-21, A Peripheral Cannabinoid Receptor 1 Antagonist, Exerts Favorable

Metabolic Modulation Including Antihypertensive Effect in KKAy Mice by Regulating Inflammatory Cytokines and Adipokines on Adipose Tissue. Front Endocrinol (Lausanne) *9*, 167.

Dopkins, N., Nagarkatti, P.S., and Nagarkatti, M. (2018). The role of gut microbiome and associated metabolome in the regulation of neuroinflammation in multiple sclerosis and its implications in attenuating chronic inflammation in other inflammatory and autoimmune disorders. Immunology.

Edgar, R.C., Haas, B.J., Clemente, J.C., Quince, C., and Knight, R. (2011). UCHIME improves sensitivity and speed of chimera detection. Bioinformatics *27*, 2194–2200.

Engeli, S., Böhnke, J., Feldpausch, M., Gorzelniak, K., Janke, J., Bátkai, S., Pacher, P., Harvey-White, J., Luft, F.C., Sharma, A.M., et al. (2005). Activation of the Peripheral Endocannabinoid System in Human Obesity. Diabetes *54*, 2838–2843.

Everard, A., Belzer, C., Geurts, L., Ouwerkerk, J.P., Druart, C., Bindels, L.B., Guiot, Y., Derrien, M., Muccioli, G.G., Delzenne, N.M., et al. (2013). Cross-talk between Akkermansia muciniphila and intestinal epithelium controls diet-induced obesity. Proc. Natl. Acad. Sci. U.S.A. *110*, 9066–9071.

Fontana, L., Eagon, J.C., Trujillo, M.E., Scherer, P.E., and Klein, S. (2007). Visceral Fat Adipokine Secretion Is Associated With Systemic Inflammation in Obese Humans. Diabetes *56*, 1010–1013.

Forde, B.M., and O'Toole, P.W. (2013). Next-generation sequencing technologies and their impact on microbial genomics. Brief Funct Genomics *12*, 440–453.

Freese, N.H., Norris, D.C., and Loraine, A.E. (2016). Integrated genome browser: visual analytics platform for genomics. Bioinformatics *32*, 2089–2095.

Fujisaka, S., Usui, I., Bukhari, A., Ikutani, M., Oya, T., Kanatani, Y., Tsuneyama, K., Nagai, Y., Takatsu, K., Urakaze, M., et al. (2009). Regulatory Mechanisms for Adipose Tissue M1 and M2 Macrophages in Diet-Induced Obese Mice. Diabetes *58*, 2574–2582.

Fukuda, D., and Aikawa, M. (2013). Expanding role of delta-like 4 mediated notch signaling in cardiovascular and metabolic diseases. Circ. J. *77*, 2462–2468.

Fukuda, D., Aikawa, E., Swirski, F.K., Novobrantseva, T.I., Kotelianski, V., Gorgun, C.Z., Chudnovskiy, A., Yamazaki, H., Croce, K., Weissleder, R., et al. (2012). Notch ligand delta-like 4 blockade attenuates atherosclerosis and metabolic disorders. Proc. Natl. Acad. Sci. U.S.A. *109*, E1868-1877.

Fung, E., Tang, S.-M.T., Canner, J.P., Morishige, K., Arboleda-Velasquez, J.F., Cardoso, A.A., Carlesso, N., Aster, J.C., and Aikawa, M. (2007). Delta-

Like 4 Induces Notch Signaling in Macrophages. Circulation *115*, 2948–2956.

Furusawa, Y., Obata, Y., Fukuda, S., Endo, T.A., Nakato, G., Takahashi, D., Nakanishi, Y., Uetake, C., Kato, K., Kato, T., et al. (2013). Commensal microbe-derived butyrate induces the differentiation of colonic regulatory T cells. Nature *504*, 446–450.

Ge, Q., Brichard, S., Yi, X., and Li, Q. (2014). microRNAs as a New Mechanism Regulating Adipose Tissue Inflammation in Obesity and as a Novel Therapeutic Strategy in the Metabolic Syndrome. J Immunol Res *2014*.

Guan, H., Singh, U.P., Rao, R., Mrelashvili, D., Sen, S., Hao, H., Zumbrun, E.E., Singh, N.P., Nagarkatti, P.S., and Nagarkatti, M. (2016). Inverse correlation of expression of microRNA-140-5p with progression of multiple sclerosis and differentiation of encephalitogenic T helper type 1 cells. Immunology *147*, 488–498.

Guo, X., Li, J., Tang, R., Zhang, G., Zeng, H., Wood, R.J., and Liu, Z. (2017). High Fat Diet Alters Gut Microbiota and the Expression of Paneth Cell-Antimicrobial Peptides Preceding Changes of Circulating Inflammatory Cytokines.

Gupta, S., Allen-Vercoe, E., and Petrof, E.O. (2016). Fecal microbiota transplantation: in perspective. Therap Adv Gastroenterol *9*, 229–239.

Hamilton, T.A., Zhao, C., Pavicic, P.G., and Datta, S. (2014). Myeloid colony-stimulating factors as regulators of macrophage polarization. Front. Immunol. *5*, 554.

Han, J.H., Shin, H., Rho, J.G., Kim, J.-E., Son, D.H., Yoon, J., Lee, Y.J., Park, J.-H., Song, B.J., Choi, C.-S., et al. (2018). Peripheral cannabinoid 1 receptor blockade mitigates adipose tissue inflammation via NLRP3 inflammasome in mouse models of obesity. Diabetes Obes Metab.

Haslam, D.W., and James, W.P.T. (2005). Obesity. The Lancet *366*, 1197–1209.

Herp, S., Brugiroux, S., Garzetti, D., Ring, D., Jochum, L.M., Beutler, M., Eberl, C., Hussain, S., Walter, S., Gerlach, R.G., et al. (2019). Mucispirillum schaedleri Antagonizes Salmonella Virulence to Protect Mice against Colitis. Cell Host Microbe *25*, 681-694.e8.

Hodin, C.M., Verdam, F.J., Grootjans, J., Rensen, S.S., Verheyen, F.K., Dejong, C.H.C., Buurman, W.A., Greve, J.W., and Lenaerts, K. (2011). Reduced Paneth cell antimicrobial protein levels correlate with activation of the unfolded protein response in the gut of obese individuals. J. Pathol. *225*, 276–284.

Hou, Y.-P., He, Q.-Q., Ouyang, H.-M., Peng, H.-S., Wang, Q., Li, J., Lv, X.-F., Zheng, Y.-N., Li, S.-C., Liu, H.-L., et al. (2017). Human Gut Microbiota Associated with Obesity in Chinese Children and Adolescents. Biomed Res Int *2017*.

Hu, F., Wang, M., Xiao, T., Yin, B., He, L., Meng, W., Dong, M., and Liu, F. (2015). miR-30 Promotes Thermogenesis and the Development of Beige Fat by Targeting RIP140. Diabetes *64*, 2056–2068.

Irani, S., Pan, X., Peck, B.C.E., Iqbal, J., Sethupathy, P., and Hussain, M.M. (2016). MicroRNA-30c Mimic Mitigates Hypercholesterolemia and Atherosclerosis in Mice. J. Biol. Chem. *291*, 18397–18409.

Ishiguro, H., Carpio, O., Horiuchi, Y., Shu, A., Higuchi, S., Schanz, N., Benno, R., Arinami, T., and Onaivi, E.S. (2010). A nonsynonymous polymorphism in cannabinoid CB2 receptor gene is associated with eating disorders in humans and food intake is modified in mice by its ligands. Synapse *64*, 92–96.

Izzo, A.A., Fezza, F., Capasso, R., Bisogno, T., Pinto, L., Iuvone, T., Esposito, G., Mascolo, N., Di Marzo, V., and Capasso, F. (2001). Cannabinoid CB1-receptor mediated regulation of gastrointestinal motility in mice in a model of intestinal inflammation. Br J Pharmacol *134*, 563–570.

Jin, B., and Robertson, K.D. (2013). DNA Methyltransferases (DNMTs), DNA Damage Repair, and Cancer. Adv Exp Med Biol *754*, 3–29.

Kent, W.J., Sugnet, C.W., Furey, T.S., Roskin, K.M., Pringle, T.H., Zahler, A.M., and Haussler, D. (2002). The human genome browser at UCSC. Genome Res. *12*, 996–1006.

Klöting, N., Berthold, S., Kovacs, P., Schön, M.R., Fasshauer, M., Ruschke, K., Stumvoll, M., and Blüher, M. (2009). MicroRNA expression in human omental and subcutaneous adipose tissue. PLoS ONE *4*, e4699.

Kyle, T.K., Dhurandhar, E.J., and Allison, D.B. (2016). Regarding Obesity as a Disease: Evolving Policies and Their Implications. Endocrinol Metab Clin North Am *45*, 511–520.

Lackey, D.E., and Olefsky, J.M. (2016). Regulation of metabolism by the innate immune system. Nature Reviews Endocrinology *12*, 15–28.

Langille, M.G.I., Zaneveld, J., Caporaso, J.G., McDonald, D., Knights, D., Reyes, J.A., Clemente, J.C., Burkepile, D.E., Vega Thurber, R.L., Knight, R., et al. (2013). Predictive functional profiling of microbial communities using 16S rRNA marker gene sequences. Nat. Biotechnol. *31*, 814–821.

Laprairie, R., Kelly, M., and Denovan-Wright, E. (2012). The dynamic nature of type 1 cannabinoid receptor (CB1) gene transcription. Br J Pharmacol *167*, 1583–1595.

Lewis, B.P., Burge, C.B., and Bartel, D.P. (2005). Conserved seed pairing, often flanked by adenosines, indicates that thousands of human genes are microRNA targets. Cell *120*, 15–20.

Ley, R.E., Bäckhed, F., Turnbaugh, P., Lozupone, C.A., Knight, R.D., and Gordon, J.I. (2005). Obesity alters gut microbial ecology. PNAS *102*, 11070–11075.

Li, G., Xie, C., Lu, S., Nichols, R.G., Tian, Y., Li, L., Patel, D., Ma, Y., Brocker, C.N., Yan, T., et al. (2017). Intermittent Fasting Promotes White Adipose Browning and Decreases Obesity by Shaping the Gut Microbiota. Cell Metabolism *26*, 672-685.e4.

Liao, X., Sharma, N., Kapadia, F., Zhou, G., Lu, Y., Hong, H., Paruchuri, K., Mahabeleshwar, G.H., Dalmas, E., Venteclef, N., et al. (2011). Krüppel-like factor 4 regulates macrophage polarization. J. Clin. Invest. *121*, 2736–2749.

Lienhard, M., Grimm, C., Morkel, M., Herwig, R., and Chavez, L. (2014). MEDIPS: genome-wide differential coverage analysis of sequencing data derived from DNA enrichment experiments. Bioinformatics *30*, 284–286.

Liu, R., Hong, J., Xu, X., Feng, Q., Zhang, D., Gu, Y., Shi, J., Zhao, S., Liu, W., Wang, X., et al. (2017). Gut microbiome and serum metabolome alterations in obesity and after weight-loss intervention. Nature Medicine *23*, 859.

Lombard, C., Nagarkatti, M., and Nagarkatti, P. (2007). CB2 cannabinoid receptor agonist, JWH-015 triggers apoptosis in immune cells: Potential role for CB2 selective ligands as immunosuppressive agents. Clin Immunol *122*, 259–270.

de Luis, D.A., Mulero, I., Primo, D., Izaola, O., and Aller, R. (2018). Effects of polymorphism rs3123554 in the cannabinoid receptor gene type 2 (CB2R)

on metabolic and adiposity parameters after weight loss with two hypocaloric diets. Diabetes Res. Clin. Pract. *139*, 339–347.

Lumeng, C.N., Bodzin, J.L., and Saltiel, A.R. (2007). Obesity induces a phenotypic switch in adipose tissue macrophage polarization. J. Clin. Invest. *117*, 175–184.

Maccarrone, M., Bab, I., Bíró, T., Cabral, G.A., Dey, S.K., Di Marzo, V., Konje, J.C., Kunos, G., Mechoulam, R., Pacher, P., et al. (2015). Endocannabinoid signaling at the periphery: 50 years after THC. Trends in Pharmacological Sciences *36*, 277–296.

Mahowald, M.A., Rey, F.E., Seedorf, H., Turnbaugh, P.J., Fulton, R.S., Wollam, A., Shah, N., Wang, C., Magrini, V., Wilson, R.K., et al. (2009). Characterizing a model human gut microbiota composed of members of its two dominant bacterial phyla. PNAS *106*, 5859–5864.

Mantovani, A., Sozzani, S., Locati, M., Allavena, P., and Sica, A. (2002). Macrophage polarization: tumor-associated macrophages as a paradigm for polarized M2 mononuclear phagocytes. Trends Immunol. *23*, 549–555.

Matthews, D.R., Hosker, J.P., Rudenski, A.S., Naylor, B.A., Treacher, D.F., and Turner, R.C. (1985). Homeostasis model assessment: insulin resistance and beta-cell function from fasting plasma glucose and insulin concentrations in man. Diabetologia *28*, 412–419.

Mehrpouya-Bahrami, P., Chitrala, K.N., Ganewatta, M.S., Tang, C., Murphy, E.A., Enos, R.T., Velazquez, K.T., McCellan, J., Nagarkatti, M., and Nagarkatti, P. (2017). Blockade of CB1 cannabinoid receptor alters gut microbiota and attenuates inflammation and diet-induced obesity. Scientific Reports *7*, 15645.

Mehrpouya-Bahrami, P., Miranda, K., Singh, N.P., Zumbrun, E.E., Nagarkatti, M., and Nagarkatti, P.S. (2019). Role of microRNA in CB1 antagonist-mediated regulation of adipose tissue macrophage polarization and chemotaxis during diet-induced obesity. J. Biol. Chem. *294*, 7669–7681.

Méndez-Salazar, E.O., Ortiz-López, M.G., Granados-Silvestre, M. de los Á., Palacios-González, B., and Menjivar, M. (2018). Altered Gut Microbiota and Compositional Changes in Firmicutes and Proteobacteria in Mexican Undernourished and Obese Children. Front Microbiol *9*.

Miranda, K., Yang, X., Bam, M., Murphy, E.A., Nagarkatti, P.S., and Nagarkatti, M. (2018). MicroRNA-30 modulates metabolic inflammation by regulating Notch signaling in adipose tissue macrophages. Int J Obes (Lond) *42*, 1140–1150.

Miranda, K., Mehrpouya-Bahrami, P., Nagarkatti, P.S., and Nagarkatti, M. (2019). Cannabinoid Receptor 1 Blockade Attenuates Obesity and Adipose Tissue Type 1 Inflammation Through miR-30e-5p Regulation of Delta-Like-4 in Macrophages and Consequently Downregulation of Th1 Cells. Front. Immunol. *10*.

Moore, K.J., Sheedy, F.J., and Fisher, E.A. (2013). Macrophages in atherosclerosis: a dynamic balance. Nat Rev Immunol *13*, 709–721.

Muccioli, G.G., Naslain, D., Bäckhed, F., Reigstad, C.S., Lambert, D.M., Delzenne, N.M., and Cani, P.D. (2010). The endocannabinoid system links gut microbiota to adipogenesis. Mol. Syst. Biol. *6*, 392.

Mukherjee, S., and Hooper, L.V. (2015). Antimicrobial Defense of the Intestine. Immunity *42*, 28–39.

Nakano, T., Fukuda, D., Koga, J., and Aikawa, M. (2016). Delta-Like Ligand 4-Notch Signaling in Macrophage Activation. Arteriosclerosis, Thrombosis, and Vascular Biology *36*, 2038–2047.

Nelson, D.L., Lehninger, A.L., and Cox, M.M. (2008). Lehninger Principles of Biochemistry (Macmillan).

Neurath, M.F., Weigmann, B., Finotto, S., Glickman, J., Nieuwenhuis, E., Iijima, H., Mizoguchi, A., Mizoguchi, E., Mudter, J., Galle, P.R., et al. (2002). The transcription factor T-bet regulates mucosal T cell activation in experimental colitis and Crohn's disease. J. Exp. Med. *195*, 1129–1143.

O'Connell, R.M., Taganov, K.D., Boldin, M.P., Cheng, G., and Baltimore, D. (2007). MicroRNA-155 is induced during the macrophage inflammatory response. Proc Natl Acad Sci U S A *104*, 1604–1609.

Olefsky, J.M., and Glass, C.K. (2010). Macrophages, Inflammation, and Insulin Resistance. Annual Review of Physiology *72*, 219–246.

Pajvani, U.B., Shawber, C.J., Samuel, V.T., Birkenfeld, A.L., Shulman, G.I., Kitajewski, J., and Accili, D. (2011). Inhibition of Notch signaling ameliorates insulin resistance in a FoxO1-dependent manner. Nat Med *17*, 961–967.

Petersen, C., and Round, J.L. (2014). Defining dysbiosis and its influence on host immunity and disease. Cell Microbiol *16*, 1024–1033.

Pi-Sunyer, F.X., Aronne, L.J., Heshmati, H.M., Devin, J., Rosenstock, J., and RIO-North America Study Group (2006). Effect of rimonabant, a cannabinoid-1 receptor blocker, on weight and cardiometabolic risk factors in overweight or obese patients: RIO-North America: a randomized controlled trial. JAMA *295*, 761–775.

Plovier, H., Everard, A., Druart, C., Depommier, C., Hul, M.V., Geurts, L., Chilloux, J., Ottman, N., Duparc, T., Lichtenstein, L., et al. (2017). A purified membrane protein from *Akkermansia muciniphila* or the pasteurized bacterium improves metabolism in obese and diabetic mice. Nature Medicine *23*, 107–113.

Putluri, N., Shojaie, A., Vasu, V.T., Nalluri, S., Vareed, S.K., Putluri, V., Vivekanandan-Giri, A., Byun, J., Pennathur, S., Sana, T.R., et al. (2011a). Metabolomic profiling reveals a role for androgen in activating amino acid

metabolism and methylation in prostate cancer cells. PLoS ONE *6*, e21417.

Putluri, N., Shojaie, A., Vasu, V.T., Vareed, S.K., Nalluri, S., Putluri, V., Thangjam, G.S., Panzitt, K., Tallman, C.T., Butler, C., et al. (2011b). Metabolomic profiling reveals potential markers and bioprocesses altered in bladder cancer progression. Cancer Res. *71*, 7376–7386.

Qin, Y., Roberts, J.D., Grimm, S.A., Lih, F.B., Deterding, L.J., Li, R., Chrysovergis, K., and Wade, P.A. (2018). An obesity-associated gut microbiome reprograms the intestinal epigenome and leads to altered colonic gene expression. Genome Biol *19*.

Qiu, Y., Nguyen, K.D., Odegaard, J.I., Cui, X., Tian, X., Locksley, R.M., Palmiter, R.D., and Chawla, A. (2014). Eosinophils and type 2 cytokine signaling in macrophages orchestrate development of functional beige fat. Cell *157*, 1292–1308.

Rao, R.R., Long, J.Z., White, J.P., Svensson, K.J., Lou, J., Lokurkar, I., Jedrychowski, M.P., Ruas, J.L., Wrann, C.D., Lo, J.C., et al. (2014). Meteorin-like is a hormone that regulates immune-adipose interactions to increase beige fat thermogenesis. Cell *157*, 1279–1291.

Ravinet Trillou, C., Arnone, M., Delgorge, C., Gonalons, N., Keane, P., Maffrand, J.-P., and Soubrie, P. (2003). Anti-obesity effect of SR141716, a CB1

receptor antagonist, in diet-induced obese mice. Am. J. Physiol. Regul. Integr. Comp. Physiol. *284*, R345-353.

Ravinet Trillou, C., Delgorge, C., Menet, C., Arnone, M., and Soubrié, P. (2004). CB1 cannabinoid receptor knockout in mice leads to leanness, resistance to diet-induced obesity and enhanced leptin sensitivity. Int. J. Obes. Relat. Metab. Disord. *28*, 640–648.

Red Eagle, A., and Chawla, A. (2010). In obesity and weight loss, all roads lead to the mighty macrophage. Journal of Clinical Investigation *120*, 3437–3440.

Redinger, R.N. (2007). The Pathophysiology of Obesity and Its Clinical Manifestations. Gastroenterol Hepatol (N Y) *3*, 856–863.

Reid, G., Kao, S.C., Pavlakis, N., Brahmbhatt, H., MacDiarmid, J., Clarke, S., Boyer, M., and van Zandwijk, N. (2016). Clinical development of TargomiRs, a miRNA mimic-based treatment for patients with recurrent thoracic cancer. Epigenomics *8*, 1079–1085.

Robertson, S.J., Lemire, P., Maughan, H., Goethel, A., Turpin, W., Bedrani, L., Guttman, D.S., Croitoru, K., Girardin, S.E., and Philpott, D.J. (2019). Comparison of Co-housing and Littermate Methods for Microbiota Standardization in Mouse Models. Cell Reports *27*, 1910-1919.e2.

Sam, A.H., Salem, V., and Ghatei, M.A. (2011). Rimonabant: From RIO to Ban. J Obes *2011*, 432607.

Schmitz, K., Mangels, N., Häussler, A., Ferreirós, N., Fleming, I., and Tegeder, I. (2016). Pro-inflammatory obesity in aged cannabinoid-2 receptor-deficient mice. Int J Obes (Lond) *40*, 366–379.

Segata, N., Izard, J., Waldron, L., Gevers, D., Miropolsky, L., Garrett, W.S., and Huttenhower, C. (2011). Metagenomic biomarker discovery and explanation. Genome Biol. *12*, R60.

Shan, T.-D., Ouyang, H., Yu, T., Li, J.-Y., Huang, C.-Z., Yang, H.-S., Zhong, W., Xia, Z.-S., and Chen, Q.-K. (2016). miRNA-30e regulates abnormal differentiation of small intestinal epithelial cells in diabetic mice by downregulating Dll4 expression. Cell Prolif. *49*, 102–114.

Singh, U.P., Singh, N.P., Singh, B., Price, R.L., Nagarkatti, M., and Nagarkatti, P.S. (2012). Cannabinoids Receptor-2 (CB2) agonist ameliorates colitis in IL-10−/− mice by attenuating the activation of T cells and promoting their apoptosis. Toxicol Appl Pharmacol *258*, 256–267.

Singh, U.P., Murphy, A.E., Enos, R.T., Shamran, H.A., Singh, N.P., Guan, H., Hegde, V.L., Fan, D., Price, R.L., Taub, D.D., et al. (2014). miR-155 deficiency protects mice from experimental colitis by reducing T helper type 1/type 17 responses. Immunology *143*, 478–489.

Sipe, J.C., Waalen, J., Gerber, A., and Beutler, E. (2005). Overweight and obesity associated with a missense polymorphism in fatty acid amide hydrolase (FAAH). Int J Obes (Lond) *29*, 755–759.

Soh, J., Iqbal, J., Queiroz, J., Fernandez-Hernando, C., and Hussain, M.M. (2013). MicroRNA-30c reduces hyperlipidemia and atherosclerosis in mice by decreasing lipid synthesis and lipoprotein secretion. Nat Med *19*, 892–900.

Sonnenburg, J.L., and Bäckhed, F. (2016). Diet-microbiota interactions as moderators of human metabolism. Nature *535*, 56–64.

van Stijn, C.M.W., Kim, J., Lusis, A.J., Barish, G.D., and Tangirala, R.K. (2015). Macrophage polarization phenotype regulates adiponectin receptor expression and adiponectin anti-inflammatory response. FASEB J. *29*, 636–649.

Sturn, A., Quackenbush, J., and Trajanoski, Z. (2002). Genesis: cluster analysis of microarray data. Bioinformatics *18*, 207–208.

Suárez-Zamorano, N., Fabbiano, S., Chevalier, C., Stojanović, O., Colin, D.J., Stevanović, A., Veyrat-Durebex, C., Tarallo, V., Rigo, D., Germain, S., et al. (2015). Microbiota depletion promotes browning of white adipose tissue and reduces obesity. Nat Med *21*, 1497–1501.

Sun, S., Ji, Y., Kersten, S., and Qi, L. (2012). Mechanisms of Inflammatory Responses in Obese Adipose Tissue. Annu Rev Nutr *32*, 261–286.

Taganov, K.D., Boldin, M.P., Chang, K.-J., and Baltimore, D. (2006). NF-κB-dependent induction of microRNA miR-146, an inhibitor targeted to signaling proteins of innate immune responses. PNAS *103*, 12481–12486.

Tomar, S., E. Zumbrun, E., Nagarkatti, M., and Nagarkatti, P.S. (2015). Protective Role of Cannabinoid Receptor 2 Activation in Galactosamine/Lipopolysaccharide-Induced Acute Liver Failure through Regulation of Macrophage Polarization and MicroRNAs. Journal of Pharmacology and Experimental Therapeutics *353*, 369–379.

Toraño, E.G., García, M.G., Fernández-Morera, J.L., Niño-García, P., and Fernández, A.F. (2016). The Impact of External Factors on the Epigenome: In Utero and over Lifetime. Biomed Res Int *2016*.

Touriño, C., Oveisi, F., Lockney, J., Piomelli, D., and Maldonado, R. (2010). FAAH deficiency promotes energy storage and enhances the motivation for food. Int J Obes (Lond) *34*, 557–568.

Turcotte, C., Blanchet, M.-R., Laviolette, M., and Flamand, N. (2016). The CB2 receptor and its role as a regulator of inflammation. Cell Mol Life Sci *73*, 4449–4470.

Turnbaugh, P.J., Ley, R.E., Mahowald, M.A., Magrini, V., Mardis, E.R., and Gordon, J.I. (2006). An obesity-associated gut microbiome with increased capacity for energy harvest. Nature *444*, 1027–1031.

Vandanmagsar, B., Youm, Y.-H., Ravussin, A., Galgani, J.E., Stadler, K., Mynatt, R.L., Ravussin, E., Stephens, J.M., and Dixit, V.D. (2011). The NALP3/NLRP3 Inflammasome Instigates Obesity-Induced Autoinflammation and Insulin Resistance. Nat Med *17*, 179–188.

Vantaku, V., Donepudi, S.R., Ambati, C.R., Jin, F., Putluri, V., Nguyen, K., Rajapakshe, K., Coarfa, C., Battula, V.L., Lotan, Y., et al. (2017). Expression of ganglioside GD2, reprogram the lipid metabolism and EMT phenotype in bladder cancer. Oncotarget *8*, 95620–95631.

Vantaku, V., Dong, J., Ambati, C.R., Perera, D., Donepudi, S.R., Amara, C.S., Putluri, V., Ravi, S.S., Robertson, M.J., Piyarathna, D.W.B., et al. (2019). Multi-omics Integration Analysis Robustly Predicts High-Grade Patient Survival and Identifies CPT1B Effect on Fatty Acid Metabolism in Bladder Cancer. Clin. Cancer Res.

Verty, A.N.A., Stefanidis, A., McAinch, A.J., Hryciw, D.H., and Oldfield, B. (2015). Anti-Obesity Effect of the CB2 Receptor Agonist JWH-015 in Diet-Induced Obese Mice. PLoS ONE *10*, e0140592.

Weber, N., Liou, D., Dommer, J., MacMenamin, P., Quiñones, M., Misner, I., Oler, A.J., Wan, J., Kim, L., Coakley McCarthy, M., et al. (2018). Nephele: a cloud platform for simplified, standardized and reproducible microbiome data analysis. Bioinformatics *34*, 1411–1413.

Weisberg, S.P., McCann, D., Desai, M., Rosenbaum, M., Leibel, R.L., and Ferrante, A.W. (2003). Obesity is associated with macrophage accumulation in adipose tissue. J Clin Invest *112*, 1796–1808.

Winer, D.A., Luck, H., Tsai, S., and Winer, S. (2016). The Intestinal Immune System in Obesity and Insulin Resistance. Cell Metab. *23*, 413–426.

Xiao, C., and Rajewsky, K. (2009). MicroRNA Control in the Immune System: Basic Principles. Cell *136*, 26–36.

Xu, H., Barnes, G.T., Yang, Q., Tan, G., Yang, D., Chou, C.J., Sole, J., Nichols, A., Ross, J.S., Tartaglia, L.A., et al. (2003). Chronic inflammation in fat plays a crucial role in the development of obesity-related insulin resistance. J. Clin. Invest. *112*, 1821–1830.

Xu, H., Zhu, J., Smith, S., Foldi, J., Zhao, B., Chung, A.Y., Outtz, H., Kitajewski, J., Shi, C., Weber, S., et al. (2012). Notch-RBP-J signaling regulates the transcription factor IRF8 to promote inflammatory macrophage polarization. Nat. Immunol. *13*, 642–650.

Zhang, F.F., Cardarelli, R., Carroll, J., Zhang, S., Fulda, K.G., Gonzalez, K., Vishwanatha, J.K., Morabia, A., and Santella, R.M. (2011). Physical activity and global genomic DNA methylation in a cancer-free population. Epigenetics *6*, 293–299.

Zhang, K., Song, F., Lu, X., Chen, W., Huang, C., Li, L., Liang, D., Cao, S., and Dai, H. (2017). MicroRNA-322 inhibits inflammatory cytokine expression and promotes cell proliferation in LPS-stimulated murine macrophages by targeting NF-κB1 (p50). Bioscience Reports *37*, BSR20160239.

Zhang, P., Yu, Y., Qin, Y., Zhou, Y., Tang, R., Wang, Q., Li, X., Wang, H., Weston-Green, K., Huang, X.-F., et al. (2019). Alterations to the

microbiota-colon-brain axis in high-fat-diet-induced obese mice compared to diet-resistant mice. J. Nutr. Biochem. *65*, 54–65.

Zhang, Y., Zhang, M., Zhong, M., Suo, Q., and Lv, K. (2013). Expression profiles of miRNAs in polarized macrophages. Int. J. Mol. Med. *31*, 797–802.

Zhao, L. (2013). The gut microbiota and obesity: from correlation to causality. Nat. Rev. Microbiol. *11*, 639–647.

APPENDIX A

DETAILED EXPERIMENTAL PROTOCOLS

PROTOCOL 1: IMMUNOHISTOCHEMISTRY: WHOLE-MOUNT ADIPOSE TISSUE

Materials:

4% (w/v) Paraformaldehyde in PBS

1% Triton X-100 (Molecular Probes, ThermoFisher, HFH10)

1% (w/v) BSA in PBS

Antibodies

BODIPY 558/568 C12 (Molecular Probes, ThermoFisher, D3835)

Hoechst 33342 (Molecular Probes, ThermoFisher, H21492)

Microscope slides

Coverslips

10 mL syringe

16-gauge needle

Fluoromount-G (eBioscience, 00-4958-02)

Rapid Dry Nail Polish

Sterile PBS

Vaseline

Antibodies:

Mouse FcR Blocker

Alexa Fluor 488 anti-mouse F4/80 Antibody (Biolegend, 123120; BM-8)

Alexa Fluor 633 Protein Labeling Kit (ThermoFisher, A20170)

Purified anti-mouse Notch 1 Antibody (Biolegend, 130602; HMN1-12)

Purified anti-mouse DLL4 Antibody (Biolegend, 130802; HMD4-1)

Procedure:

1. Dissect epididymal fat pads from euthanized mice and mince into small pieces (~2-3 mm) using a scalpel.
2. Wash tissue pieces in PBS.
3. Fix in 4% paraformaldehyde for 3h at RT.
4. Permeabilize with 1% Triton X-100 for 10m at RT.
5. Block with 1% BSA + 1ug mouse FcR blocker for 40m at RT.
6. Incubate in primary Ab overnight at 4°C (anti-F4/80, anti-NOTCH1, anti-DLL4; [5ug/ml=1:100 dilution] in 1% BSA/PBS).
7. Incubate in secondary Ab for 1h at RT (Rabbit anti-Hamster IgG—Alexa Fluor 633 [10ug/ml=1:100 dilution] in 1% BSA/PBS).
8. Counterstain with BODIPY 558/568 [5uM] and Hoechst 33342 [40uM] for 1hr at RT.
9. Wash 3X with PBS and place on center of microscope slide.
10. Make a boundary of Vaseline around the samples about 2mm high (matching tissue height) using a Vaseline-filled syringe.
11. Fill inside of boundary with Fluoromount-G.
12. Gently place coverslip onto the slide on top of the Vaseline boundary
13. Lightly push down to meet the top of the sample.
14. Seal edges with nail polish and let dry.
15. Store 2-8°C in dark.
16. Image within 3 days by confocal microscopy.

PROTOCOL 2: BONE MARROW-DERIVED MACROPHAGE (BMDM) DIFFERENTIATION

Materials:

Sterile PBS

Complete DMEM or DMEM/F12 (supplemented with 10% (v/v) heat-inactivated FBS, 1% (v/v) penicillin/streptomycin mixture, 2mM L-glutamine)

Recombinant mouse M-CSF, carrier-free (BioLegend 576406)

5-10mL syringe fitted with a 20-gauge needle

Procedure:

1. Dissect the tibias and femurs from euthanized 6-8-week-old naïve female C57BL6 mice.
2. Flush the bones using an ice-cold PBS-filled syringe fitted with a 20-gauge needle. Use approximately 5-10 mL PBS per bone.
3. Manually dissociate bone marrow by vortexing or passing through a syringe.
4. Filter suspension through a sterile 70uM nylon mesh.
5. Pellet cells (300xg, 7m, 4°C) and pour off supernatant.
6. Resuspend cell pellet in 1mL RBC-lysis buffer and incubate 3-5m at RT.
7. Add 10mL complete medium and pellet cells (300xg, 7m, 4°C).
8. Resuspend in complete medium and count cells.
9. Plate $2x10^6$ cells in 10mL complete medium + 1U/mL M-CSF in a T-75 flask or 100mm cell-culture dish.
10. Incubate (37°C, 5% CO_2, 95% humidity) for 7-10 days with the addition of 5mL complete medium + 1U/mL M-CSF on Day 4.

PROTOCOL 3: MACROPHAGE: LYMPHOCYTE CO-CULTURE

Materials:

6- and 24-well tissue culture plates

Complete RPMI 1640 medium (cRPMI) supplemented with 10% heat-inactivated FBS, 1% penicillin/streptomycin, 2mM L-glutamine, 10mM HEPES buffer, and 0.0002% β-mercaptoethanol

Sterile PBS

DMSO and 100mM AM251 (Tocris 1117)

Isotype control IgG and anti-DLL4 blocking mAb (BioLegend 130804)

Lipopolysaccharide (LPS) (eBioscience 00-4976)

Recombinant mouse cytokines, carrier-free (IFNγ: BioLegend 575302, IL-4: BioLegend 574302)

ConcanavalinA (ConA) (Sigma C5275)

Day 0:

1. Plate $1.5x10^6$ mature BMDM in 1.5mL cRPMI medium in 6-well plates.
2. Add 0.5mL cRPMI containing DMSO (vehicle control), 10uM AM251, IgG (Isotype control) or 1ug/mL anti-DLL4 mAb.
3. Incubate 1h (37°C, 5% CO_2, 95% humidity).

4. Polarize BMDM by addition of 200uL cRPMI containing polarization factors (M1: 1ug/mL LPS + 500ng/mL IFNγ, M2: 10ng/mL IL-4).
5. Culture for 24h (37°C, 5% CO_2, 95% humidity).

Day 1:

1. Isolate cervical, axillary, popliteal, mesenteric, and inguinal lymph nodes from euthanized naïve 6-8-week-old female C57BL6 mice.
2. Bring lymphocytes to single-cell suspension by filtering through a sterile 70um nylon mesh and washing in cRPMI. Count cells. Keep on ice.
3. Detach pre-treated and polarized BMDM from 6-well plates by gently scraping. Pellet BMDM by centrifugation (300xg, 7m, 4°C). Store supernatant at -20°C and wash BMDM 3X with PBS.
4. Resuspend BMDM in cRPMI. Count. Adjust to $2x10^5$ BMDM/mL.
5. Plate $3x10^5$ lymphocytes in 0.5mL cRPMI containing 2ug/mL ConA into a 24-well plate in the wells that will contain a 1:1 co-culture ratio. Plate $1x10^5$ lymphocytes in 0.5mL cRPMI containing 2ug/mL ConA into the wells that will contain a 1:3 co-culture ratio. Plate 1 extra well for ConA stimulation control. Plate 1 well of lymphocytes in cRPMI without ConA as an unstimulated control.
6. Add 500uL of each BMDM suspension to the appropriate lymphocyte wells. For the positive and negative ConA stimulation control wells add 500uL cRPMI. The final ConA concentration is 1ug/mL for all wells.
7. Culture for 48h (37°C, 5% CO_2, 95% humidity).
8. Harvest cells on Day 3 for flow cytometry and supernatants for ELISAs.

APPENDIX B

PERMISSION TO REPRINT

PERMISSION TO REPRINT CHAPTER 2

RightsLink®

Home | Account Info | Help

SPRINGER NATURE

Title: MicroRNA-30 modulates metabolic inflammation by regulating Notch signaling in adipose tissue macrophages

Author: Kathryn Miranda et al

Publication: International Journal of Obesity

Publisher: Springer Nature

Date: Jun 13, 2018

Logged in as:
Kathryn Miranda
LOGOUT

Author Request

If you are the author of this content (or his/her designated agent) please read the following. If you are not the author of this content, please click the Back button and select no to the question "Are you the Author of this Springer Nature content?".
Ownership of copyright in original research articles remains with the Author, and provided that, when reproducing the contribution or extracts from it or from the Supplementary Information, the Author acknowledges first and reference publication in the Journal, the Author retains the following non-exclusive rights:
To reproduce the contribution in whole or in part in any printed volume (book or thesis) of which they are the author(s).
The author and any academic institution, where they work, at the time may reproduce the contribution for the purpose of course teaching.
To reuse figures or tables created by the Author and contained in the Contribution in oral presentations and other works created by them.
To post a copy of the contribution as accepted for publication after peer review (in locked Word processing file, of a PDF version thereof) on the Author's own web site, or the Author's institutional repository, or the Author's funding body's archive, six months after publication of the printed or online edition of the Journal, provided that they also link to the contribution on the publisher's website.
Authors wishing to use the published version of their article for promotional use or on a web site must request in the normal way.

If you require further assistance please read Springer Nature's online author reuse guidelines.

For full paper portion: Authors of original research papers published by Springer Nature are encouraged to submit the author's version of the accepted, peer-reviewed manuscript to their relevant funding body's archive, for release six months after publication. In addition, authors are encouraged to archive their version of the manuscript in their institution's repositories (as well as their personal Web sites), also six months after original publication.

v1.0

BACK | CLOSE WINDOW

Permission to Reprint Chapter 3

Citation: Miranda K, Mehrpouya-Bahrami P, Nagarkatti PS and Nagarkatti M (2019) Cannabinoid Receptor 1 Blockade Attenuates Obesity and Adipose Tissue Type 1 Inflammation Through miR-30e-5p Regulation of Delta-Like-4 in Macrophages and Consequently Downregulation of Th1 Cells. *Front. Immunol.* 10:1049. doi: 10.3389/fimmu.2019.01049